Gain-switched all-fiber lasers and quasi-continuous wave supercontinuum generation

Larsen, Casper

Publication date:
2013

Document Version
Publisher's PDF, also known as Version of record

DTU Fotonik
Department of Photonics Engineering

Technical University of Denmark

Gain-switched all-fiber lasers and quasi-continuous wave supercontinuum generation

Casper Larsen
PhD Thesis
December 2013

NKT Photonics

Abstract

The extreme broadening phenomenon of supercontinuum (SC) generation in optical fibers is the basis of SC laser sources. These sources have numerous applications in areas, such as spectroscopy and microscopy due to the unique combination of extremely broad spectral bandwidths, high spectral power densities, and high spatial coherence.

In this work the feasibility of applying gain-switched all-fiber lasers to SC generation is investigated. It is motivated by the simplicity of the architecture and the ability to scale the optical output power of such fiber lasers.

The physics of fiber lasers are reviewed to understand the mechanisms involved in gain-switching. A detailed numerical model is provided to give deep insight into the different stages of pulse generation. A simplified model is also developed to derive an analytic expression for the pulse duration.

Extensive experiments with gain-switching of fiber lasers with a variety of different configurations are carried out. The peak power, pulse duration, bandwidth, and scaling with repetition rate are thoroughly described. General guidelines are submitted to enable designing of gain-switched fiber lasers with specifically tailored properties.

The physics of SC generation are reviewed with focus on the quasi-continuous wave pumping regime. Experiments with a gain-switched fiber laser as a pump for SC generation in photonic crystal fibers are carried out. Requirements for efficient SC generation are analyzed. Finally, an optimization of photonic crystal fibers for gain-switched fiber laser-pumped SC generation is presented.

Resumé (in Danish)

Den danske titel på projektet er noget i stil med: *Forstærkningsmodulerede fiberlasere og kvasi-kontinuerligt superkontinuum generering.*

Det ekstreme udvidelsesfænomen superkontinuum generation i optiske fibre er grundlaget for superkontinuum laser kilder. Disse kilder har en lang række anvendelser inden for områder som spektroskopi og mikroskopi på grund af den unikke kombination af den ekstremt brede spektrale båndbredde, høj spektral effekttæthed og høj rumlig kohærens.

I dette projekt undersøges muligheden for at benytte forstærkningsmodulerede fiberlasere til superkontinuum generation. Dette projekt er motiveret af enkeltheden og muligheden for at skalere den optiske effekt af sådanne fiberlasere.

Fysikken bag fiberlasere gennemgås for at forstå de mekanismer, der er involveret i forstærkningsmodulering. En detaljeret numerisk model er beskrevet for at give dyb indsigt i de forskellige faser af pulsgeneringen. En forenklet model er også udviklet til at gøre det muligt at finde et analytisk udtryk for pulsvarighed.

Omfattende eksperimenter med forstærkningsmodulering af fiberlasere med en række forskellige konfigurationer er udført. Spids-effekt, pulsvarighed, den spektrale båndbredde, og skalering med repetitionsraten er grundigt beskrevet. Generelle retningslinjer er fremsat som muliggør at designe en forstærkningsmoduleret fiberlaser med specifikke egenskaber.

Fysikken bag superkontinuum generation gennemgås med fokus på det kvasi-kontinuere pumpingsregime. Eksperimenter med en forstærkningsmoduleret fiberlaser som pumpe til superkontinuum generation i fotoniske krystal fibre er udført. Betingelser for effektiv superkontinuum generation er analyseret. Endelig er en optimering af fotoniske krystal fibre til forstærkningsmoduleret fiberlaser pumpet superkontinuum

generation fremlagt.

Preface

This thesis is submitted for the degree of Doctor of Philosophy to the Technical University of Denmark.

This PhD-project has been prepared from the August, 2010 to December, 2013 by the author. It has been carried out as a part of the research project "Intelligent Tapers and Seeding for taming the optical Rogue wave and develop stable deep-blue Supercontinuum light sources" (ITRUS) supported by the Danish Research Council for Technology and Production Sciences, (Ref. 09-070566). The project partners were DTU Fotonik – the Department of Photonics Engineering at the Technical University of Denmark and NKT Photonics A/S in Birkerød. The supervisors were Professor Dr. Ole Bang, DTU Fotonik, Senior Researcher Dr. Kent Mattsson, DTU Fotonik, Senior Scientist Dr. Peter M. W. Skovgaard, and Head of Marketing Dr. Kim P. Hansen, NKT Photonics. NKT Photonics delivered experimental expertise and equipment, and a large part of the project is therefore carried out in Birkerød.

The PhD-project also included a three month external stay at Fraunhofer Institute for Laser Technology in Aachen, Germany. The goal of the project was to investigate the feasibility of second harmonic generation of a gain-switched fiber laser. Results of the gain-switching are included here, whereas the second harmonic generation results are left out to maintain the focus of the thesis.

A part of the project was conducted in very close collaboration with NKT Photonics, where picosecond-pumped supercontinua were analyzed and modeled to improve the understanding of the spectral shape. In continuation of this work, the author was hired by NKT Photonics for a four month period in 2013 to investigate and improve properties of supercontinua. This effort resulted in contributions to a submitted patent. Due to intellectual property rights, this work could not be published and

is *omitted* from the thesis.

A detailed numerical model is developed in the project and implemented in Matlab. This code is made publicly available on www.muder.dk/GS.

Citations are indicated by number and the full list of citations is placed in the last section of the thesis. All figures are made by the author unless otherwise stated. Furthermore, a list of abbreviations is located after the conclusion. A few appendices are attached and are referenced within the relevant sections.

Acknowledgements

First of all I would like to thank all of my supervisors for their support, suggestions, guidance, and for making this project possible. I would like to thank Ole Bang for giving me the opportunity and for sharing his great enthusiasm. The assignment from a supervisor from NKT Photonics has been a bit of a joy ride – nevertheless getting support has never been a problem. At first, Kent E. Mattsson was assigned, however, before I even started he moved to DTU Fotonik (and continued being my supervisor). The next supervisor I had an opportunity to 'scare' away was Peter M. W. Skovgaard, who after four very productive months left the company (for other reasons of course). The final victim was Kim P. Hansen, who soon after abandoning the engineering department and became the head of marketing. Bad luck or faith? When it comes down to it, I could never imagine a more competent team of supervisors.

I owe credit to Jes Broeng, Christian Jakobsen, and Thomas Tanggaard Alkeskjold for creating some fantastic optical fibers and their never ending support. A very special thanks goes to Danny Noordegraaf for brilliant experimental guidance and continuous support. A great thanks goes to Chris Brooks for proofreading the manuscript. Also a thanks to all the people at NKT Photonics who I have been working with over the last three years, and to all the always helpful and cheerful people in the lab.

Thanks to the people involved in my external stay in Aachen, Germany, in 2012. A special thanks to Bernd Jungbluth for making it possible, Martin Giesberts for great collaboration in the lab, and Sebastian Nyga and Oliver Fitzau for exciting discussions.

Thanks to my fellow PhD students and colleagues Simon Sørensen, Christian Agger, Mette Marie Johansen, Sidsel Petersen, Marco Laurila, Kristian Hansen, Irnis Kubat, Uffe Møller, and many others for great company.

Finally, I would also like to thank Camilla, my family, and all my friends for their help and support during this PhD study.

Contents

List of publications

Most of the work described in this thesis has been published in peer-review journal publications and in conference contributions. A patent has also been filed based on experiments carried out at NKT Photonics during my leave from the PhD project in 2013. Additionally, a paper based on my unrelated master's project has been prepared during the early stage of the PhD project.

Peer-reviewed journal publications

Paper I C. Larsen, D. Noordegraaf, P. M. W. Skovgaard, K. P. Hansen, K. E. Mattsson, and O. Bang, "Gain-switched CW fiber laser for improved supercontinuum generation in a PCF." Optics Express **19**, 14883–91 (2011).

Paper II C. Larsen, S. Sørensen, D. Noordegraaf, K. Hansen, K. Mattsson, and O. Bang, "Zero-dispersion wavelength independent quasi-CW pumped supercontinuum generation," Optics Communications **290**, 170–174 (2013).

Paper III C. Larsen, M. Giesberts, S. Nyga, O. Fitzau, B. Jungbluth, H. D. Hoffmann, and O. Bang, "Gain-switched all-fiber laser with narrow bandwidth," Optics Express **21**, 170–174 (2013).

Paper IV C. Larsen, K. P. Hansen, K. E. Mattsson, and O. Bang, "The all-fiber cladding-pumped gain-switched fiber laser," Optics Express **22**, 1490–1499 (2014).

Conference contributions

Paper V C. Larsen, P. M. W. Skovgaard, D. Noordegraaf, K. P. Hansen, K. E. Mattsson, and O. Bang, "Supercontinuum generation in a photonic crystal fiber pumped by a gain-switched high-power fiber laser," CLEO EU (2010).

Paper VI C. Larsen, D. Noordegraaf, K. P. Hansen, K. E. Mattsson, and O. Bang, "Photonic crystal fibers for supercontinuum generation pumped by a gain-switched CW fiber laser," SPIE (2012).

Paper VII C. Larsen, M. Giesberts, S. Nyga, O. Fitzau, B. Jungbluth, H. D. Hoffmann, and O. Bang, "Gain-switched, Yb-doped, all-fiber laser with narrow bandwidth," CLEO EU (2013).

Peer-reviewed journal publications out of the scope of the thesis

Paper Z C. Larsen, D. G. Cooke, and P. U. Jepsen, "Finite-difference time-domain analysis of time-resolved terahertz spectroscopy experiments," Journal of the Optical Society of America B **28**, 1308–1316 (2011).

Coauthor in peer-reviewed journal publications

Paper IX S. T. Sørensen, C. Larsen, U. Møller, P. M. Moselund, C. L. Thomsen, and O. Bang, "Influence of pump power and modulation instability gain spectrum on seeded supercontinuum and rogue wave generation," Journal of the Optical Society of America B **29**, 2875–2885 (2012).

Paper X U. Møller, S. T. Sørensen, C. Larsen, P. M. Moselund, C. Jakobsen, J. Johansen, C. L. Thomsen, and O. Bang, "Optimum PCF tapers for blue-enhanced supercontinuum sources," Optical Fiber Technology **18**, 304–314 (2012).

Paper XI S. T. Sørensen, U. Møller, C. Larsen, P. M. Moselund, C. Jakobsen, J. Johansen, T. V. Andersen, C. L. Thomsen, and O. Bang, "Deep-blue supercontinnum sources with optimum taper profiles–verification of GAM." Optics Express **20**, 10635–45 (2012).

Paper XII S. T. Sørensen, C. Larsen, U. Møller, P. M. Moselund, C. L. Thomsen, and O. Bang, "The role of phase coherence in seeded supercontinuum generation." Optics Express **20**, 22886–94 (2012).

Paper XIII S. T. Sørensen, C. Larsen, C. Jakobsen, C. L. Thomsen, and O. Bang, "Single-mode high air-fill fraction photonic crystal fiber for high-power deep-blue supercontinuum sources." Optics Express (Accepted January 2014).

Author contributions

In all first-authored papers (I-IV) the author provided the dominant contribution in the design of the experiments and in conducting the experiments. The author carried out the analysis of the data and prepared the manuscripts. All authors participated in the interpretation of the results, the writing of the paper, and the final approval of the version to be published.

In the coauthored papers (IX-XII) the author participated in the discussions of the results and the final approval of the version to be

published. In the papers (X-XI) the author also performed numerical modeling of the transverse properties of photonic crystal fibers.

Chapter 1

Introduction

The invention of the laser in the 1960s represents a gigantic scientific and technological step, and the Nobel Prize in Physics in 1964 was awarded to the theoretical pioneers [1, 2]. The very key feature of lasers is the high spatial and temporal coherence of the generated light, whereby unprecedented electric field strengths are achievable. The light-matter interaction at these high electric field strengths spawned the field of nonlinear optics, where the central outcome is the ability to generate light with frequencies other than the laser frequency [3, 4].

The quest for the capability to transmit laser light over long distances led in the 1970s to significant progress in reducing the loss in silica materials, which enabled fabrication of optical waveguides in fibers with extremely low loss [5, 6]. Rare-earth doping of fibers was developed alongside as efficient gain medium for amplification to compensate for the loss [7, 8]. The success of the optical fiber is not to be overlooked; more than 10^{12} m of fiber has been installed around the globe [9]. Later, rare-earth doped fiber lasers and amplifiers have emerged as technologies with a wide spectrum of applications entering new fields such as material processing and sensing. Owing to mass-produced high-power pump diodes and the double-clad pumping geometry, highly efficient fiber lasers with multiple kilowatts of output power are now commercially available [10, 11].

A side-effect of the fact that light can be confined in a small fiber core over very long distances, is that the optical powers required for nonlinear effects to occur is much lower than with bulk optics [12]. For telecommunication these effects are under most circumstances unwanted, but they can also be used to manipulate the light in peculiar ways [12–14]. The nonlinear effects in fibers are mainly governed by the degree of confinement and chromatic dispersion. The ultimate control of these

properties was made possible with the invention of the photonic crystal fiber (PCF) in the late 1990s [15]. The culmination of the PCF technology was the discovery of the spectacular nonlinear process of visible supercontinuum (SC) generation in 2000 [16]. A SC with wavelengths from 450 nm to 1600 nm could be generated in the fundamental transverse mode of the PCF by using an unprecedented low peak power in the kilowatt range [16].

A laser source based on SC generation solves a shortcoming of lasers, namely that wavelengths are restricted by the elements suitable for lasing (and their harmonics). Furthermore, SC laser sources can be made completely fiber-integrated, and therefore it is robust and maintenance-free. It can replace conventional lamps e.g. in microscopy [17, 18], but the high spatial coherence and the high spectral power density over the visible and near infrared wavelengths open up a huge potential for applications. Such applications are within fluorescence microscopy [19], stimulated emission depletion microscopy [20], optical coherence tomography [21–25], photo-acoustic imaging [25, 26], range finding [27, 28], broadband dispersion measurements [29, 30], and coherent anti-Stokes Raman scattering [31, 32].

1.1 Improving supercontinuum laser sources

SC laser sources are now commercially available using picosecond and nanosecond pumping by numerous vendors [17, 33–37]. There has been a continuous focus on improving the properties and reliability of such sources.

Particularly, the interest in expanding the wavelength range have resulted in demonstrations of an SC spanning almost three decades from 350–2600 nm [38–40]. Expanding the spectra beyond ∼2500 nm in silica fibers is challenging due to absorption losses, and new materials with broader transmission windows are being tested to make SC generation of light at near and far infrared wavelengths possible [41–44].

It is also of interest to increase the spectral power density in selected regions of the SC. Power scaling of picosecond pumped SC sources based on a PCF have reached ∼40 W of average power [45]. The scaling is limited by damages induced in the fiber core at the high intensities [46]. Infrared SC generation in large core fibers has been scaled to the 200 W level [47]. A high spectral power density can also be achieved by pumping PCFs with continuous wave (CW) fiber lasers [48–50]. The drawback of CW pumping is the low peak power, which leads to high sensitivity of the fiber parameters, reduced spectral broadening, and low

efficiency of visible light generation.

At the present state SC laser sources are technically applicable in many instruments and optical measuring methods, but the current price point for SC sources limits the implementation of such systems into relevant fields. Interest is therefore also on reducing the complexity of the SC source to reduce the cost and thereby enable applications within new areas.

1.2 Motivation for project

This project was spawned from the idea to use a fiber laser, which is gain-switched, as pump for an SC laser source. The envisioned SC laser setup is illustrated in Fig. 1.1. The benefits of this approach are that a high average power can be obtained and the simple construction reduces the cost of the source. This project is therefore a feasibility study to illuminate the possibilities and limitation of this design.

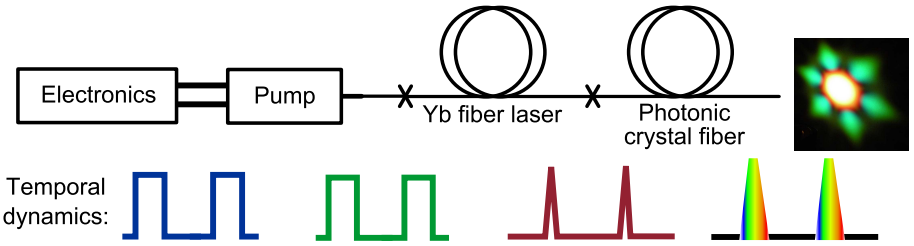

Figure 1.1: Envisioned SC laser source based on gain-switching of a fiber laser. The pulsed pump forces the fiber laser to emit high peak power pulses, which are suitable for SC generation.

The underlying physical principle of gain-switching (GS) is to control the inherent relaxation oscillations of the fiber laser occurring within a few μs after switching on the pump and therefore the gain of the laser [51]. By isolating the first and most powerful spike, a stable pulse train of high peak power pulses with tens-to-hundreds of nanoseconds in duration are created. The use of GS for improving the SC generation is motivated by the fact that the peak power of the pulses is nearly an order of a magnitude higher than the CW power. Even though the physical principles have been known for more than 50 years, little work on the subject is published compared to other pulsing techniques. One reason for this is that the pump power required in applying GS is more than an order of magnitude higher than what is required for Q-switching [52]. However, GS is increasingly interesting due to the decreasing cost

of pump diodes and the all-fiber construction. In this project gain-switched fiber lasers are investigated theoretically and experimentally to examine the opportunities and limitations of obtainable peak power, pulse duration, and spectral bandwidth.

SC generation dynamics occur on a time scale much shorter than that of pulses generated by GS, which can be as long as hundreds of nanoseconds in duration; therefore SC generation from a GS source is considered quasi-continuous wave (quasi-CW). The peak power of the GS pulses is lower than in picosecond-pumped SC generation, which affects the complex interplay of the linear and nonlinear processes in SC generation. Therefore, the specific quasi-CW SC dynamics are discussed and various PCFs are examined to optimize the efficiency of the process and bandwidth of the SC spectrum.

1.3 Thesis outline

In Chapter 2 a frame of reference to understand the propagation of light in fibers is given. This includes a description of different types of waveguides, how amplification in rare-earth doped fibers is achieved, solving of transverse fiber modes, and an introduction to the nonlinear propagation equation.

The physics of GS of fiber lasers are presented in Chapter 3. A detailed and a simplified model are both presented. Deep insight into the pulse generation process are given and the results of the models are compared to experimental results.

In Chapter 4 the experimental results of various fiber laser configurations and power levels are shown and discussed. The results are summarized and design guidelines are given.

In Chapter 5 the complex process of SC generation is analyzed and special attention is given to dynamics relevant to quasi-CW SC generation. A series of PCFs is pumped by pulses from a GS fiber laser and the spectral properties are discussed. Optimized PCFs are suggested based on these results.

Finally, the thesis is concluded in Chapter 6 and relevant future work is discussed.

In Appendix A the used abbreviations are listed. In Appendix B the current fiber laser technology is presented and it is intended to be an introduction to the terminology for the reader not familiar with the subject. The final three appendices on pumping of fiber lasers, the implementation of the detailed model of a fiber laser, the laser cavity, and chromatic material dispersion are included as additional material.

Chapter 2

Light propagation in fibers

In this section the physics of optical fibers, fiber lasers, and the mathematical basis to describe light propagation in fibers are presented.

2.1 The fiber geometry and guidance

The most common guiding mechanism in optical fibers is total internal reflection. It relies on an elevated refractive index in the light-guiding core compared to the refractive index of the surrounding cladding. In fiber optics the refractive index difference is often denoted by the numerical aperture,

$$\mathrm{NA} = \sqrt{n_c^2 - n_{cl}^2}, \tag{2.1}$$

where n_c is the core refractive index and n_{cl} is the cladding refractive index. A standard step index telecommunication fiber has an 8 μm Ge-doped core with a refractive index 0.36% higher than the cladding refractive index of 1.45 at a wavelength $\lambda = 1\mu$m, which results in an NA of 0.12. The highest angle of acceptance of an optical ray incident on the core of a fiber is given by $\theta_a = 2\sin^{-1}(\mathrm{NA})$, so a higher NA generally equates to the ability of a fiber to collect more of the light incident on the fiber core.

A step index fiber can be modeled by the (scalar) wave equation derived in section 2.3. The solution turns out to be a Bessel function of the first kind in the core region and a decaying modified Hankel function in the cladding region. The propagation constant β is then related to the effective index defined as $n_{\mathrm{eff}}(\lambda) = \beta(\lambda)2\pi/\lambda$, and for total internal reflection it is necessary that $n_c > n_{\mathrm{eff}} > n_{cl}$. The solution can be

normalized by introducing the so-called V-parameter;

$$V = \frac{2\pi a}{\lambda}\mathrm{NA}, \tag{2.2}$$

which dictates the properties of the fiber based on the wave behavior (the wavelength), the geometry (the core radius a), and the confinement (the NA). If $V < 2.405$ the fiber is called a single-mode fiber, which means that only a single transverse mode with two polarization states exists. For $2.405 < V < 3.832$ the two first higher order modes are also present and in total 6 guided modes (including the polarization states) can be guided. In practice the V-parameter is only a guideline for the number of guided modes because, e.g. bending of the fiber introduces significant loss for the least confined higher-order modes.

Since the early development of the optical fiber a vast amount of different fiber geometries have been proposed and fabricated [6]. The three most important fiber geometries for this project is shown in Fig. 2.1. These geometries are step index fiber with a single or a double cladding, and photonic crystal fiber (PCF).

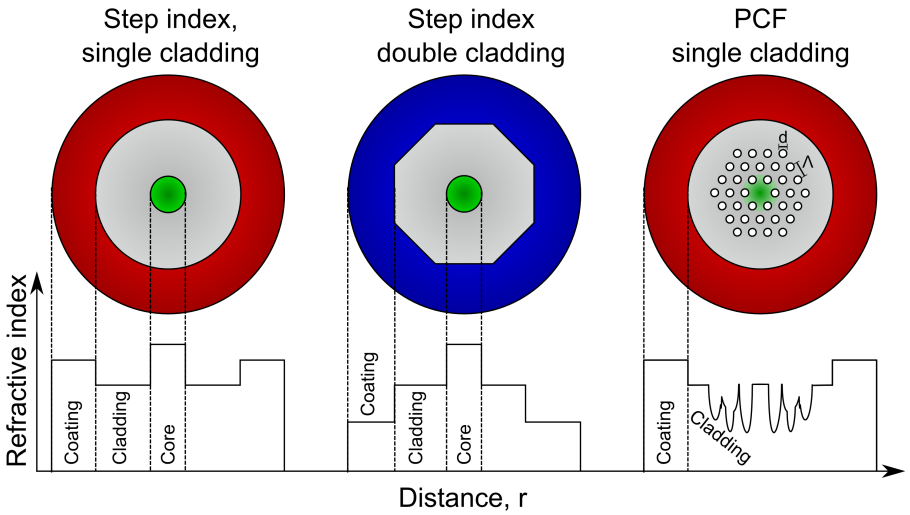

Figure 2.1: Facets of a single-clad step index fiber, a octagonal double clad step index fiber, and a PCF. In the lower section the refractive index profiles of the fibers are illustrated as function of the radial direction. The air hole diameter d and the hole-to-hole distance (pitch) Λ are shown. The radial and refractive index dimension are not shown to scale.

Optical fibers are typically constructed as a cylindrical core surrounded by a silica cladding with a diameter of 125 μm. The diameter

of the cladding is larger than what is necessary to confine the light and is chosen to obtain a good mechanical strength while still being easy to handle and process. The cladding is coated with a polymer to protect the fiber from the outside environment and scratches. The refractive index of the cladding is in most cases higher than silica to strip off (guide and absorb) the light that is lost in splices or along the fiber length due to, for example, scattering of defects.

Alternatively, the refractive index of the coating polymer can be lower than the refractive index of silica, which means that the silica cladding acts as a *highly* multi-mode waveguide. Such fibers with two waveguides are called doubled clad fibers, see Fig. 2.1. The refractive index of the polymer is lowered by fluorinating the polymer and the resulting cladding NA is typically on the order of 0.46, which corresponds to a full acceptance angle of 55°. Another approach is to use air as the second cladding material, which can be fabricated by isolating the first cladding by small silica bridges to an outer silica buffer [53]. This type of double cladding is called an air-clad and the NA can be up to 0.7 corresponding to a full acceptance angle of 89°. Double clad geometry fibers are mostly used for active rare-earth doped fibers, because the second cladding acts as a waveguide for the pump light, which can have a lower beam quality/larger divergence angle than what can be coupled to the core. The advantages of the double clad fibers are further described in section 2.2. In a cylindrically symmetric pump cladding circulating helical modes may exist, which will not pass through the fiber core to be absorbed. For this reason the pump cladding is often octagonal or D-shaped to break up cylindrical symmetry, as shown in Fig. 2.1.

2.1.1 The photonic crystal fiber

The last type of fiber investigated in the project is the photonic crystal fiber (PCF). Other names are sometimes used such as; micro-structured optical fiber, holey fiber, hole-assisted lightguiding fiber, and single-material fibers [54, 55]. The name comes from *photonic crystals*, which most often are constructed via periodic holes in bulk materials. A PCF can be defined as a fiber with a hexagonal array of air holes, within the cladding region of a fiber, and the core is defined by the vacancy of an air hole in the center of the array. The structure can be seen in Fig. 2.1. The distance between the holes is Λ and the hole diameter is d.

The idea of creating optical fiber using a single material and air as the cladding was proposed in the 1970s to avoid doping of the core, which at that time increased the loss of the optical fibers [6, 56, 57]. Relatively low loss single-mode guidance was achieved; however, diffi-

culties in the manufacturing process of the structure and successes of alternative methods halted the effort [58].

Interest was sparked again in 1996 when the stack-and-draw method was used to fabricate robust all-silica fibers [15] and theoretical predictions indicated that the fibers could be single-mode for all wavelengths (endlessly single-mode) in certain cases [55, 59]. These fibers are more complicated to draw than standard fibers but the refractive index contrast can be a factor of 10 better than Ge and F doped silica, and the refractive index profiles can be designed with unprecedented freedom. The core size and refractive index contrast can be extremely large or extremely small – whatever is desired. Large core single-mode fibers can handle high optical powers and are generally much better at mitigating nonlinear effects. Small core fibers can be engineered to achieve a high degree of nonlinearity, and are therefore called highly nonlinear PCFs. A side-effect of light propagating in a small core is that the chromatic waveguide dispersion is highly affected. Among others attributes, the important zero dispersion wavelength can be designed to be in the visible wavelength range and a second zero dispersion wavelength can be introduced. The confinement, scattering, and contaminant losses were sufficiently low already in the early stages of development of such fibers and have improved to approach the value of 0.2 dB/km at 1.55 μm for conventional fibers [60].

2.1.2 Supercontinuum generation in a PCF

A supercontinuum (SC) is formed by a complex cascade of linear and nonlinear processes that act together upon a pump pulse in order to cause extreme spectral broadening [13, 16]. There is no clear definition as to the extent of spectral broadening needed to classify such an effect as SC generation; however the bandwidth of an SC spans more than half a decade in most cases. SCs spanning the whole transmission window of silica (350-2600 nm) with an average power of several Watts have been generated [40].

The PCF is a particularly effective medium for SC generation due to the small mode area and the large design freedom of the chromatic dispersion. The most efficient SC generation occurs when the dispersion at the pump wavelength is anomalous because it promotes the formation of short duration solitons. This condition is obtained if the zero dispersion wavelength is below the pump wavelength. The formed solitons have a higher peak power than the pump and this enables a series of nonlinear processes in which wavelengths widely spaced from the pump can be generated. The bandwidth of the SC is ultimately limited by the

absorption loss in the medium used to generate it. For example, in silica it is difficult to generate a long wavelength edge of an SC above 2400 nm because of the rapidly increasing loss in silica above that wavelength [14].

The nonlinear processes in SC generation are described in detail in section 5.1 and optimization of dispersion properties of PCFs are discussed in section 5.6.

2.2 Rare-earth doped fiber lasers

The first fiber laser [7] was demonstrated in 1961 shortly after the demonstration of the first laser [2], which at that times was called an optical maser [1]. The word laser originated as an acronum which stands for *light amplification by stimulated emission of radiation*. It is a very different approach to the generation of light than in the classical picture, where light is generated by acceleration of charges. The amplification of light is possible by the process of stimulated emission, which relies on a non-equilibrated state corresponding to a laser transition. This non-equilibrated state is also called population inversion and occurs when the population of a upper or excited state is higher than the population in a lower state. The source that excites the gain medium to the upper state is called the pump.

Lasers are usually understood as being oscillators containing an amplification medium. The oscillator (also called optical resonator or cavity) is constructed by two reflective surfaces, which provide an optical feedback so that lasing can be sustained. A laser medium without an oscillator is a gain medium, which can be suitable for optical amplification.

2.2.1 The active material

The active ions used in fiber lasers are rare earth elements in the group of lanthanides, which, contrary to the sound of the name, are fairly abundant [61]. The lasing transition occurs via the $4f$-shell electons which enables lasing transitions with wavelengths from 455 nm to 3950 nm [61, 62]. The $6s$-shell is also populated, which shields these ions from the host material and results in long excited state lifetimes up to a few milliseconds. The rare earth elements used in fiber lasers are: Yb, Er, Tm, Ho, Nd, and Pr [62, 63]. From a technological perspective Er and Yb are the most important elements with a wide variety of applications in telecommunication and high power lasers, respectively.

The Yb ion has a unique advantage over the other rare earth ions in that the $4f$-shell is only missing a single electron. This prevents detri-

mental interactions between the different excited states, such as excited state absorption or non-radiative decay. It also leads to smaller differences in the pump and emission wavelength, which means that the efficiency of the laser can be exceedingly high [10]. In this project only fibers doped with Yb have been used due to the combination of high efficiency, the availability of powerful pump lasers, and an appropriate emission wavelength for SC generation. The other rare earth elements used in fibers also have exciting applications [62] but will not be addressed in this thesis.

The Yb^{3+} ion $\left([Xe]4f^{13}\right)$ has two energy level manifolds relevant for lasing; the ground state $\left({}^2F^{7/2}\right)$ and excited state $\left({}^2F^{5/2}\right)$, which are illustrated in Fig. 2.2. The population densities are also shown for the cases of population inversion and thermal equilibrium. The Stark and vibrational states in the ground state are populated in both situations because of thermal excitation at finite temperature. The excited state lifetime of Yb ions in silica is about 800 μs [64], which indicates that the ions are well isolated from the host.

With the emission of a photon with a wavelength of 976 nm the Yb ion must relax from an excited state into a highly populated ground state, and the Yb ion acts as a three level laser medium. To obtain population inversion at this emission wavelength a high pump power is in general needed. With the emission of a photon with a wavelength of 1064 nm the ion relaxes to a lower lasing level that is comprised of elevated vibrational states. These states have energies four times higher than the average thermal energy, and therefore thermal population of these states is in most cases quite low. This leads to a method by which the Yb ion can be treated as a quasi-four (quasi-three) level laser medium at an emission wavelength of 1064 nm, and hence the required pump power to reach population inversion is low.

The Yb ion is typically excited by an optical pump at a wavelength of 915 nm or 976 nm. When the wavelength of the pump is lower than 976 nm (corresponding to higher photon energy), the Yb ion is excited into vibrational states above the electronic excited state ${}^2F^{5/2}$. The Yb ion would then relax to the bottom of electronic excited state within less than a nanosecond by generation of phonons [61].

The transitions between the energy levels can be found experimentally by measuring the so-called absorption and emission cross sections. In Fig. 2.3 measured absorption and emission cross sections of Yb doped silica are shown. It can be seen the pumping band at 976 nm has a full-width at half-maximum (FWHM) of about 9 nm, which means that in many cases the pump wavelength must be stabilized. On the other

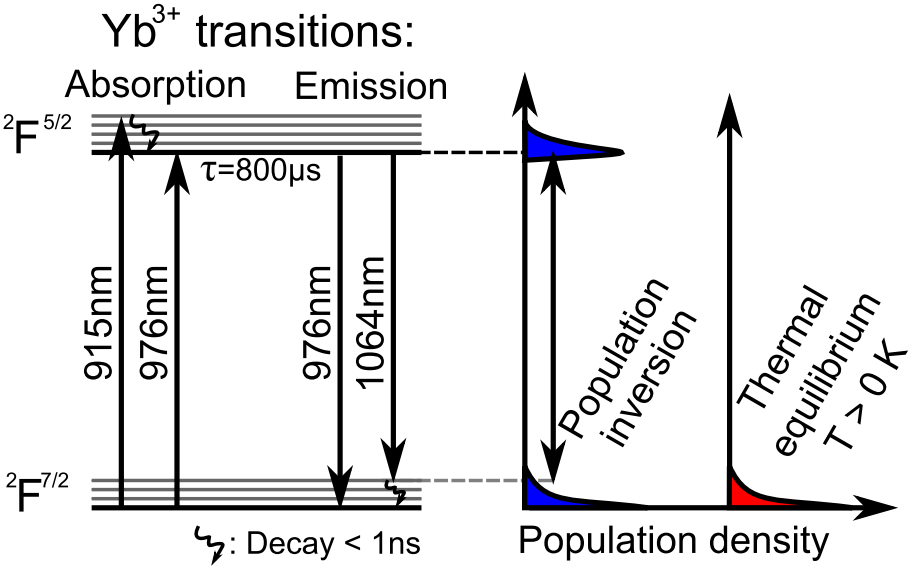

Figure 2.2: Energy level diagram and transitions of the Yb^{3+} ion. To the right the population density is illustrated at population inversion and at thermal equilibrium.

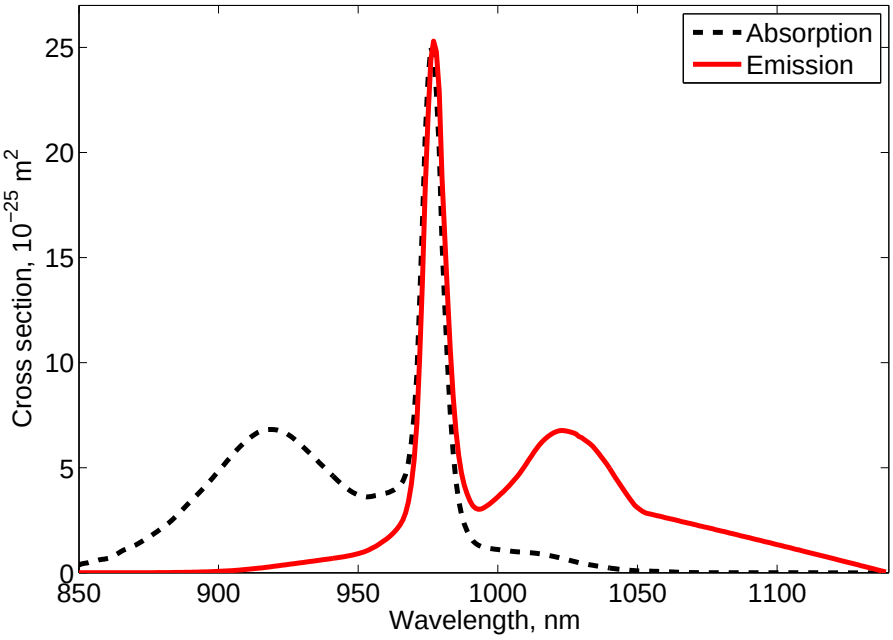

Figure 2.3: Absorption and emission cross section of Yb doped silica. [65, 66]

hand at the absorption shoulder at 915 nm the FWHM bandwidth is more than 50 nm and is practically insensitive to wavelength shift or bandwidth of the pump laser. The usable emission wavelength range is from 976 nm to beyond 1150 nm, which is considered very broad and is advantageous in ultra short pulsed lasers and tunable lasers.

2.2.2 Rare earth doped fibers

A fiber with rare earth doping is often called an active fiber. Doping of silica with Yb (and co-doping with Al) increases the refractive index of the glass and the core can be formed in this manner. Step index single mode active fibers with a core diameter up to 11 μm and NA down to 0.07 are commercially available [66, 67]. The NA can not under typical conditions be reduced further without lowering the Yb concentration. If a single mode fiber with a larger core diameter is needed the advantages of the PCF technology can be used to lower the NA below 0.03 [53] or a few-mode fiber can be coiled.

Active fibers can, depending on the application, be designed to be core pumped or cladding pumped. In Appendix B.2 the differences and the influence on the pump absorption efficiency are described. In summary, the core pumping is generally used when the emission power is below a few Watts, and for higher powers cladding pumping is advantageous due the increased fiber length and easily accessible high power pump diodes. In this thesis the focus is on Yb-doped silica fiber lasers with powers exceeding tens of Watts and therefore the cladding pumping scheme is applied.

Finally, it should be noted that many other types of lasers than the fiber lasers exist. Seen from a historical perspective the most used lasers are gas and solid state lasers, and fiber lasers have only been considered commercially relevant within the last 15 years [10,68]. Compared to the other types of lasers, the fiber laser has the following advantages:

- High total efficiency (especially for Yb)
- Large surface area to dissipate the generated heat
- Diffraction limited beam with low distortion in power scaling
- Broad gain bandwidth/tunable
- Cost-effective
- Robust to the operating environment
- Compact and maintenance-free

The disadvantages or challenges of fiber lasers are:

- The tight confinement that reduces the obtainable peak power due to nonlinearities
- Dispersion that can be detrimental for ultra short pulses
- Degradation can be problematic. This is called photo-darkening and the mechanisms are complicated and still controversial [69].

In Appendix B the current concepts and technologies behind fiber lasers will be described with the aim of introducing a non-expert reader to the terminology and various practical aspects. The output properties and way to measure them are also described.

2.3 Fundamental electromagnetism

The very foundation of optical modeling of light propagation within optical fibers is the Maxwell equations and the constitutive equations for non-magnetic and dielectric materials; [70]

$$\begin{aligned}
\nabla \cdot \mathbf{D}(\mathbf{r}, w) &= 0 && (2.3)\\
\nabla \times \mathbf{E}(\mathbf{r}, w) &= -i\omega \mathbf{B}(\mathbf{r}, w) && (2.4)\\
\nabla \cdot \mathbf{B}(\mathbf{r}, w) &= 0 && (2.5)\\
\nabla \times \mathbf{H}(\mathbf{r}, w) &= i\omega \mathbf{D}(\mathbf{r}, w) && (2.6)\\
\mathbf{D}(\mathbf{r}, w) &= \epsilon(\mathbf{E}(\mathbf{r}, w), \mathbf{r}, w)\mathbf{E}(\mathbf{r}, w) && (2.7)\\
\mathbf{B}(\mathbf{r}, w) &= \mu_0 \mathbf{H}(\mathbf{r}, w), && (2.8)
\end{aligned}$$

where $\mathbf{D}$ is electric displacement, $\mathbf{E}$ the electric field, $\mathbf{B}$ the magnetic induction, $\mathbf{H}$ the magnetic field, ϵ the permittivity, and $\mu_0 = 4\pi \cdot 10^{-7}$ Hm^{-1} is the vacuum permeability. Here the equation are expressed in the frequency domain for convenience[1]. The glory of the Maxwell's equations is the complete description of coupling between the electric and magnetic fields that can describe electromagnetic wave propagation.

The electric displacement describes the material response to an applied electric field and the induced electric polarization $\mathbf{P}$ in the material is defined through

$$\mathbf{D}(\mathbf{r}, w) = \epsilon_0 \mathbf{E}(\mathbf{r}, w) + \mathbf{P}(\mathbf{E}(\mathbf{r}, w), \mathbf{r}, w), \quad (2.9)$$

[1]Functions in the time-domain are denoted with a tilde. The definition of the Fourier transform used is $f(\omega) = \mathcal{F}\{\tilde{f}(t)\} = \int_{-\infty}^{\infty} \tilde{f}(t) exp(i\omega t) dt$.

where $\epsilon_0 = 8.854...\cdot 10^{-12}$ Fm^{-1} is the vacuum permittivity. In general $\mathbf{P}$ depends on $\mathbf{E}$ in all space and past time (positive and negative frequencies). Non-local effects such as thermal diffusion, which can be relevant in very low NA active fibers [71], are in the content of this project neglected. On the contrary, the nonlinear effects that arise due to higher order powers of the electric field, are crucial. A first approximation is to include the nonlinear induced polarization $\mathbf{P}_{NL}$ as a perturbative term:

$$\mathbf{P}(\mathbf{E}(\mathbf{r}, w), \mathbf{r}, w) = \mathbf{P}_L(\mathbf{r}, w) + \mathbf{P}_{NL}(\mathbf{E}(\mathbf{r}, w), \mathbf{r}, w). \tag{2.10}$$

The components of the nonlinear induced polarization will be treated thoroughly in section 2.5, where nonlinear propagation is discussed. It has also been assumed that the linear part is instantaneous, which generally is a good approximation at non-resonant frequencies. Silica is amorphous and therefore isotropic, which means that the linear scalar susceptibility $\chi^{(1)}$ can be introduced as

$$\mathbf{P}_L(\mathbf{r}, t) = \epsilon_0 \chi^{(1)}(\mathbf{r}) \mathbf{E}(\mathbf{r}, t). \tag{2.11}$$

From this the relative permittivity $\epsilon_r(\mathbf{r}) = 1 + \chi^{(1)}(\mathbf{r})$ can be defined.

2.3.1 The wave equation

The wave equation can be derived by taking the curl of Eq. (2.4) and combining the result with Eq. (2.6), which yields

$$\nabla \times (\nabla \times \mathbf{E}) = \mu_0 \epsilon_0 \omega^2 \mathbf{E} + \mu_0 \omega^2 \mathbf{P}. \tag{2.12}$$

Inserting the induced polarization and using that the speed of light is $c_0 = (\mu_0 \epsilon_0)^{-1/2}$ and the wavenumber $k_0 = \omega / c_0$, we then have

$$\nabla \times (\nabla \times \mathbf{E}) - \epsilon_r k_0^2 \mathbf{E} = \mu_0 \omega^2 \mathbf{P}_{NL}. \tag{2.13}$$

The left hand side is the general wave equation and the nonlinear induced polarization term on the right hand side acts as a source term. Solving this is quite involved due to the vectorial nature. When the nonlinearity can be neglected a full vectorial eigenproblem solver can be used to find the eigenmodes, and this procedure will be described section 2.4.

It has been shown that the problem can be simplified in the case of *weakly guiding fibers*[2], which obey the relation [72]

$$(n_c - n_{cl})/n_{cl} \ll 1, \tag{2.14}$$

[2]This should not to be confused with leaky fibers, where losses are high.

The results imply that the modes have linear polarization states and are mostly transverse to the direction of propagation. Wave propagation is therefore analogous to plane waves solution [73]. One might think that the approximation is not valid for a silica strand in vacuum (an extreme PCF) because of $(n_c - n_{cl})/n_{cl} = 1/3$. However, the validity in this case has been confirmed by full vectorial numerical calculations, which show that the longitudinal components of the fundamental mode are very small compared to the transverse field components. The weakly guiding approximation implies that the divergence of $\mathbf{E}$ can be simplified to

$$\nabla \cdot \mathbf{E} = \epsilon_r^{-1}\mathbf{E} \cdot \nabla\epsilon_r(\mathbf{r}) \approx 0, \tag{2.15}$$

hence the wave equation can be written

$$\nabla^2\mathbf{E} + \epsilon_r k_0^2\mathbf{E} = -\mu_0\omega^2\mathbf{P}_{NL}. \tag{2.16}$$

It is convenient to separate the problem into a static transverse problem and a (nonlinear) propagation problem, to which we may submit a solution on the following form; [74, 75]

$$\mathbf{E}(r,\omega) = \frac{1}{2}\hat{\mathbf{x}}N\Big(\psi(\mathbf{r}_\perp,\omega)A(z,w)e^{i\beta_0 z} + c.c.\Big), \tag{2.17}$$

where *c.c.* is the complex conjugate, $N = (0.5\epsilon_0 c_0 n)^{-1/2}$, ψ is the normalized transverse field, A the envelope function of the propagating field with the instantaneous optical power $\tilde{P}(z,t) = |\tilde{A}(t)|^2$, and $\beta_0 = \beta(\omega_0)$ is the propagation constant of the carrier wave with angular frequency ω_0. Only the polarization state in the $\hat{\mathbf{x}}$ direction is considered. It is not strictly necessary to limit the polarization state but it is common in nonlinear propagation to reduce the complexity of the often computationally heavy simulations as will be touched upon in section 2.5.

The separation of variables method is now done in the linear regime and a separation constant β_s is introduced. Two independent homogeneous differential equations are obtained [75]

$$\nabla_\perp^2\psi + (k_0^2\epsilon_r - \beta_s^2)\psi = 0 \tag{2.18}$$

$$\frac{\partial^2 A}{\partial z^2} + 2i\beta_0\frac{\partial A}{\partial z} + (\beta_s^2 - \beta_0^2)A = 0. \tag{2.19}$$

The nonlinear contributions to the refractive index[3] can reach 10^{-3} in extreme but realistic situations. This hardly affects the transverse mode

[3] Using $\underline{n}_2 = 2.6 \cdot 10^{-20}$ m^2/W, a peak power of 100 kW, and core diameter of 2 μm.

(of a typical nonlinear PCF) but has huge implications on propagation. This justifies separation and the two problems can be solved independently. In the transverse problem the propagation constant can be renamed $\beta_s(\omega) \rightarrow \beta(\omega)$ and the solution is presented in section 2.4. The nonlinearities are included in $\beta_s(\omega)$ through a perturbation, which will be described in section 2.5.

2.4 The transverse problem

Fundamental to understanding propagation in waveguides is the ability to solve the transverse problem. Analytic solutions are rare [72], even in the simple case of e.g. the step index fiber, and numerical methods need to be applied. Popular numerical methods are finite difference, finite element method, and plane wave expansion [54]. The best approach depend on the problem, and in this project the finite element method is applied due to the maturity, the ability to setup an arbitrary structure, the accuracy, and the ability to estimate the confinement loss through the use of absorbing boundary conditions. The software packages COMSOL Multiphysics® version 3.4 and Matlab® version 2010 were used. The full vectorical eigenvalue problem is defined in COMSOL as;

$$\nabla \times (\epsilon_r^{-1} \nabla \times \mathbf{H}) - k_0^2 \mathbf{H} = \mathbf{0}, \quad \mathbf{H} = \mathbf{H}(x,y)e^{uz}, \quad u = -i\beta - \delta, \tag{2.20}$$

which can be obtained directly from Maxwell's equations. The full vectorial problem is solved instead of the scalar problem in Eq. (2.18) to ensure that the most accurate dispersion is found for all wavelengths and all structures [76]. The eigenvalue u and the eigenvector $\mathbf{H}$ are found by the SPOOLES eigenproblem solver and typically 6 eigenvalues are found.

In Fig. 2.4 the total domain of the calculation is shown together with the computational grid. The outermost border consists of an absorbing and non-reflecting layer to attenuate the field – the so-called perfectly matching layer. The air holes are distributed all the way to the perfectly matching layer to avoid situations in which the solver may find modes in that region with similar mode area and effective index to that of the fundamental mode. The symmetry of the structure is six fold, which dictates that the fundamental mode has a similar symmetry. This makes it possible to reduce the computational domain. Four-fold symmetry can easily be implemented in the solver by selecting appropriate boundary conditions, and is used in the modeling but is not shown in the figures. This simplification reduces the computational time and memory demand by more than a factor of four. In the right section of Fig. 2.4, the grid

is shown and the grid density is enhanced in the core region to increase the number of computational points where the field amplitude is high.

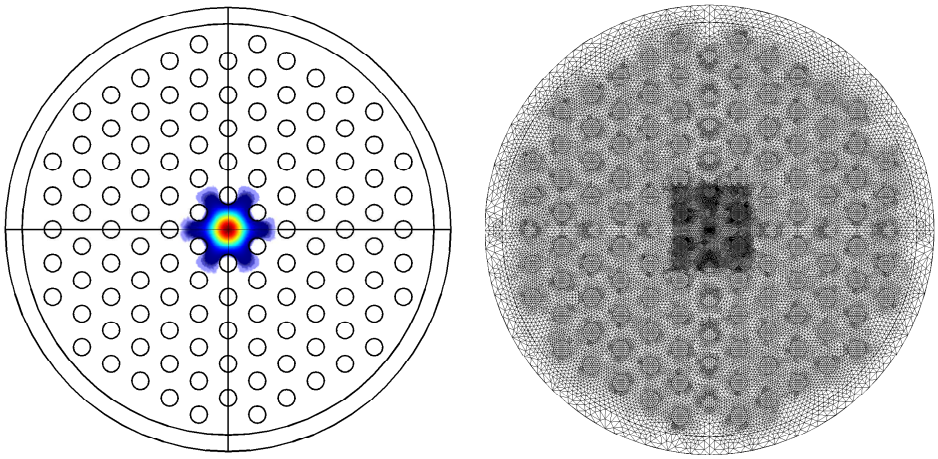

Figure 2.4: *Left:* Structure and electric energy density of the fundamental mode. *Right:* Computational grid with improved density in the core region. The x- and y-symmetry axes are indicated.

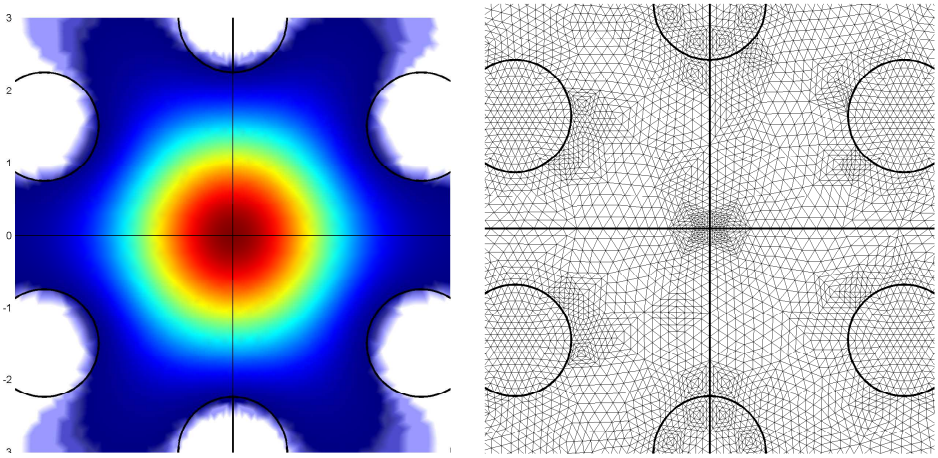

Figure 2.5: *Left:* Core structure and electric energy density of the fundamental mode. *Right:* Computational grid in the core region. The x- and y-symmetry axes are indicated.

In Fig. 2.5 only the core region is shown, and it can be seen that the fundamental mode has a hexagonal symmetry and that the power density is very low in the air holes. The mode avoids the air hole to maximize the effective refractive index. The field mostly interacts with the first ring of air holes, and therefore the size of these holes is the most

important factor for the waveguide properties.

The dispersive and nonlinear properties of a PCF must in general be solved numerically for a given pitch and hole size. Some general guidelines will be given in section 5.6 where the common parameter space of PCFs are modeled and analyzed.

2.5 The propagation problem

The solution to the linear propagation problem in Eq. (2.19) is given by

$$A(z,\omega) = A(0,\omega)e^{i(\Re[\beta(\omega)]-\beta_0)z}e^{\Im[\beta(\omega)]z}, \tag{2.21}$$

where $\Re$ and $\Im$ take the real and imaginary components, respectively. It is seen that the real part of $\beta(\omega)$ determines the phase for each frequency component independently, which in the time domain translates into pulse broadening in the case of finite dispersion of β. This is in general referred to as chromatic dispersion, which is crucial in SC generation and will be discussed in section 5.1.

The imaginary component acts as exponential attenuation or amplification depending on the sign of the exponential term. Different contributions enter into to the propagation loss: confinement, scattering, absorption due to impurities, and point losses (splices) [77]. The loss in nonlinear PCFs and active fibers are in general very low, and inclusion of loss is only relevant in this project in the case of broad SC reaching the scattering loss edge at < 400 nm or the OH absorption at $\sim$2400 nm [77, 78].

In case of semi-classical modeling of lasers the amplification factor $\Im[\beta(\omega)]$ is given by the product of the emission cross section and the population inversion density. This approach to modeling of gain will be used in section 3.3.

2.5.1 The nonlinear induced polarization

A nonlinearity, due to an applied electric field, can in general be described by the anharmonicity of the atomic potential of the nuclei at large field amplitudes [4]. It acts as a source in the propagation equation through nonlinear induced polarization, which can be split in power of the electric field as

$$\tilde{\mathbf{P}}_{NL}(\mathbf{r},t) = \epsilon_0 \sum_{k=2}^{\infty} \chi^{(k)} \tilde{\mathbf{E}}(\mathbf{r},t)^k. \tag{2.22}$$

In silica the strongest higher order term is the third in the series, because silica is isotropic and the even order vanishes [12]. Much less pronounced

phenomena arise from interfaces and defects that can induce anisotropic contributions and from other higher order terms [4, 79–81].

In silica the nonlinear response can arise from elastic and inelastic scattering. The electronic response, termed the Kerr nonlinearity in $\chi^{(3)}$-materials, is elastic and is considered instantaneous. Responses characterized as inelastic scattering involves generation of optical or acoustic phonons. The optical phonon interaction is called stimulated Raman scattering and has a delayed response on the order of ~ 50 fs time scale. The acoustic phonon interaction called stimulated Brillouin scattering has time response of >1 ns, and is relevant for coherent CW pumps i.e. lasers having a narrow spectral bandwidth of ~ 10 GHz or ~ 0.05 nm at 1064 nm. Such pump sources are not used in the project and stimulated Brilloiun scattering will be neglected for the rest of this thesis.

The third order induced polarization can be written;

$$P^{(3)}_{i,NL}(\omega) = \epsilon_0 \iint \chi^{(3)}_{ijkl}(\omega; \omega_1, -\omega_2, \omega_3) \vdots \mathbf{E}_{\omega_1} \mathbf{E}^*_{\omega_2} \mathbf{E}_{\omega_3} d\omega_2 d\omega_3, \qquad (2.23)$$

where $\chi^{(3)}_{ijkl}$ is an 81 elements tensor, $\{i, j, k, l\}$ are either x, y, or z, $\omega_1 = \omega - \omega_2 + \omega_3$, and the integration over all frequencies is carried out to take all interactions into account. In silica $\chi^{(3)}$ can be reduced to three independent elements due to rotational symmetry. Furthermore, in case of linear polarized electric fields ($\mathbf{E} = \hat{\mathbf{x}} E_x$) only the element $\chi^{(3)}_{xxxx}$ survives. This is advantageous because the complexity of the calculations is reduced but is strictly only valid in situations where only one polarization is guided. However, it is a fair approximation in the case of randomly polarized light or where the linear polarization is rapidly degraded [82].

2.5.2 The GNLSE model

In order to solve the nonlinear propagation problem in Eq. (2.19), the small nonlinear perturbation is introduced as $\beta_s^2(E) = \beta^2 + \Delta\beta(E)^2$ [12, 75]. The model is called the generalized nonlinear Scrödinger equation (GNLSE). The derivation is lengthy [12, 75] and only the crucial approximation will be discussed here.

A great simplification to the problem is realized by reducing the equation from second order to first order by factoring it into components describing both forward and backward propagation and neglecting the components for backward propagation [75]. This is not the same approach as the slowly varying envelope approximation, which has ques-

tionable validity in the case of SC generation, due to a requirement of the bandwidth to be less than 1/3 to the carrier wave frequency [83].

As the SC spectrum can span from 350-2600 nm [40], it is important not only to include the chromatic waveguide dispersion but also the dispersion of the strength of the nonlinearity. This is done by taking into account the dispersion of the effective area [84] and approximating the dispersion of $\chi^{(3)}$. The dispersion of the effective area $A_{\text{eff}}(\omega) = (\int \psi^2 dxdy)^2 / \int \psi^4 dxdy$ is included by scaling the field as

$$C(z,\omega) = A(z,\omega)\left\{\frac{A_{\text{eff}}(\omega_0)}{A_{\text{eff}}(\omega)}\right\}^{1/4}. \tag{2.24}$$

The coordinate system is transformed to be following the carrier group velocity, hence a dispersion operator is defined

$$\hat{D} = i\{\beta(\omega) - \beta(\omega_0) - \frac{\partial\beta(\omega)}{\partial\omega}\Big|_{\omega_0}[\omega - \omega_0]\} - \frac{1}{2}\alpha(\omega), \tag{2.25}$$

where α is the attenuation. In order to solve the equation efficiently, the so-called interaction picture is used, and C is transformed as [42, 85]

$$C_I = \exp\{-\hat{D}(\omega)z\}C. \tag{2.26}$$

We then arrive at the final GNLSE [42, 86]

$$\frac{\partial C_I}{\partial z} = i\gamma(\omega)\frac{\omega}{\omega_0}e^{-\hat{D}z}\mathcal{F}\Big\{\tilde{C}\mathcal{F}^{-1}\big[R(\omega-\omega_0)\mathcal{F}(|\tilde{C}|^2)\big]\Big\}, \tag{2.27}$$

where $\tilde{C}(z,t) = \mathcal{F}^{-1}\{C(z,\omega)\}$. The response function R contains the instantaneous Kerr and the delayed Raman contribution as

$$R(\omega) = (1-f_R) + f_R\frac{\tau_1^2+\tau_2^2}{\tau_2^2 - \tau_1^2(i+\tau_2\omega)^2}, \tag{2.28}$$

where f_R is the relative strength of the Raman interaction and is close to 0.18. The Raman response function is approximated as a damped oscillator with $\tau_1 = 12.2$ fs and $\tau_2 = 32$ fs [87].

The dispersion of the effective area is included in the nonlinear parameter $\gamma(\omega)$, which is defined [88]

$$\gamma(\omega) = \frac{\omega_0 \underline{n}_2 n_{\text{eff}}(\omega_0)}{c_0 n_{\text{eff}}(\omega)\sqrt{A_{\text{eff}}(\omega)A_{\text{eff}}(\omega_0)}}, \tag{2.29}$$

and by ignoring the frequency dependence the usual form $\gamma = \frac{\omega_0 \underline{n}_2}{c_0 A_{\text{eff}}(\omega_0)}$ is retrieved. The nonlinear refractive index $\underline{n}_2$ is then defined for silica as

$$\underline{n}_2 = \frac{3}{4}\frac{\chi^{(3)}_{xxxx}}{n_{\text{eff}}^2 \epsilon_0 c_0} \approx 2.6\cdot 10^{-20}\ \text{m}^2/\text{W}. \tag{2.30}$$

The nonlinear refractive index can be increased to $5 \cdot 10^{-20}$ m^2/W when the material composition is altered by doping with Ge [75, 89, 90].

The implementation of the GNLSE used in this thesis is based on the fourth-order Runge-Kutta method in the interaction picture with adaptive step size [85, 91, 92]. Details on this approach can be found in [38].

Chapter 3

Gain-switching of fiber lasers

In this chapter gain-switching (GS) of fiber lasers is investigated theoretically. First a qualitative explanation of the physical mechanisms of GS is given. A review of GS of fiber lasers in the literature are presented with focus on Yb-doped fiber lasers. The governing equations and modeling using a detailed and a simplified model are described. Insight to the fundamental physics behind the GS process and general trends will be described.

3.1 Gain-switching

GS is a technique for pulse generation by fast modulation of the laser gain via modulation of the applied pump. A pulse is generated by releasing stored energy within the gain medium, which must be released before the equilibrium between the pump rate and emission rate can be reached. This unstable behavior is fundamental for all lasers and is called relaxation oscillations or spiking. Relaxation oscillations were observed in the very first lasers made in 1960 [93,94] and several theories on the subject were developed simultaneously [95–98]. The phenomenon is mostly seen as unwanted due to the noise-like nature [99]. The idea of taking advantage of them by repetitively pulsing the pump was first published in 1968 [100] and has since been applied to most types of lasers; including fiber lasers [51].

The relaxation oscillations are described by the transient coupling of the population inversion and the photons in the cavity. The dynamics are illustrated in Fig. 3.1 and will be presented in a step-by-step manner to reveal the rich details;

1. In the initial state there is no population inversion nor light in the

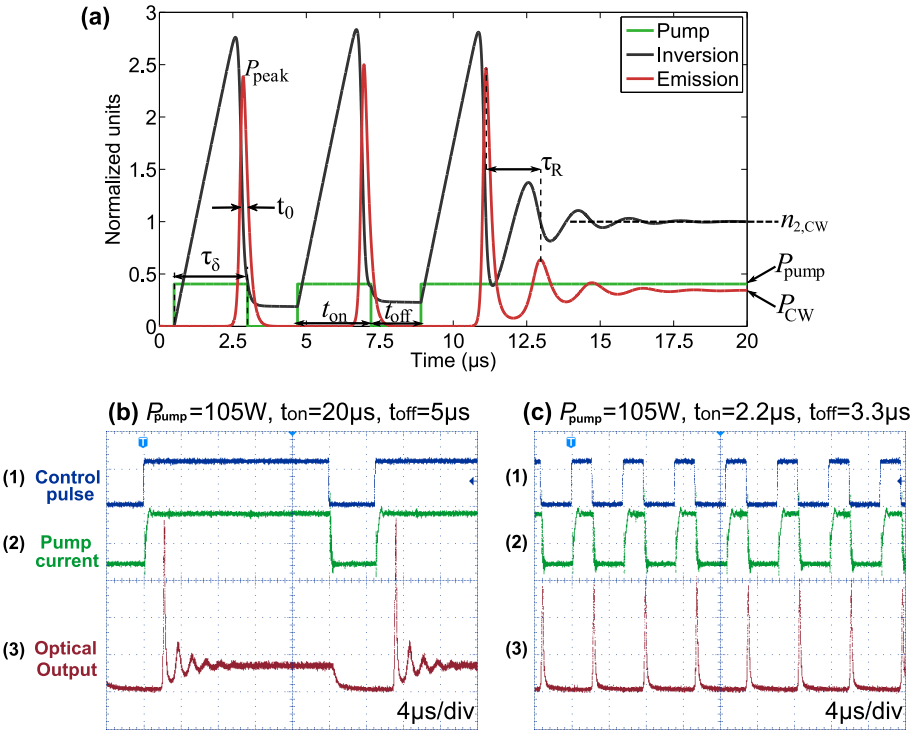

Figure 3.1: Modeled and experimental transient behavior of a fiber laser. In (a) the transient behavior is illustrated and the characteristic parameters are defined: the build-up time (or delay) τ_δ, relaxation oscillation period τ_R, pump power P_{pump}, first optical pulse spike peak power P_{peak}, optical pulse full width half maximum width t_0, CW power level P_{CW}, pump pulse duration t_{on}, and off-time t_{off}. The dynamics are simulated using the point model described in section 3.6. In (b) and (c) experimental oscilloscope traces of the electronic on/off modulation and fiber laser output are shown. (b) shows the relaxation oscillation regime ($t_{on} \gg \tau_\delta$). (c) shows the GS regime for which $t_{\mathrm{on}} \approx \tau_\delta$. The fiber laser is with configuration A (see section 4).

cavity.

2. Pumping starts to build up population inversion and the cavity is mainly filled with low power spontaneous emission.

3. As pumping continues, the population inversion is increased almost linearly with time and lasing starts by amplification of the spontaneous emission.

4. The increasing optical power in the cavity begin to deplete the population inversion and the front of pulse appears at the output.

5. The population inversion is decreased below the threshold and the generated pulse has reached its peak value. The pumping is normally stopped at this time to avoid emission of additional pulses. The full train of relaxation oscillations that occur with continued pumping is shown in 3.1(a) (after 10 μs) and 3.1(b).

6. The cavity is gradually emptied and the tail of the pulse is emitted. The population in the upper state will decrease slowly with a rate determined by the lifetime of the excited state.

7. The cycle is repeated to produce the next pulse.

In Fig. 3.1(a) definitions of characteristic parameters are given. The build-up time τ_δ is the time between when the pump is turned on and the first spike peaks. The oscillation period of the relaxation oscillations is τ_R. For a given pump power P_{pump} a certain peak power of the first spike P_{peak} is obtained and the duration of this spike is defined as the full width half maximum t_0. When the pump is off for a time period of t_{off} the cavity is emptied. The process repeats with the repetition rate $f^{-1} = t_{\text{off}} + t_{\text{on}}$ and the duty cycle is defined $ft_{\text{on}} \cdot 100\%$. If the pump pulse width t_{on} is much longer than the decay of the relaxation oscillations the laser goes into CW operation with an output power of P_{CW} and population inversion level of $n_{2,CW}$, as can be seen after $\sim$15 μs.

In Fig. 3.1(b) experimental results show the transient behavior of the fiber laser after fast turn-on of the pump and relaxation oscillations are present before the laser goes into CW operation. In Fig. 3.1(c) the pump pulse width is selected such that only the initial spike is generated without the train of relaxation oscillations and the fiber laser operates in a GS mode of operation.

In Fig. 3.2 a phase plot of the process is shown using the same simulation process as in Fig. 3.1(a). Stable and efficient GS is obtained

when the phase circles are coinciding and as open as possible, which means that for each repetition the population inversion reaches the same maximum level that leads to the same maximum instantaneous (peak) power. In Fig. 3.2 the phase circles do not overlap perfectly because too few repetitions have passed in order for the laser to have stabilized. When pumping is continued the relaxation oscillations can be seen as a spiral, which eventually falls to a center point which coincides with the CW state.

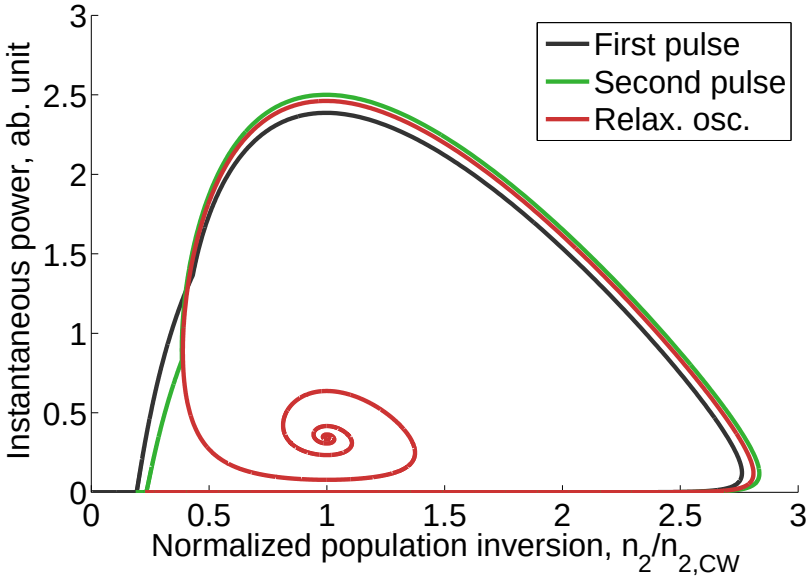

Figure 3.2: Phase plot of GS and relaxation oscillations. The simulation is identical to Fig. 3.1(a).

The population inversion density and the density of photons in the cavity are coupled by rate equations in which the term describing the stimulated emission process contains the product of the two densities. In this sense the problem is nonlinear; therefore, unstable solutions exist. With a given set of input parameters, a lack of or multiple pulses per repetition can occur, which is called bifurcation and is studied in Refs. [101, 102]. This dynamic is important to have in mind, when high stability of the fiber laser is required. For most practical purposes it can be avoided by ensuring that the cavity is emptied sufficiently before pumping starts.

3.2 Review of gain-switching of fiber lasers

In the first experiment with a fiber laser carried out in 1961, an Nd-doped fiber was pumped with pulses from a flash lamp [7], and was therefore the first account of GS in a fiber laser, even though the output was only noted as "ringing". The first systematic study was published in 1989, where an Nd-doped fiber was pumped by a dye laser at 590 nm [51] with square and sinusoidal pulses. Fiber lengths between 1 cm and 7 m were tested. The configuration, in which square (on/off) pulses were used, was observed to be the most stable. The pulse duration at the shortest fiber length was 40 ns [51].

A series of papers showed unstable gain-switching of Nd-doped, Tm-doped, Er-doped, and Yb-Er-codoped fiber lasers [103–107]. The reason for the unstable behavior was that the pump photon energy was much higher than the emission photon energy, which is called out-of-band pumping [107, 108]. Unwanted temporal structures and instabilities occurred because the rare earth ions were pumped to a high energy level, which decayed to the upper lasing level on the same timescale as that of GS dynamics [107, 108]. Note, that as the Yb ion only has a single electronic transition (see section 2.2), these complication do not apply in Yb-doped fiber lasers.

Single pulse and stable GS of a Tm-doped fiber laser was demonstrated in 2007 [109, 110], where in-band pumping of the Tm ion was achieved via a pulsed 1.55 μm Er-doped fiber laser. The peak power reached over 1 kW and the shortest pulse duration was 10 ns due to a short fiber length of 25 cm. In [111] a peak power of 8 kW and a pulse duration of 1.5 ns at 20 kHz was achieved in a Tm-doped fiber with a length less than 50 cm. In [112] the pump power was increased by using a cladding pumped Er-doped amplifier, and this resulted in repetition rates of 300 kHz with pulse duration at 25 ns and peak power of 1 kW. Other realizations were Tm-doped fiber in a ring cavity [113] and a Tm-doped fiber laser pumped by an Er-Yb-doped fiber laser modulated by an acousto-optic modulator [114]. Recently, a Tm-Ho-doped fiber laser was gain-switched, and influence on the pulse duration and peak power of the fiber length and output coupling was investigated [115].

In 2007 results from the first gain-switched Yb-doped fiber laser was published [116]. The pump was a single-mode laser diode, which had a much lower peak power than the Er-doped fiber lasers used for pumping of Tm-doped fibers, and the peak power in this investigation reached 43 mW with a pulse duration of 200 ns [116]. The laser cavity was of the distributed feedback type and the length of the fiber was 5 cm. In [117] the double-clad pumping scheme was used and the required fiber length

was 3.5 m. This setup enabled a peak power of more than 100 W, a pulse energy of 16 μJ, and a duration of 130 ns at 25 kHz [117]. The involved physics and the influence of repetition rate and pump pulse energy on the build-up time, pulse duration, and pulse energy were investigated in [118]. Using a 12.5 m Yb-doped fiber a pulse energy of 36 μJ and duration of 1.4 μs at 50 kHz was achieved [118]. In [119] GS of a 9 m Yb-doped fiber laser was characterized and analyzed numerically. The model did not reproduce the experimental results quantitatively. A peak power of 60 W, pulse duration of 1 μs and a pulse energy of 30 μJ were obtained at $\sim$10 kHz [119].

Since the start of this project three articles, much in line with this thesis, have been published [120–122]. A numerical model and accompanying experiments of a cladding pumped Yb-doped all-fiber laser are presented in [120,121]. In [122] power scaling has been carried out using a fiber with a larger core and higher pump power, and the resulting peak power reached more than 2 kW with a pulse duration of 60 ns. These results are highly relevant for the results obtained in the project and will be included in the discussion.

As a summary, the study of stable GS of fiber lasers is a rather new field and the configuration simultaneously achieving the highest peak power and shortest pulse duration to date is that of Tm-doped fiber lasers pumped with a pulsed 1.55 μm source. This type of GS has been reviewed recently [108, 123]. There are a handful of articles on GS of Yb-doped fiber lasers, and interest seems to be growing.

Another field with growing interest is the hybrid pumping scheme based on out-of-band CW cladding pumping and in-band pulsed core pumping acting as a trigger [124]. This started in 2010 with a Tm-doped fiber laser pumped at 793 nm and 1914 nm, which resulted in an average power of 100 W and 2 mJ pulses with a duration of 1 μs at 50 kHz [125]. By reducing the repetition rate to 0.5 kHz the pulse energy increased to 10 mJ and the pulse duration was decreased to 75 ns, which corresponded to peak power of more than 130 kW. An all-fiber laser based on the hybrid pumping scheme was developed in [126], where pumps were at 790 nm and 1053 nm, and a pulse energy of 2 mJ and a pulse duration of 500 ns were achieved. By taking advantage of stimulated Brillouin scattering the pulses could be narrowed to 20 ns, which corresponded to a peak power of more than 100 kW [124,127]. Recently, hybrid pumping has been applied to Yb-doped fibers, where the pumps are at 976 nm and 1064 nm, and the emission is at 1120 nm [128]. This scheme has also been developed as a dual-cavity arrangement, where a peak power of 1.4 kW in 45 ns pulses with pulse energy of 62 μJ is obtained [129, 130].

Yet another field is cascading of gain-switched fiber lasers, such as in [102, 131] where an Er-doped fiber laser is used to pump a gain-switched Tm-doped laser, which in turn is used as a pump source for a gain-switched Ho-doped fiber laser. Furthermore, a few articles describe more complicated scenarios related to GS [101, 132–135].

Here, only results of GS of fiber lasers are presented, however GS of semiconductor diode lasers has also been studied in e.g. [136, 137], and can be used as seeders for fiber amplifiers as in [138]. The fundamental physics are the same, but the length scales of the cavity and the energy transitions are not comparable and will not be discussed further.

3.2.1 Alternatives to and advantages of gain-switching

Several alternative techniques of pulse generation have been developed based on various physical principles [99]. The most common techniques are mode-locking and Q-switching, but external modulation of a CW laser, self-pulsation, and amplification of a modulated diode laser are also relevant to consider. The results from GS of fiber lasers described above can hardly compete with e.g. Q-switched fiber lasers where peak power >100 kW and pulse duration <10 ns is achieved routinely [10, 139–142].

The motivation for heading towards GS fiber lasers are that they can be built to be completely fiber-integrated, which is in contrast to common Q-switched or mode-locked lasers that require free-space coupling to for instance an acousto-optical modulator [143–146]. A completely monolithic system is desired in many applications because it has the advantage of being mechanically and thermally robust, cost-effective, and compact. Maybe more importantly, the devices are turn-key and can be operated by untrained personnel.

Several methods of pulsing all-fiber lasers have been examined but it turns out to be rather challenging. A few examples of such pulsed fiber laser are listed here; Femtosecond pulses can be produced by mode-locking through the use of nonlinear polarization rotation [147]. Active Q-switching has been achieved by detuning the cavity through elongation of one of the fiber Bragg gratings [148, 149]. Passive Q-switching has been demonstrated with specially-doped or standard small-mode-area saturable absorber fibers [150, 151]. The fiber geometry allows for a very high single pass gain of more than 50 dB, which is advantageous in amplifiers. However, the high gain increases the requirements for the contrast of a Q-switching element [10] and is the origin of often destructive self-pulsation [152]. Compared to these results, the GS of

fiber lasers has the advantage of being highly effective, having a simple construction, and being able to generate high energy pulses.

The closest alternative technique to GS is Q-switching and they are sometimes confused [153]. The similarities and differences will therefore be pointed out. GS is related to Q-switching in the way that the pulses grow from spontaneous emission within the nanosecond time scale. The major difference is the time available for pumping [99]. In GS the gain medium can only be pumped for a short time interval, typically a few microseconds, before the pulse builds up. This is in contrast to Q-switching, where the pump time can be as long as the lifetime of the upper state, which for rare earth doped glasses is hundreds of microseconds. This means that the pump (peak) power requirement for applying GS is more than an order of magnitude higher. However, GS is increasingly interesting due to the decreasing cost of pump diodes, the all-fiber construction and no need for specialty components [10].

3.3 Modeling approach

Theoretical modeling and numerical simulations are important to understand the dynamics and characteristics, and to optimize the system parameters for a particular application. A laser is inherently a deeply quantum mechanical device, however a complete description is seldom necessary. The dephasing rates of excited rare-earth elements at ambient temperature are fast, hence coherent quantum optical effects can be neglected (except stimulated emission of course) [154]. This justifies the use of rate equations to describe only a few discrete energy levels as thoroughly derived in [154,155]. This approach is therefore semi-classical and is rigorously derived under the approximation that the population inversion changes slowly compared to $\omega/2\pi$, and that the change in the refractive index due to the redistribution of the electrons in the ions can be neglected [155].

The quantitative description of the process of GS is quite involved due to the linear growth of the population inversion and simultaneous exponential amplification of spontaneously emitted photons (ASE), which reduces the population inversion. This problem is nonlinear and no analytic solution exists. Two approaches are chosen in order to solve the dynamics of GS of a fiber laser.

Firstly, a detailed model that couples the propagation equation of the optical power and the rate equation of the population inversion is solved numerically using a finite difference scheme. The level of approximations are kept very low to make the model as accurate as possible,

but this comes at the expense of computational speed. The variation of the population inversion with length and radial position is taken into account and an arbitrary number of ASE wavelengths and transverse modes can be calculated. The pump is modeled as forward and backward propagating powers as is the signal and ASE wavelengths. This means that pump saturation effects are also taken into account.

Models with this amount of detail are described in [151, 156] where they are applied to an Er-doped planar ring waveguide and all-fiber passive Q-switching, respectively. Similar models have been solved in the steady state in [157–159]. A detailed model has recently been applied to GS of fiber lasers [120, 121, 123, 160] except that the pump is not propagated and the radial dependence is neglected. The model used is similar to those found in [161, 162], where Q-switching of fiber lasers has been investigated. Studies on Er-doped and Yb-Er-codoped fibers have shown that the radial dependence can have a significant effect on amplification [158, 163, 164], and the model developed and implemented in this project will be able to tell if this concerns GS. Furthermore, the spontaneous emission that seeds the pulse is examined in detail.

A second and simpler model is also developed. Here the population inversion and the photon density are assumed to be homogeneously distributed in the core and along the length of the cavity. The advantage of this is that it can be solved by simple numerical integration and a linear stability analysis can be carried out analytically. The outcome is an expression for the relaxation oscillation period and from this the pulse duration can be defined. It is based on the early solutions to the rate equations of the laser [96, 98] and a similar approach has been applied to GS in [51, 100, 165, 166]. This model is derived here to validate the approximations in the specific case of the cladding pumping scheme and to test the accuracy of the approach.

3.4 The detailed model

It is possible to solve the propagation equation in Eq. (2.5) for example by the finite difference or split-step method [71]. However, the process of GS does not rely on any phase relation between the longitudinal modes as does for example mode-locking. It is therefore a good approximation to only consider the propagation of the optical power. Such a model is called a traveling wave model and is used widely within simulations of fiber lasers and amplifiers [146, 151, 157–159, 162].

The coupling of light with the energy level population is handled through absorption and emission cross sections. They are defined as the

change in the intensity $I_\omega(\mathbf{r},t)$ at angular frequency ω with propagation distance z as

$$\frac{dI_\omega}{dz} = \{N_2\sigma_{e\omega} - N_1\sigma_{a\omega}\}I_\omega - \alpha_\omega I_\omega + \eta_{\omega,\mathrm{SE}}\frac{N_2\hbar\omega}{\tau_2}, \tag{3.1}$$

where $N_2(\mathbf{r},t)$ and $N_1(\mathbf{r},t)$ are the number density of atoms in the upper and lower lasing level, respectively, α_ω is the loss at the angular frequency ω, $\hbar\omega$ is the photon energy, and τ_2 is the upper state lifetime. The last term is spontaneous emission, which does not depend on the intensity. The spontaneous emission is emitted in all directions and within the emission bandwidth of the ion. Therefore, the efficiency of coupling of spontaneous emission $\eta_{\omega,\mathrm{SE}}(\mathbf{r}_\perp)$ is introduced. The intensity is split into the monochromatic components and the sum over all frequencies is the total intensity $I = \sum_\omega I_\omega$.

The rate equation of $N_2(\mathbf{r},t)$ is given by

$$\frac{\partial N_2}{\partial t} = \sum_\omega \frac{I_\omega}{\hbar\omega}(\sigma_{a\omega}N_1 - \sigma_{e\omega}N_2) - \frac{N_2}{\tau_2}. \tag{3.2}$$

This rate equation is suitable for Yb-doped fiber, but if Er or Tm are simulated, more energy levels and their coupling coefficients must be included [163].

The propagation equation of the optical power is derived by considering energy conservation of the electromagnetic energy density given by I/v_g in the segment Δz, where v_g is the group velocity. The rate of change of the energy density equals the inward $I_\omega(z,t)$ and outward $I_\omega(z+\Delta z,t)$ propagating intensities and the intensity generated through stimulated emission $G(z)$, which equals the right hand side of Eq. (3.1) [154, 167]. The equation of continuity can thus be written

$$\frac{\partial}{\partial t}\left(I_\omega(z,t)\frac{\Delta z}{v_g}\right) = I_\omega(z,t) - I_\omega(z+\Delta z,t) + G(z)\Delta z, \tag{3.3}$$

Propagation in either direction of z can be accounted for by denoting the intensity variable I_ω^+ and I_ω^- for forward and backward traveling intensities, respectively. By assuming $v_g = c_0/n$ and taking the limit of $\Delta z \to 0$ leads to

$$\frac{n}{c_0}\frac{\partial I_\omega^\pm}{\partial t} \pm \frac{\partial I_\omega^\pm}{\partial z} = G(z). \tag{3.4}$$

The geometry of the optical fiber dictates translational symmetry, hence

$$I_\omega^\pm(\mathbf{r},t) = p_\omega^\pm(z,t)\Psi_\omega(\mathbf{r}_\perp), \tag{3.5}$$

where the optical power $p_\omega^\pm(z,t) = |\tilde{A}(z,t)|^2$ and transverse mode profile $\Psi_\omega(\mathbf{r}_\perp) = \psi^2(\mathbf{r}_\perp,\omega)$ according to the definitions in section 2.3.1. The power corresponds to the spectral power located within the interval $[\lambda - \Delta\lambda/2; \lambda + \Delta\lambda/2]$. Cylindrical coordinates are used so that

$$\mathbf{r} = \{r,\theta,z\}, \qquad \mathbf{r}_\perp = \{r,\theta\}, \qquad dS = rdrd\theta \tag{3.6}$$

It is assumed that the total number density of atoms are $N_0(\mathbf{r},t) = N_2 + N_1$. The fraction of the ions in the upper state is defined

$$n_2(\mathbf{r},t) = N_2(\mathbf{r},t)/N_0(\mathbf{r}), \tag{3.7}$$

and n_1 can be similarly defined, hence it follows that $n_2 + n_1 = 1$. The lower lasing level $n_1 = 1 - n_2$ is a dependent variable and is not necessary to model.

By combining Eqs. (3.1), (3.2), (3.4), (3.5), and (3.7) and integrating over the transverse plan, the final rate equation of population inversion can be put forward

$$\frac{\partial n_2(r)}{\partial t} = -\frac{n_2}{\tau_2} + \sum_\omega [\sigma_{a\omega} - (\sigma_{a\omega} + \sigma_{e\omega})n_2]\Psi_\omega(r)\frac{(p_\omega^+ + p_\omega^-)}{\hbar\omega} \tag{3.8}$$

together with the propagation equation

$$\begin{aligned} \frac{n}{c}\frac{\partial p_\omega^\pm}{\partial t} \pm \frac{\partial p_\omega^\pm}{\partial z} &= p_\omega^\pm \iint N_0\Psi[(\sigma_{a\omega} + \sigma_{e\omega})n_2 - \sigma_{a\omega}]dS \\ &\quad -\alpha_\omega p_\omega^\pm + \frac{\hbar\omega}{\tau_2}\iint \eta_{\omega,SE}N_0 n_2 dS. \end{aligned} \tag{3.9}$$

In the next section the spontaneous emission fraction $\eta_{\omega,SE}$ is discussed and illustrative examples are presented. The implementation is described shortly in Appendix C.

3.4.1 The spontaneous emission

In GS the pulse grows from spontaneous emission and it is therefore of crucial importance to include this contribution. There is no agreement on how to treat this term and several semi-classical models can be found in the literature [120, 151, 157–159, 162, 168–171]. The idea is to describe the probability that a spontaneously emitted photon is within the bandwidth of the optical resonator and within the supported NA of the fiber core. The contributions to the probability are therefore the spatial fraction $\eta_{\omega,SE}^{\text{spatial}}$ and the spectral fraction $\eta_{\omega,SE}^{\text{spectral}}$. Often the number of supported modes m are included, and it holds that $m = 2$

for a single mode core with two polarization states (modes). The total efficiency can therefore be written as

$$\eta_{\omega,SE}(\mathbf{r}_\perp) = m \cdot \eta_{\omega,SE}^{\text{spatial}} \cdot \eta_{\omega,SE}^{\text{spectral}} \tag{3.10}$$

One approach to find the description of the spatial contribution relies on solving the overlap of far-fields of a radiating dipole (the ion) and the transverse mode. It is written as [157]

$$\eta_{\omega,SE}^{\text{spatial,1}} = \frac{1}{2} \frac{|\iint \Phi_D \Phi_M dS|^2}{\iint |\Phi_D|^2 dS \iint |\Phi_M|^2 dS}, \tag{3.11}$$

where Φ_D is the far-field of the emitting dipole and Φ_M is the far-field of the transverse mode in the fiber. The solution in the limit of small angles (NA $<$0.2, $V >$1) is [157, 159, 172]

$$\eta_{\omega,SE}^{\text{spatial,1}} = \frac{\lambda^2}{4\pi n^2} \Psi_\omega. \tag{3.12}$$

An alternative method is a geometric approach, where the solid angle spread by the NA of the fiber $\pi \text{NA}^2/n^2$ is compared to the solid angle of an emitting dipole of 4π, hence [159]

$$\eta_{\omega,SE}^{\text{spatial,2}} = \frac{\text{NA}^2}{4n^2}. \tag{3.13}$$

The spectral component depends on the fraction of light emitted within the relevant bandwidth $\Delta\lambda$ (or $\Delta\omega$) with respect to the total emission and is written as [157]

$$\eta_{\omega,SE}^{\text{spectral,1}} = \frac{\sigma_{e\omega} \Delta\omega}{\int \sigma_{e\omega} d\omega} = \frac{\sigma_e(\lambda) \Delta\lambda}{\int \sigma_e(\lambda) d\lambda}. \tag{3.14}$$

It is possible to combined of Eqs. (3.12) and (3.14) using a relation between the spontaneous emission and an approximation for the lifetime τ_2 and assuming uniform distribution of ions over the core region [151, 159, 162]

$$\eta_{\omega,SE}^{\text{spectral,2}} = \frac{\sigma_{e\omega} c_0 \tau_2 \Delta\lambda}{A\lambda^2} \left(\eta_{\omega,SE}^{\text{spatial,1}} \right)^{-1}. \tag{3.15}$$

The results [159] and [162] differ by a factor of n. Alternatively, a one-photon-per-mode approximation can be used, which is defined as [158, 169]

$$\eta_{\omega,SE}^{\text{spectral,3}} = \Delta\nu \tau_2 \sigma_{e\omega} \Psi = \frac{c_0 \tau_2 \sigma_{e\omega} \Psi \Delta\lambda}{\lambda^2}. \tag{3.16}$$

In the literature different combinations of the spectral and spatial components are used. For example in [158, 169] only the one-photon-per-mode is used and in [168] a fitting parameter is added to the model to obtain agreement with the experimental results. In [159] the spatial contributions $\eta_{\omega,SE}^{\text{spatial},1}$ and $\eta_{\omega,SE}^{\text{spatial},2}$ are compared and $m = 2$ is used, but to obtain agreement with the results another parameter (overlap Γ, see section 3.6) is fitted. Eq. (3.15) and $m = 2$ are used in [162] and is generalized in [151] to include the radial dependence. Recently, a simulation of GS is shown in [120, 160] where $\eta_{\omega,SE}$ presumably is fitted to experimental data.

It is interesting to illustrate the differences between the approaches for realistic parameters. The chosen parameters are: $\Delta\lambda$ =1 nm, λ=1064 nm, $n = 1.45$, NA=0.087, $V = 3$, $A = 36\pi\mu\text{m}^2$, $\tau_2 = 800\mu$s, $\sigma_{e\omega} = 2.5 \cdot 10^{-25}\text{m}^2$, and a step index profile is used; hence $\int N_0 \Psi dS = N_0\Gamma/A$ and $\Gamma = 0.93$. The spatial contributions are in this case: $\eta_{\omega,SE}^{\text{spatial},1} = 3.5 \cdot 10^{-4}$ and $\eta_{\omega,SE}^{\text{spatial},2} = 9 \cdot 10^{-4}$, which is in fairly good agreement. The spectral contribution are $\eta_{\omega,SE}^{\text{spectral},1} = 3.3 \cdot 10^{-3}$, $\eta_{\omega,SE}^{\text{spectral},2} = 1.3 \cdot 10^{-3}$, and $\eta_{\omega,SE}^{\text{spectral},3} = 4.4 \cdot 10^{-7}$. The first two are also in good agreement with one another, whereas they both differ from the last approximation by almost four orders of magnitude. The last is used in time-independent simulations of amplification of spontaneous emission (ASE), which might be the reason for its validity and why it can applied effectively. For this reason the one-photon-per-mode approach will not be used here. As the different approaches yield similar results, it has been decided that Eq. (3.15) will be used as formulated in [151] in its implementation in this thesis.

3.5 Simulation results

In this section the detailed model is used to visualize the GS process and put forward some general trends. The results from simulations will also be compared to selected experiments to determine the degree of correspondence.

A set of standard parameters are used, unless otherwise stated in the caption of the figures. The parameters are close to one of the laser configurations examined in the experiments (laser configuration C as described in section 4.1). The parameters are: $P_{\text{pump}} = 75$ W, $L_{\text{Yb}} = 7$ m, $L_{\text{pas}} = 1$ m, $R_{\text{LR}} = 15\%$, $R_{\text{HR}} = 100\%$, $\Delta\lambda_e = 1$ nm, NA=0.087, $\lambda_{\text{pump}} = 915$ nm, and $\lambda_{\text{e}} = 1064$ nm, $2a = 12.5\mu$m, $D_{\text{clad}} = 125\mu$m, and $N_0 = 6 \cdot 10^{25}\text{m}^{-3}$. For simplicity no ASE wavelengths are simulated

unless otherwise stated, hence only the pump and signal are propagated.

The numerical parameters are chosen through a compromise between accuracy and computational time, thus $Q = 0.8$, $N_z = 75$, $dt = 0.45$ ns, $h = 0.11$ m, and $N_r = 10$. The simulation time of a single pulse train is between 1-10 minutes depending on the specifications of the PC and the numerical resolution.

In Fig. 3.3 the initial dynamics of GS can be seen. After 4-5 pulses the pulse train has stabilized so that the variation of peak power and pulse duration are less than 0.5%. The first pulse requires a longer pump pulse because transparency must first be created before the pulse can start to build up.

The impact of the pump power is shown in Fig. 3.4, where the pump power is varied from 15-150 W. The pulse duration is seen to decrease approximately as $t_0 \propto P_{\text{Pump}}^{-1/2}$ [51, 120]. The peak power increases almost linearly with the pump power with a slope around seven. Such fundamental analysis of GS is common to carry out to characterize the performance of the fiber laser. Examples of such analysis can be found in [114, 115, 120] and will also be shown in the chapter describing the experiments.

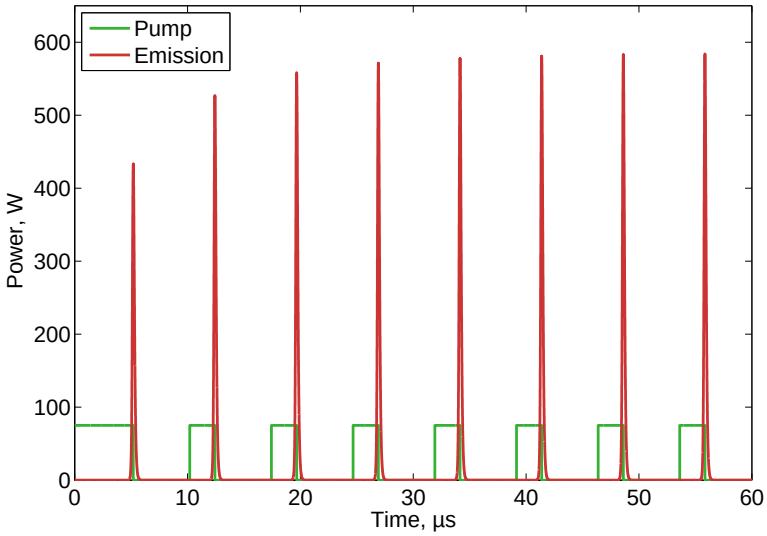

Figure 3.3: Instantaneous output power starting from the when the laser is shut off until the pulse train is stabilized.

Radial discretization is one of the strengths of the implementation developed in this project and the influence of non-homogeneous radial distribution of the excited state population will now be discussed. The

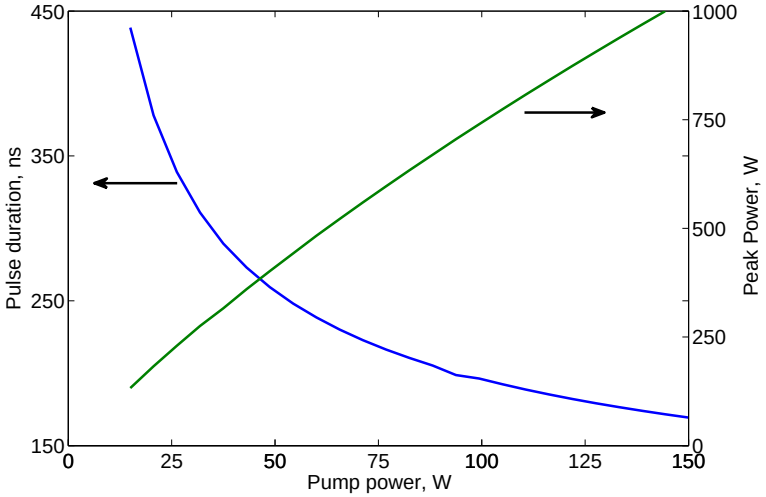

Figure 3.4: Influence of increasing pump power on the pulse duration and the peak power.

reason that the radial distribution of the excited population n_2 is non-homogenous is that the transverse mode in the core has a bell-like distribution. In general, this causes the population inversion in the center of the core to be depleted faster than the population inversion in the outer core. Before investigating the actual distribution it is relevant to evaluate the required number of radial points to obtain accurate results without unduly increasing the simulation time. Therefore, in Fig. 3.5 the influence of the number of radial point N_r on the peak power and the pulse duration is examined. It can be seen the peak power and pulse duration converge to a given value when the number of radial points is above about 20. At 10 radial points the error of both is below 2%, which in most cases is an acceptable error level, and therefore will this number of points be used in most of the following simulations. When only a few points are used the discrepancies become so large that the solution is invalid. For only a single radial point, which corresponds to the case of a homogeneous radial distribution, the pulse duration is only about 2% shorter than the converged solution and the peak power is 6% smaller. This deviation is rather small considering the large variation of actual n_2 population as will be discussed below.

In Fig. 3.6 the population of $n_2(r, z)$ is shown at the time for which the total population is at the highest i.e. right before the pulse is generated. In Fig. 3.7 $n_2(r, z)$ is shown at the time right before the *pump* is turned on, hence the population is at its lowest value. The difference

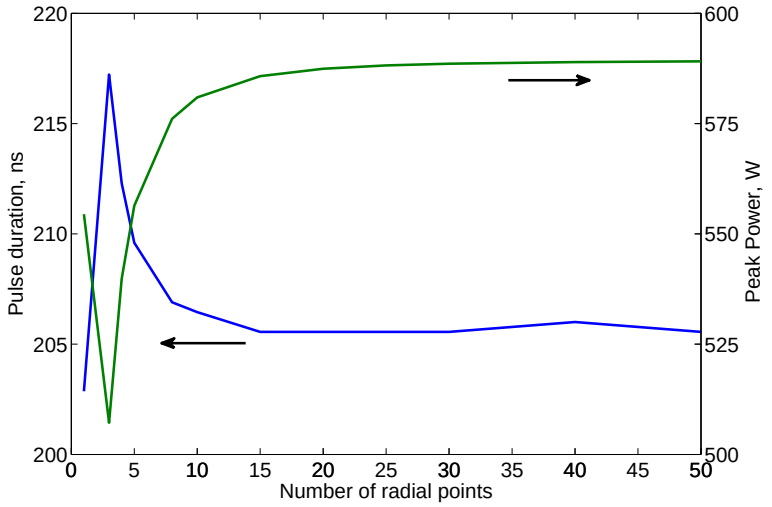

Figure 3.5: The pulse duration and peak power at increasing number of radial points.

between Figs. 3.6 and 3.7 corresponds to the extracted energy of the GS pulse. The minimum population is about ∼1% which corresponds to the transparency condition $n_2 = \sigma_{a\omega}/(\sigma_{a\omega} + \sigma_{e\omega})$. The maximum population is at the outer core close to the high reflector (small z). This region can not be completely depleted for several reasons: the overlap of the outer core and the transverse mode is small, the pump power is highest at this point, the area is largest in the outer core so a large fraction of pump power is absorbed, and the sum of the forward and backward propagating power is not sufficiently high to deplete the high population. In the case shown the maximum population is 13% before pulse generation, and after the pulse is generated the remaining maximum population is close to 10%. A high population of n_2 leads to a high amount of spontaneous emission. This means that the probability that the pulse is seeded by photons emitted from this region is high. Based on these results it is hard to argue that radial dependence can be neglected in accurate modeling of GS as done e.g. in [120, 160]. An extenuating circumstance might be that the fiber laser in [120] is backward pumped whereby the distribution of the forward and backward propagating powers is different.

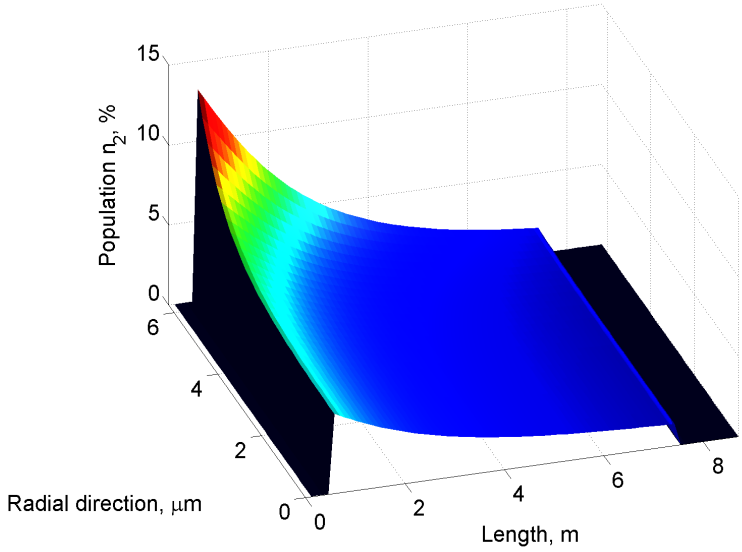

Figure 3.6: Population of the excited state n_2 before generation of the pulse. The number of radial point is $N_r = 30$.

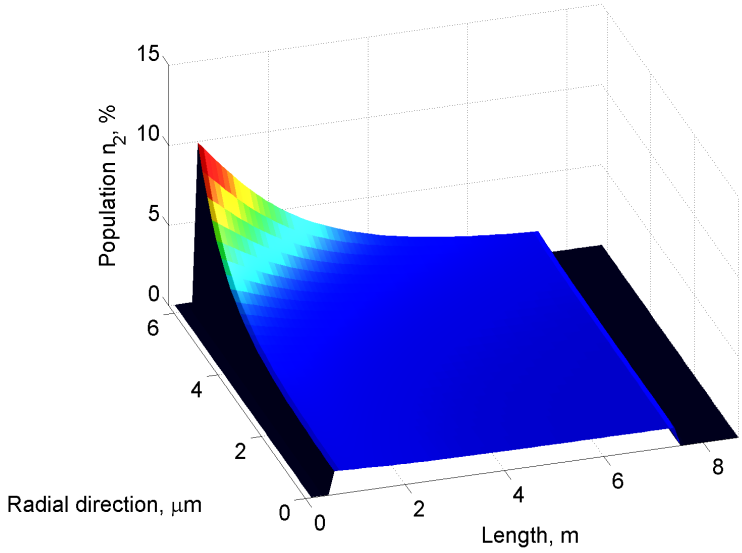

Figure 3.7: Population of the excited state n_2 long time after generation of the pulse. The number of radial point is $N_r = 30$.

It is also instructive to visualize the distribution of the optical power in the cavity during the generation of the pulse. This is illustrated in Figs. 3.8 and 3.9, where the forward and backward propagating power are shown, respectively. Note that the scales of the power axes are different in the two figures. It is seen that the pulse is generated homogeneously in the cavity as function of time. Backward propagating power is seeded by the reflected portion of the forward propagating light at the low reflector. It grows slowly until about 1-2 meters before the high reflector grating where it increases rapidly due to the high population inversion, as shown in Fig. 3.6. The boundary condition for the high reflector Eq. (C.3) applies, hence $p_\omega^+(L_{HR}) = R_{H,\omega} p_\omega^-(L_{HR})$. The forward propagating power increases mostly in the first half of the fiber length and reaches the maximum value right before the low reflector grating. From these figures it can be deduced that the GS process occurs with such a slow rate, compared to the propagation rate, that all points in the cavity at all times are in quasi-equilibrium.

The influence of the spontaneous emission and amplified spontaneous emission (ASE) in the early stage of the GS process will be addressed in the following. These effects are included in the model by simulating a number of wavelengths that do not have feedback by reflections. The wavelengths are spanning the most relevant emission wavelengths of the Yb ion between 1020-1130 nm. The number of discrete wavelengths is again a compromise between accuracy and computational speed. The number of wavelengths simulated was chosen to be 20, which corresponds to a bandwidth of $\Delta\lambda_{\mathrm{ASE}} = 5.5$ nm.

In Fig. 3.10 the instantaneous power in dBm is shown for the pump, the laser emission, and four selected ASE wavelengths. It can be seen that power at these wavelength is low and will not affect the optical-to-optical efficiency of the laser. However, it is interesting to see that the it takes about 500 ns before the power at the laser wavelength exceeds the ASE power level. This corresponds to more than six round trips in the cavity. During this time span the laser wavelength is competing against the ASE wavelengths over the gain. However, by comparing two identical simulations with either ASE included or no ASE wavelengths, it is found that the ASE wavelengths play no role in the output pulse characteristics. It is therefore a good approximation to neglect ASE wavelengths under typical conditions.

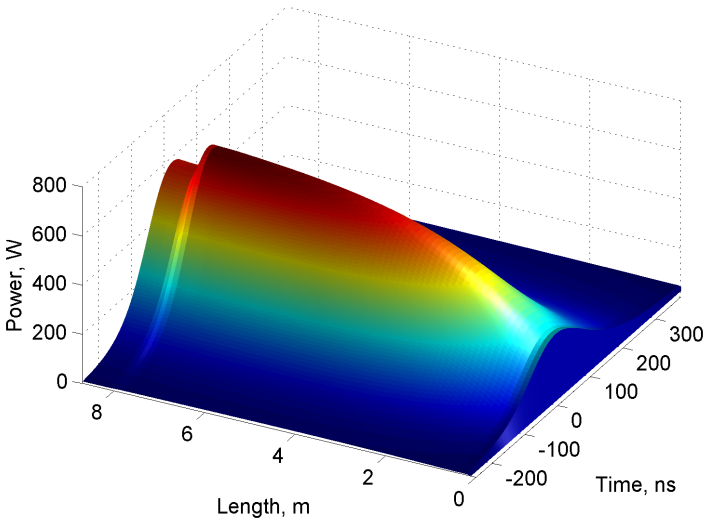

Figure 3.8: Forward propagating power in the cavity during pulse generation.

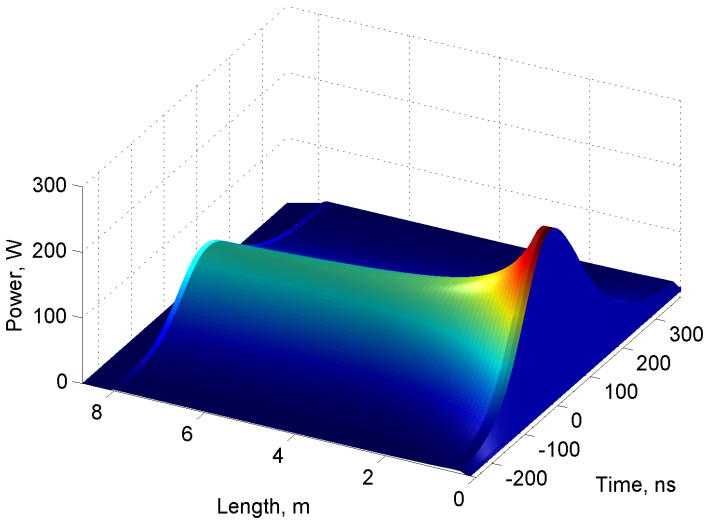

Figure 3.9: Backward propagating power in the cavity during pulse generation.

The power at the ASE wavelengths increases during the pump pulse but it is nothing compared to the power propagating at the laser wavelength. The dramatic amplification of more than 80 dB of the laser emission in the short time period of a few microseconds illustrates the extreme physics involved in GS. It can also be seen that after emission of the pulse the output power at the laser wavelength decays exponential (linearly on the dBm scale) at a rate given by the cavity decay time (see Appendix D). It takes almost 1.5 μs for the emission at 1064 nm to reach the ASE level around -30 dBm. This imposes an upper limit on a repetition rate for such a laser configuration.

It can be seen that the power level of the ASE wavelengths shown in Fig. 3.10 varies about 15 dB. To further investigate the variation with wavelength the time-averaged power spectral density at the ASE wavelengths are shown in Fig. 3.11. The maximum of the ASE is at 1072 nm, which is close to but slightly longer than the laser wavelength. This can be explained by the fact that ASE tends to have maximum at the lowest wavelength that fulfills the transparency condition, which is given by the remaining inversion level. The level of the power spectral density spans -50– -32 dBm/nm). For comparison the power spectral density is +45 dBm/nm during laser emission at 1064 nm.

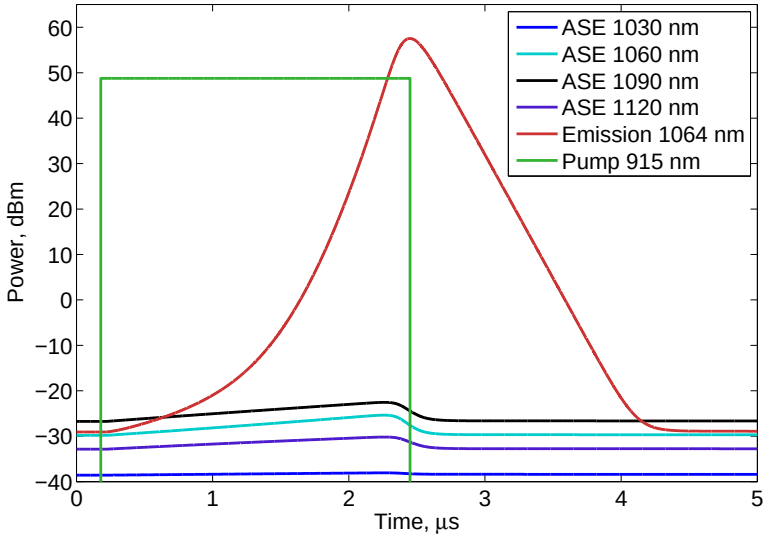

Figure 3.10: Instantaneous output power during a complete pump cycle. The pump at 915 nm and the emission at 1064 nm are shown together with ASE at four selected wavelengths. The number of simulated ASE wavelengths are 20, which corresponds to a bandwidth of 5.5 nm.

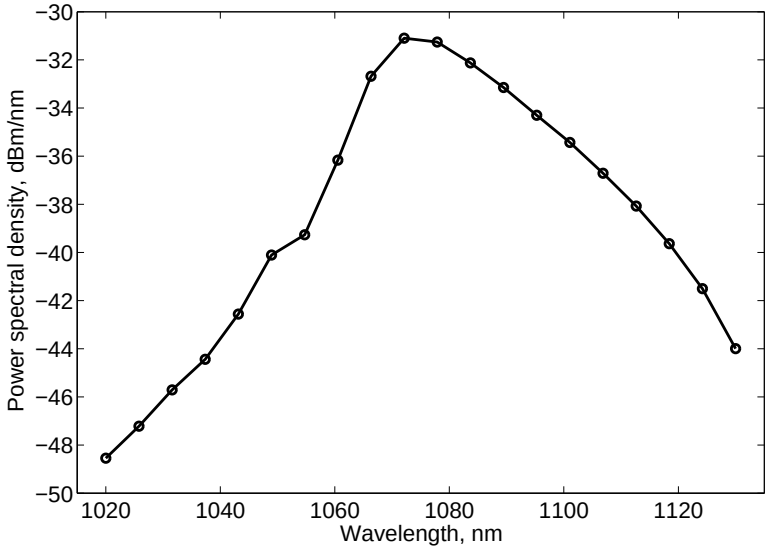

Figure 3.11: Time-averaged power spectral densities at the 30 simulated ASE wavelengths.

3.5.1 Optimizing input parameters

It is of interest to optimize the peak power and pulse duration for specific applications. By varying the fiber and resonator parameters in the model, the effect on the peak power and the pulse duration can be found. In the following, only the peak power is considered because it is the most important in SC generation. It is assumed that the model describes the physical system equally correctly for all inputs.

The number of radial points in these new simulations is set to 10 and no ASE wavelengths are considered. The standard parameters are: $P_{\text{pump}} = 75$ W, $L_{\text{Yb}} = 7$ m, $L_{\text{LR}} = 8$ m, $R_{\text{LR}} = 15\%$, $\Delta\lambda_e = 1$ nm, NA=0.08, $\lambda_{\text{pump}} = 915$ nm, and $\lambda_{\text{e}} = 1064$ nm. The peak power for the standard set of parameters is found to be 587 W . When the position of the low reflector L_{LR} is shorter than the active fiber length L_{Yb}, the rest of the active fiber is simulated as if it is spliced to the output of the low reflector grating.

The resulting relative improvements to the output peak power are listed in Table 3.1. In each line only the parameter to the left is changed and all other parameters are fixed. It can be seen that according to the model that it is favorable to have a long wavelength, narrow bandwidth, low reflection at the output, not too long or too short of a cavity length, and a low NA fiber core. When all these improvements are combined, i.e.

$L_{\mathrm{LR}} = 3$ m, $R_{\mathrm{LR}} = 5\%$, $\Delta\lambda_e = 0.01$ nm, NA=0.03, and $\lambda_{\mathrm{e}} = 1080$ nm, the peak power reaches 1090 W, which corresponds to an improvement of 85% more peak power compared to the standard configuration. The underlying reason for the improvement is related to reducing the coupling of spontaneous emission into the laser mode.

Here only a few selected parameters are optimized but one could also consider optimizing the doping density, the pump wavelength, the distribution profile of the ions in the core, core size, passive fiber length in the cavity, and if forward and backward pumping differs. It is unfortunately a humongous task to investigate the entire parameter space through simulations and even more time consuming to validate the results experimentally. For this reason a simplified model will be derived in the following section, which has the advantage that an analytic expression for the pulse duration can be derived. Furthermore, it turns out that this model is capable of describing the experimentally obtained pulse duration as will be discussed in section 4.3.

Parameter	Conf. 1 (diff.)	Conf. 2 (diff.)	Conf. 3 (diff.)
λ_{e}	1030 nm (-26%)	1050 nm (-8%)	1080 nm (8%)
$\Delta\lambda_{\mathrm{e}}$	10 nm (-11%)	0.1 nm (10%)	0.01 nm (20%)
R_{LR}	50% (-34%)	25% (-9%)	5% (6%)
L_{LR}	5 m (10%)	3 m (16%)	1 m (4%)
NA	0.14 (-12%)	0.05 (12%)	0.03 (29%)

Table 3.1: Relative improvement to the peak power via variation of the model input parameters relative to the standard parameters. Only the parameter listed to the left is changed in each line.

3.5.2 Comparison to experiment

The numerical model has now been used to reveal physical insight into the process of GS and some general trends have been discussed. It is also of interest to compare the numerical results with the experimentally obtained results to evaluate the accuracy of the model, which is the topic of this section.

The details of the experiments will be given in section 4 and for now only the temporal profile of a pulse will be used. The parameters used in the modeling are designed to be as similar to the experimental parameters as possible.

In Fig. 3.12 temporal pulses are shown, which are obtained in both experiments and through simulations. It can be seen that the peak power found in the experiment of ∼640 W is in reasonably agreement with the

peak power obtained in the simulation of 580 W for $m = 2$, which corresponds to single-mode operation. The pulse duration (FWHM) in the simulation is 210 ns and in the experiment it is 153 ns, so when it comes to the pulse duration the agreement is not satisfactory.

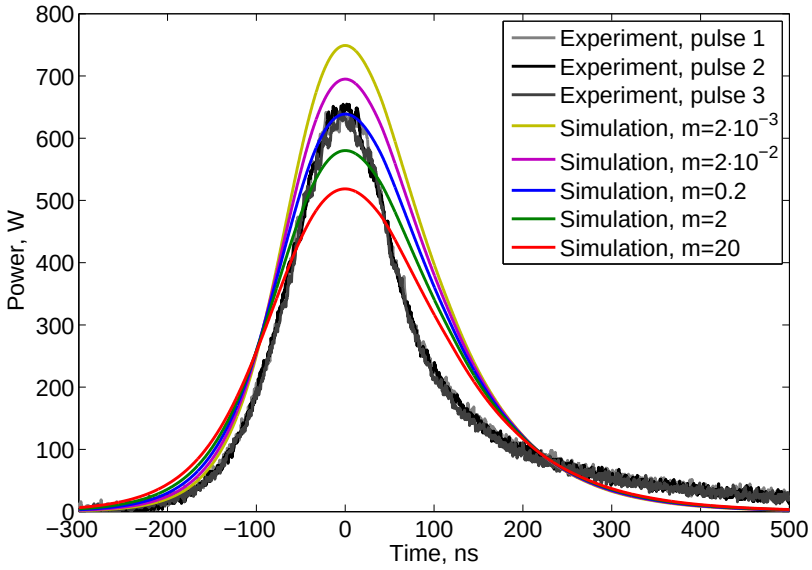

Figure 3.12: Experimental pulse profiles at a pump power of 75 W and 7 m active fiber using laser configuration C (section 4.1). Simulated pulse profiles are also shown for which the coupling strength of the spontaneous emission into the laser mode m is varied. The number of radial points is 15 and ASE wavelengths are neglected.

The fiber used in the experiment discussed here supports up to 6 modes (V=3.2), which means that the core can guide more of the spontaneously emitted light. The coupling of the spontaneous emission to the laser mode is controlled by the m-parameter (among others); therefore, a series of simulations with varying m-parameter are also shown in Fig. 3.12. It can be seen that peak power of the pulse is reduced with increasing m and vice versa. It is found that in order to fit the peak power the level of the experiment of 640 W an m of 0.2 is needed. However, at this value of m the pulse duration is 200 ns. At even lower value of m the pulse duration can be seen to decrease and at $m = 2{\cdot}10^{-3}$ it is 185 ns, which is closer to the experimental value.

Different configurations and pump power levels have been simulated and similar discrepancies to the experiments are generally found. For example, for a Yb-doped fiber length of 1 m the peak power and pulse duration obtained in the experiments are 270 W and 132 ns, respectively. The simulation results for this configuration yields a peak power

of 321 W and a pulse duration of 136 ns for $m = 2$, and to fit either the peak power or the pulse duration by the m-parameter results in reduction of the agreement to the experiment of the other output parameter.

At this point, it remains an open question what causes the deviation between experiments and simulations. The spontaneous emission power level in the experiment might be different than what the modeling predicts. The used spectroscopic data (cross sections) could also not be representative for the fiber in the experiment, even though it is provided by the fiber manufacture. The radial distribution the Yb ions are assumed homogeneous which might not be correct. Alternatively, pulse compression by nonlinear self-phase modulation, which are neglected here, could maybe explain the discrepancies.

In order to approach the experimental results one or more fitting parameters are required for now. This undermines the further evaluation using the model because these fitting parameters depend on unknown factors.

3.6 The point model

A simplified model will be derived, which has the advantage of being easier to solve than the detailed model in section 3.3. From this model, an analytic expression for the pulse duration can be derived, which is more practicable than a numerical model.

The population inversion and the photon density are assumed to be homogeneously distributed along the length of the cavity. Therefore, we can consider the simple rate-equations for a point model of a quasi four level laser medium ($\sigma_a \approx 0$) [99]. Thus, the population inversion density is $\Pi(t) = V^{-1} \int N_2(\mathbf{r}, t) d\mathbf{r}$ and the photon density in the cavity is $\phi = V^{-1} \int (p_\omega^+ + p_\omega^-) d\mathbf{r}$, where $V = \int_{\text{cav}} d\mathbf{r} = AL$ is the volume of the core, with A being the core area and L the cavity length. The ion density is described as $N_0(\mathbf{r}) = \hat{N}_0 \Phi(\mathbf{r}_\perp)$, where $\Phi(\mathbf{r}_\perp)$ is the transverse distribution function. The z dependence can be neglected and the rate equations are then reduced to [99]

$$\frac{d\Pi}{dt} = -\Gamma c \sigma_e \Pi(t) \phi(t) - n(t)/\tau_2 + p \tag{3.17}$$

$$\frac{d\phi}{dt} = \Gamma c \sigma_e \Pi(t) \phi(t) - \phi(t)/\tau_c + S - c\phi(t)\delta, \tag{3.18}$$

where $\Gamma = \int \Phi \Psi dS$ is the effective overlap of the optical mode and the doped area, $c = c_0/n$ the speed of light in the medium, σ_e the emission cross section at the emission wavelength, $p = P_{\text{abs}}/(V\hbar\omega_p)$ the absorbed

photon pump rate density, τ_c the cavity decay time defined in Appendix D, S the source of photons due to spontaneous emission, and δ the loss. In the following the fiber loss is small and therefore neglected.

The instantaneous output power is given by $P_{\text{out}}(t) = \hbar\omega_e V\phi(t)/\tau_c$. The rate equation in Eqs. (3.17) and (3.18) can easily be solved numerically e.g. using a time-step integration method. An example of a solution is shown in Figs. 3.1(a) and 3.2, where both GS operation and relaxation oscillations are shown.

The simplified and the detailed models have been compared and similar results can be obtained. In the simplified model the description of the coupling of the spontaneous emission to the laser mode determines the output pulse characteristics – as was the case with the detailed model.

The coupled equations are nonlinear and cannot be solved analytically, however an approximate analytic solution can be obtained by a linear stability analysis around a well-defined state. It is advantageous to use the steady state (CW) solution, where the population inversion density and the photon density are given by $\Pi_s = p_s\tau_2$ and $\phi_s = \tau_c(p - p_s)$, respectively, and the threshold power is defined as $p_s = (\Gamma c\sigma_e\tau_c\tau_2)^{-1}$.

Eqs. (3.17) and (3.18) are now linearized around the steady-state solution. We define $\Pi_1(t) = \Pi(t) - \Pi_s$ and $\phi_1(t) = \phi(t) - \phi_s$. The product of $n_1\phi_1$ is at first assumed to be small and this crucial approximation will be validated later. After some algebra the problem is reduced to a second order linear differential equation [99]

$$\frac{d^2\phi_1}{dt^2} + (\Gamma c\sigma_e\phi_s + \tau_2^{-1})\frac{d\phi_1}{dt} + (\Gamma c\sigma_e)^2\Pi_s\phi_s\phi_1 = 0. \tag{3.19}$$

This is of the form of a damped harmonic oscillator, which has the well-known underdamped, overdamped, and critically damped solutions. As τ_2 is much longer (hundreds of microseconds) than τ_c (nanoseconds) for rare earth doped glasses, it can be shown that the equation is dominated by the last term. The solution is therefore of the underdamped type [99]. From the solution to Eq. (3.19) we find the period of the relaxation oscillations, which is given by [51]

$$\tau_R = 2\pi\sqrt{\tau_2\tau_c}(p/p_s - 1)^{-1/2} \approx 2\pi\left(\frac{n_{SiO_2}AL}{c_0\Gamma\sigma_e}\frac{h\nu_p}{P_{\text{abs}}}\right)^{1/2}, \tag{3.20}$$

when it is assumed that the laser is driven well above threshold: $p/p_s \gg 1$. The absorbed pump power is related to the active fiber length by $P_{\text{abs}} = pV\hbar\omega_p = P_{\text{pump}}(1 - exp\{-0.23\alpha_{dB}L_{Yb}\})$, where α_{dB} is the pump absorption coefficient and P_{pump} is the incident pump power. The total cavity length is the sum of the passive and the active fiber length

$L = L_{\text{pas}} + L_{Yb}$. If the laser is not well above threshold, as for example in the case of three level lasers such as Tm-doped fiber lasers, the full expression in Eq. (3.20) must be used.

At first glance it might seem unreasonable to use the linear stability analysis of the rate equations to describe the GS process, which is not a small perturbation to a steady state. However, in the GS process the population inversion oscillates out of phase with the photon density, which can be interpreted from Fig. 3.2. Here it can be seen that when the population inversion is high the photon density is small and vice versa. In the derivation of Eq. (3.20) $\Pi_1\phi_1$ is neglected from the sum $(\Pi_s\phi_1 + \Pi_1\phi_s + \Pi_1\phi_1)$, hence the error of the approximation ξ can be evaluated numerically by

$$\xi(t) = \frac{\Pi_1\phi_1}{|\Pi_s\phi_1| + |\Pi_1\phi_s|}. \tag{3.21}$$

This error is shown in Fig. 3.13 for typical parameters used in this project. It is seen that ξ reached its maximum value of $\sim$0.6 at the front of the pulse and decays with the relaxation oscillations. Thus, the influence of the term is canceled out because $|\xi| < 1$ and the fact that it is oscillating rapidly compared to τ_R. The assumed product $\Pi_1\phi_1 = 0$ is therefore a fair approximation.

The relaxation oscillation period is central for GS because it dictates the time scale of the dynamics. In [51] the pulse duration t_0 of pulses produced by GS of an Nd-doped core-pumped fiber laser was found theoretically and experimentally to be related to T_R by

$$t_0 = \tau_R/\pi^2. \tag{3.22}$$

The derivation in [51] involves some questionable approximations, i.e. $t_{\text{on}} \approx 0.5\tau_R$; however as will be seen later, the pulse duration measured in the experiments match excellently with the pulse durations found using Eq. (3.22).

The pulse duration, therefore, has a square root dependence on the cavity length and the core area and an inverse square root dependence on the pump power. This is in contrast to Q-switching where the pulse duration depends on the mirror reflectivities and has a linear dependence on the cavity length [99].

3.7 Summary

In summary, the detailed model is an excellent tool for obtaining insight to the fundamental physics behind the GS process and general trends

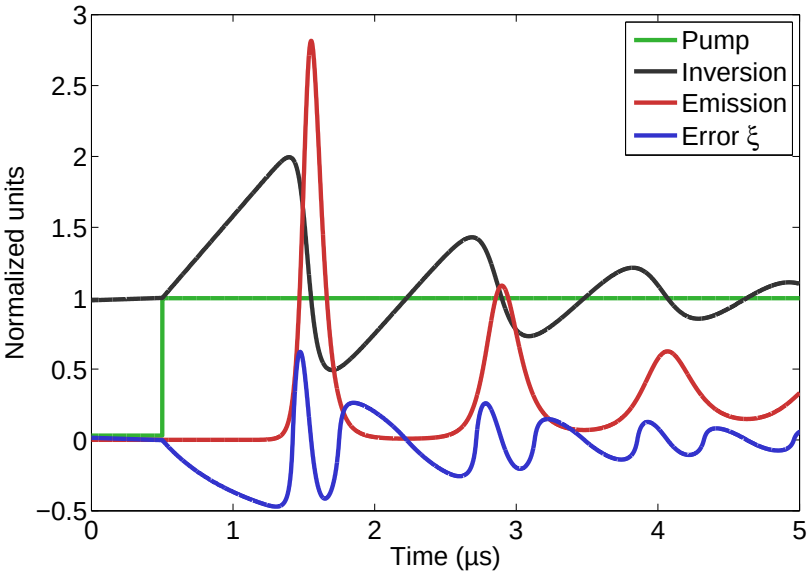

Figure 3.13: Simulated GS operation with evaluation of the linearization error ξ. The parameters are typical for GS cladding pumped Yb-doped FLs: 75 W pump at 915 nm, a 7 m cavity, and a core diameter 10 μm.

can be derived. The radial dependence is shown to be an important parameter when describing the non-homogeneous excited state population accurately. It is also concluded that the low power present at ASE wavelengths does not, under typical conditions, contribute significantly in the GS process. Alas, the model is computationally heavy and the agreement to experimental results is not sufficient.

A simplified model is derived and a linear stability analysis has been carried out, and validity of it is analyzed. The outcome is that the relaxation oscillation period can be found analytically, which is known to be related to the pulse duration of GS pulses. The simplified and the detailed models have been compared and similar results can be obtained. In the simplified model the description of the coupling of the spontaneous emission to the laser mode determines the output pulse characteristics – as was the case with the detailed model.

Chapter 4

Gain-switching experiments

In this chapter the GS experiments carried out in the course of the project will be presented. The experimental methods and configurations are described. The experiments are arranged so that one topic regarding a characteristic of GS is treated at a time. The experiments are therefore presented in a rather condensed form with focus on distinctive properties of GS. The discussed output parameters are the peak power, pulse duration, and spectral bandwidth. Both dynamics of GS at high and low repetition rates are investigated and discussed. Finally, the opportunities and limitations of GS of Yb-doped fiber lasers will be summarized. Some of the results presented here are published in [52, 173, 174].

4.1 Laser configurations and methods

The current fiber laser technology, common components, and methods by which to measure the output properties of fiber lasers are given in Appendix B. The addition of this appendix is intended to be an introduction to the terminology for the reader not familiar with fiber laser technology.

The typical experimental setup is illustrated in Fig. 4.1. During the course of this project several configurations of active fibers and fiber Bragg gratings (FBGs) have been built. In Table 4.1 the properties of the active fibers and FBGs used are summarized. The maximum available pump power and the maximum repetition rate by which they have been gain-switched are also listed. The typical slope efficiencies, the maximum obtained peak power, and minimum obtained pulse duration in GS operation are also summarized.

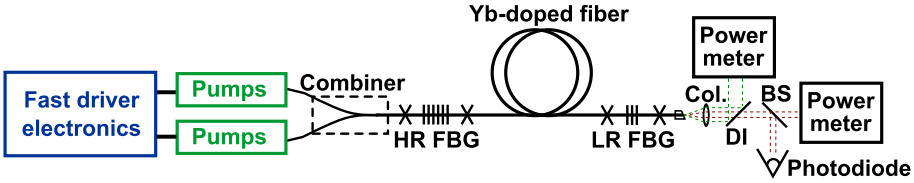

Figure 4.1: Experimental setup used in the project for GS in configuration A, B, and C. The differences between the configurations are listed in Table 4.1 The free-space components are collimator (Col.), dichroic mirror(DI), and beam sampler (BS).

The FBGs in configuration A are written directly into the core of the active fiber, which is Ge-codoped to assist with the grating writing process, and no passive fiber length is present in the cavity. In configuration B, C, and D the FBGs are written in the a Ge-doped fiber (TeraXion), that is subsequently spliced to the active fiber to form the cavity.

The power supplies of the pump lasers in configuration A and C are capable of operating at a high repetition rate, which corresponds to a high average output power of tens of Watts (IXYS Colorado formerly Directed Energy, or Messtec Power Converter GmbH). This is in contrast to configuration B and D, where the maximum limit on the repetition rate is about 8 kHz (Picolas GmbH) and the maximum average output power is a few Watts.

The wavelength of the pump diodes is around 915 nm (JDSU, Oclaro/-Bookham/Prophotonix, Jenoptik), and the maximum coupled pump power is varied between the configurations. In configuration C both pump diodes with wavelengths of 915 nm and 976 nm are used, and the maximum CW pump power is 75 W and 100 W, respectively. The pump diodes with wavelength of 976 nm are temperature controlled to stabilize the center wavelength.

4.1.1 Experimental method

All components of the fiber lasers are spliced and fulfill the requirement of being all-fiber lasers. The active fiber is coiled to a diameter for which the fundamental mode is primarily present. The splices are re-coated with a low refractive index polymer.

The output fiber is angle-cleaved and an anti-reflection-coated lens is used for collimation as can be seen in Fig. 4.1. In configuration B and C pump light is present at the output, which is separated by a dichroic mirror. The power of this residual pump light is measured by a

Configuration	A	B	C	D
Name of fiber	AeroLase	Liekki10	Liekki12	Liekki20
Mode field diameter (μm)	15	10	12.5	20
Core NA	0.073	0.08	0.087	0.07
Cladding diameter (μm)	250	125	125	125
Cladding NA	0.60	0.46	0.46	0.46
Cladding geometry	Air-clad	Round	Octagon	Octagon
Pump absorption (dB/m)	0.5	1.7	2.0	6.2
Polarization maintaining	No	Yes	No	No
MO length (m)	7	2.8	0.5-7	3.5
Passive length (m)	0	0.4	0.5-1.1	0.4
Gratings	In-fiber	Spliced	Spliced	Spliced
Low reflectivity (%)	15-20	13.7	14.7	11.9
Center wavelength (nm)	1064	1063.5	1064	1080
Bandwidth (nm)	<0.5	0.185	0.96	0.5
Combiner	61(10):1	7(2):1	7(7):1	†
Abs. slope efficiency (%)	75	36	83-90	75
Max. pump power (W)	105	230	75-100	1500
GS peak power (W)	730	700	900	9000
GS pulse width (ns)	210	66	80	40
Max. rep. rate (kHz)	500	8	1000	8

Table 4.1: Laser configurations used in the course of the project. The notation used for describing the combiner should be read as that in configuration A the combiner has 61 input ports, whereof 10 is used, and it has one output port. † Configuration D has both a forward combiner (7:1) and a backward combiner with signal feed-through (6+1:1) as can be seen in Fig. 4.12.

power sensor and meter. The light at the signal wavelength is incident on a beam sampler (wedge). The reflected light is diffused with a ceramic diffuser, and the temporal dynamics of the signal is detected by a photodiode (Thorlabs) whose output photocurrent is measured by an oscilloscope (Tektronix). The transmitted light is used to measure optical output power via a thermal power sensor and meter (Ophir 250 W). The measured output power is corrected for the power lost in reflection by the beam sampler.

The fiber laser is first characterized under CW pumping to extract the slope efficiency, the absorbed slope efficiency, and the optical-to-optical efficiency (see Appendix B.1). The ratio of signal power in the core and signal power in the cladding is measured by an adjustable iris. At high repetition rates the thermal load on especially the splices can be high, and their temperature is measured by a thermal camera. The

laser efficiency during GS is essentially the same as the CW efficiency.

In GS operation a given pump (peak) power and a duty-cycle are selected. The repetition rate is then increased or decreased until only a single spike is emitted, i.e. no subsequent relaxation oscillations are present. This condition is mostly met when the pump pulse is shut-off at the peak of the output GS pulse. Hysteresis effects can occur due to energy storage dynamics at high duty cycles (i.e. short time between the pump pulses), but can mostly be avoided by turning off the pump diodes before the repetition rate is changed.

In order to analyze the peak power and the pulse duration of the pulses, a Gaussian fit to the pulse temporal profile recorded with the oscilloscope is calculated as seen in Fig. 4.2. The peak power is then found as

$$P_{\text{peak}} = \frac{P_{\text{ave}}}{f \cdot t_0} = \frac{E}{t_0}, \tag{4.1}$$

where P_{ave} is the measured average output power of the fiber laser, f the repetition rate, $E = P_{\text{ave}} f^{-1}$ the pulse energy, and the pulse duration t_0 is determined as the FWHM of the Gaussian fit to the profile such as that shown in Fig. 4.2. The pulses do not have a perfect Gaussian shape but the method allows for an approximate and consistent determination of the peak power and the pulse duration. The residual power lying outside of the Gaussian fit has been evaluated and the fraction of the power outside the Gaussian function is typically 3% and at most 5%.

4.2 The peak power

The peak power of the pulses produced by GS is essential for the application of SC generation (see section 5), and is therefore investigated thoroughly. First, a simple examination of the peak power as function of pump power is given. Second, general dependencies are extracted by analyzing the peak power obtained in a variety of configurations.

The peak power (and the pulse duration) versus the available pump power is shown in Fig. 4.3. It is seen that the peak power varies linearly with pump power, and the slope has been evaluated at 6.6 W/W. By comparing the characteristics here to the simulation results in Fig. 3.4, the same trends are observed.

The linear behavior has also been found theoretically in [100] and it has been shown experimentally in recent publications for a fixed active and passive fiber length [114, 115, 120]. However, the effect of varying the cavity length on the peak power has not been explained in detail before and this aspect will be discussed in the following.

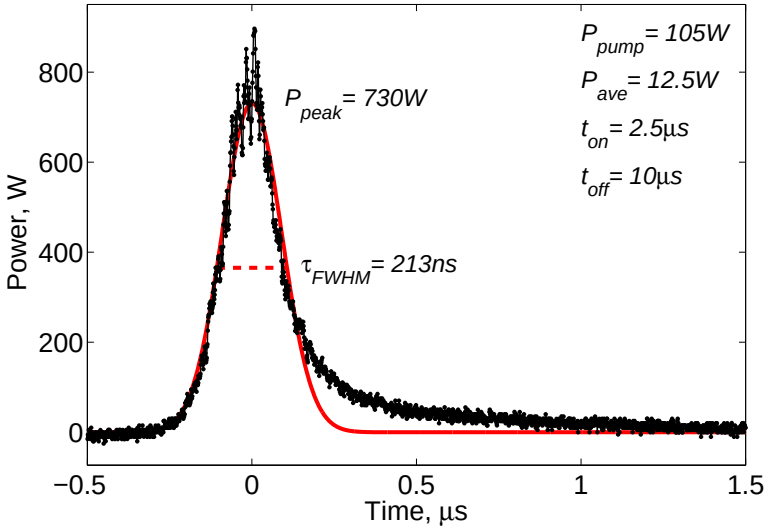

Figure 4.2: Determination of the peak power of a pulse via a Gaussian fit. The pulse shown here is obtained with the parameters given in the upper right. The peak power is estimated to be 730 W and the duration is 213 ns. This result is obtained using laser configuration A.

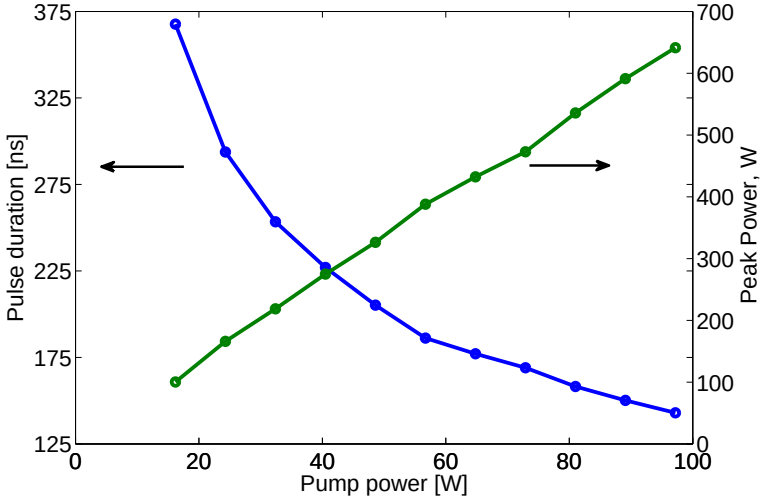

Figure 4.3: Pulse duration and peak power versus available pump power using laser configuration C with pumps at 915 nm and 5.5 m active fiber.

According to Eq. (4.1) the peak power is increased by reducing the pulse duration at a fixed pulse energy. The pulse duration is related to the length of the cavity as is described by the simplified model in Eq. (3.22) and in Appendix D. Thus, a hypothesis can be put forward that a shorter cavity length results in an increased peak power, which has been found to be the case in the Q-switching regime [99].

To investigate this hypothesis, laser configuration C is used and the active fiber length is reduced from 7 m to 0.5 m in steps of 0.5-1 m. The duty cycle is fixed at 20% and the average output power at the signal wavelength varies between 0.6-11 W due to a reduced pump absorption at shorter active fiber length. The resulting peak power of the pulses is shown in Fig. 4.4 for three pump power levels. It is seen that the peak power increases with pump power level (as seen in Fig. 4.3), and that for a fixed pump power level the peak power saturates as the active fiber length is increased. This saturation is related to the fact that for lengths longer than about 6 m, the pump absorption efficiency is >12 dB and increasing the length will only increase the absorption marginally. In [120] this saturation trend associated with active fiber length was shown numerically but three measurements showed a significant discrepancy. Here, the more comprehensive experiments for several pump power levels confirm the saturation. The outlined hypothesis can by this ground not be accepted.

The behavior seen in Fig. 4.4 gives a hint that the peak power is closely related to the absorbed pump power, which has a dependence on the active fiber length (L_{Yb}) that goes as

$$P_{\text{abs}} = \eta_{\text{abs}} P_{\text{pump}} = (1 - exp\{-0.23\alpha_{dB} L_{Yb}\}) P_{\text{pump}} \tag{4.2}$$

in the unsaturated case and for ideal pump distribution in the pump cladding. It is therefore proposed that peak power is linear with respect to absorbed pump power;

$$P_{\text{peak}} = \underline{\beta} P_{\text{abs}} = \underline{\beta} \eta_{\text{abs}} P_{\text{pump}}. \tag{4.3}$$

In Fig. 4.4 fits to the dependence of peak power on active fiber length obtained from combining Eqs. (4.2) and (4.3) are shown with dashed lines. The slope to the linear dependence $\underline{\beta}$ is found to be 9.1 W/W for all pump power levels. The good agreement here with peak power dependence on absorbed pump power allows us state that the slope $\underline{\beta}$ seems to be independent of the cavity length. To further test this generalization, the peak power is plotted against the absorbed pump power in Fig. 4.5, for several active fiber lengths (0.5-7 m), pump powers (25 W-105 W), pump wavelengths (915 nm and 976 nm), and active fibers (configurations A and C). A clear linear dependence can be seen.

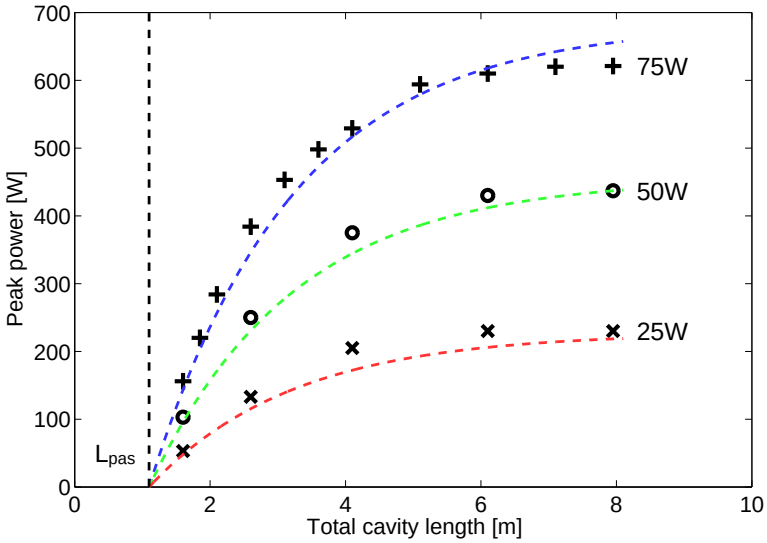

Figure 4.4: Peak power versus total cavity length for the result with 915 nm pumping using configuration C. The dashed lines are fits given by $P_{\text{peak}} = 9.1 P_{\text{pump}}(1 - exp\{-0.23\alpha_{dB} L_{Yb}\})$. The passive length ($L_{\text{pas}}$) of 1.1 m is indicated by the vertical dashed line.

Given the span of tested pump power levels, pump wavelengths, and cavity lengths, it is reasonable to believe that the slope is related to inherent properties of GS of Yb-doped fiber lasers. This is further supported by the fact that a slope of ∼9.3 W/W can be extracted from [120], where the cavity length is fixed at 2.12 m and pump wavelength is fixed at 976 nm. This result tells that the most important design parameter for the peak power is the absorbed pump power.

4.3 The pulse duration

In many applications the pulse duration is important and it is therefore investigated here. First, the pulse duration is examined with respect to increasing pump power in Fig. 4.3. The pulse duration is inversely proportional to the square root of the pump power as predicted by Eq. (3.22). By comparing the measured pulse duration to the simulation results in Fig. 3.4, it is seen that the same behavior is present.

To enable a thorough comparison of theory with experimental observations a wide range of pump power levels, pump wavelengths, and doped fiber lengths are examined. In Fig. 4.6 the resulting measured pulse durations are shown for laser configuration C with 915 nm pump

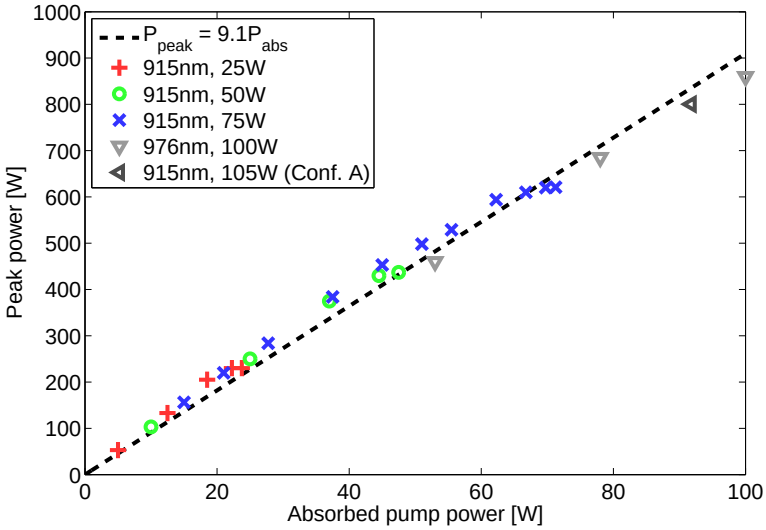

Figure 4.5: Peak power versus absorbed pump power for configuration C. The linear fit shows a slope of 9.1 W/W. The result at 915 nm and 105 W is from configuration A.

diodes with a pump power level of 25-75 W and for 976 nm pump diodes with a pump power level of 100 W. The cavity length is varied between 1.6 m and 8.1 m, which corresponds to 20%-95% absorption efficiency. The duty cycle is fixed at 20%, corresponding to repetition rates from 60 kHz to 500 kHz. A single result for configuration A and one obtained in [120] are also included. The pulse duration varies from 80 ns at the highest pump level to 260 ns at the lowest.

The dotted lines in Fig. 4.6 are found using Eq. (3.22) from the simplified model. The similarity between the model and the experimental results is striking. Considering the large parameter space spanned (cavity length, pump wavelength, pump power, core diameter, and doping level), the validity of Eq. (3.22) is confirmed. Such a thorough comparison between theory and experiments have not been described before [51,100]. The parameters, that determine the pulse duration, are therefore given explicitly in Eqs. (3.20) and (3.22).

In Fig. 4.6 a minimum of the pulse duration for a fixed pump power level can be seen at small cavity lengths of 2–3 m in the experimental data as well as in the analytical results. Note that the cavity length at the minimum is independent of the pump power level. This minimum can be explained by the presence of a certain length of passive fiber in the cavity of $L_{\mathrm{pas}} = 1.1$ m. It is expected that decreasing the passive fiber length reduces the pulse duration. By doing a thorough analysis

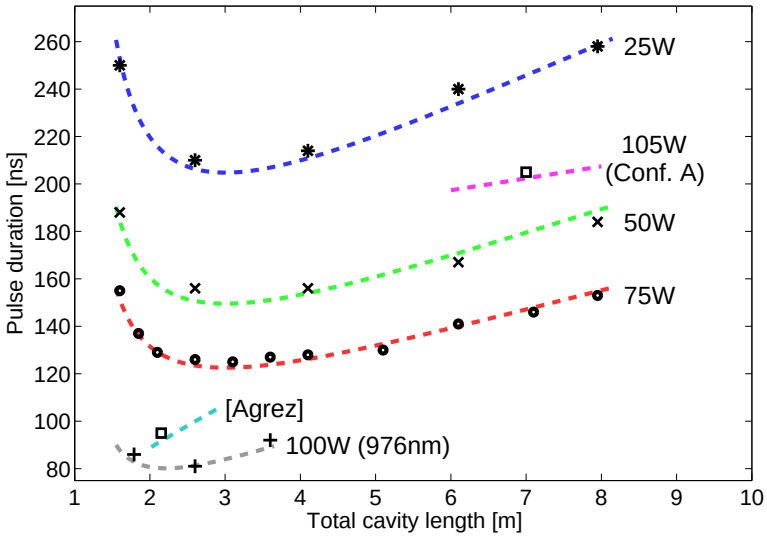

Figure 4.6: Pulse duration versus and total cavity length. Configuration C is used and the pump power at 915 nm is varied from 25 W–75 W and the pump power at 976 nm is fixed at 100 W. The pulse duration found in configuration A is also shown, by which only a single cavity length of 7 m is analyzed. The dotted lines are the results predicted by Eq. (3.22) with $\sigma_e = 2.5 \times 10^{-25}\mathrm{m}^2$, n_{SiO_2}=1.45, and Γ=0.93 (evaluated numerically). The black square adjacent to the bracket [Agrez] refer to results in [120] where the is pump at 976 nm and a different fiber is used.

it can be realized that the minimum pulse duration occurs at a shorter active fiber length, as the passive fiber length is reduced [52].

4.4 The repetition rate

At this point the discussed results have been obtained at a fixed duty cycle of 20% and the reason for this choice will become clear in this section. The influence of the repetition rate on the pulse characteristics will now be analyzed in the complete kilohertz range. In some situations it is of interest to increase the repetition rate to achieve the highest possible average output power. This also ensures the most efficient use of the available pump power. In other situations e.g. when the pulses are to be amplified in a fiber amplifier, a low repetition rate is desirable to obtain a high gain.

The GS properties of a fiber laser are characterized by a parameter space defined by pump power, pulse repetition rate f, and duty cycle D. In some situations it can be advantageous to state the repetition rate and the duty cycle in terms of the on-time $t_{\mathrm{on}} = D/f$, the off-time

$t_{\text{off}} = (1-D)/f$, or other combinations. Note that average output power scales (linearly) with duty cycle.

4.4.1 High repetition rate dynamics

The GS properties of the fiber laser in configuration A at high repetition rates (>50 kHz) will now be analyzed. The results obtained at the maximum pump power of 105 W are shown in Fig. 4.7. The pump power is fixed at 105 W to give the highest possible peak power. By increasing the duty cycle the average power is increased. Stable GS operation is obtained by selecting the first spike as described in section 4.1.1. The resulting t_{on} and t_{off} are shown in the lower section of Fig. 4.7. This kind of analysis has also been carried out using configuration C and similar trends are generally obtained. The shape of the curves in Fig. 4.7 will be described in the following and in the next section theoretical estimates of the on-time and off-time are given.

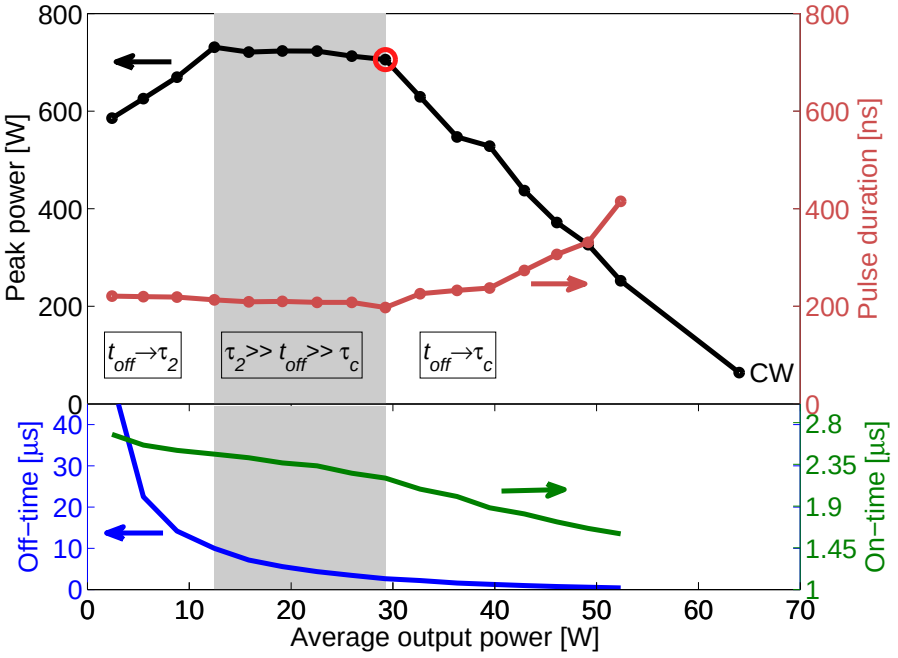

Figure 4.7: The GS power characteristics of the fiber laser with configuration A at maximum pump power of 105 W. The peak power and pulse duration of pulses are shown. The optimum regime regarding peak power is in-between the slow; $t_{\text{off}} \rightarrow \tau_2$ and the fast; $t_{\text{off}} \rightarrow \tau_c$ regimes. The off-time t_{off} and the pump pulse duration t_{on}, which is set equal to the build-up delay ($\tau_\delta = t_{on}$), are shown in the lower section.

At the lowest average output powers the pump pulses are separated

by long off-times. The limiting situation of this is given by a completely relaxed laser cavity pumped by a single pump pulse. Here the pump has to excite ions to reach threshold before lasing occurs. This costs pump energy, hence the peak power of the pulse is reduced. The characteristic time for a completely relaxed cavity is given by the upper state lifetime of the Yb ions τ_2, which is 800 μs depending, among other things, on the doping concentration [64]. By these arguments the region of reduced peak power at lowest average powers can be explained by too long of an off-time in which the system approaches the relaxed state; $t_{\text{off}} \to \tau_2$.

At the highest average output power the off-time is decreased to the same value as the on-time or less. If the off-time approaches the cavity decay time, the cavity still contains a large amount of photons at the beginning of a new pump cycle. Therefore, the initial conditions for the relaxation oscillations are different and it results in longer signal pulse durations. The regime can be described by $t_{\text{off}} \to \tau_c$, where the cavity decay time $\tau_c = 35$ ns is given by Eq. D.4. The underlying mechanism of this scenario can be visualized by looking at Fig. 3.10, where it is clear that in order for the photon level to reach the spontaneous emission level a certain off-time is needed, which in that case is about 1.5μs.

For SC generation a high peak power is required to obtain a broad bandwidth, and for a fixed peak power the highest average power is desired to get the highest power spectral density in the SC spectrum. Given the plateau of constant peak power observed in Fig. 4.7, the optimum point of operation is selected as the point marked by red in Fig. 4.7. Here, GS of the fiber laser can yield a train of pulses with more than 700 W peak power and a duration around of 200 ns when operated at 105 W of pump power and a repetition rate of 210 kHz with a duty-cycle of 45%, which corresponds to $t_{\text{on}} = 2.1$ μs and $t_{\text{off}} = 2.6$ μs. The resulting average power is 29 W and the pulse energy is 150 μJ. The generated pulse train has, to our knowledge, the highest pulse energy and average power levels published using a diode-pumped gain-switched fiber laser [108, 109, 118, 119].

It has been observed that for a variety of different laser cavities in configuration C, the lower limit of the plateau is at duty cycles lower than 20% . This justifies the use of a duty cycle of 20% in the investigation of the peak power and the pulse duration above.

4.4.2 On-time and off-time

In the lower section of Fig. 4.7 the variation of on-time t_{on} and off-time t_{off} are shown for a given experiment. They can be used to determine at which repetition rate efficient GS operation is achieved for a given pump

power through $f^{-1} = t_{\text{on}} + t_{\text{off}}$. It is desirable to be able to control the repetition rate, and therefore the dependencies of on-time and off-time will be examined.

The variation of the on-time as function of the pump power is shown in Fig. 4.8. It is shown together with the pulse duration to emphasize that they approximately have the same dependence. The on-time therefore also goes approximately as $P_{\text{pump}}^{-1/2}$. This dependence has also been discussed in [100, 120].

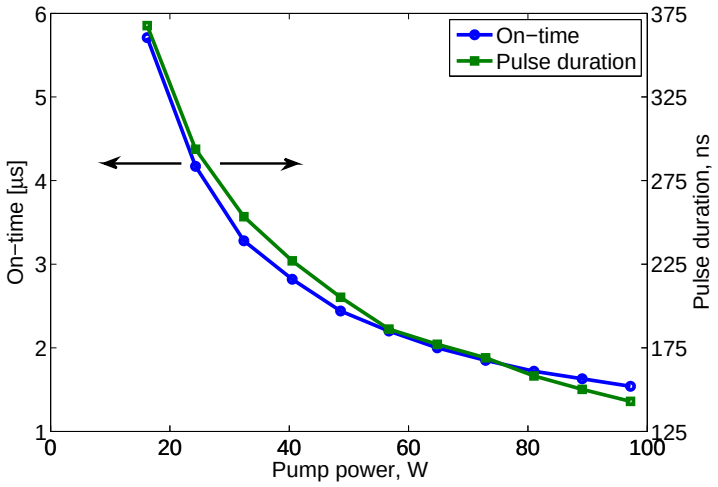

Figure 4.8: On-time as function of pump power using laser configuration C with pumps at 915 nm and 5.5 m active fiber.

The starting point for predicting the on-time is to consider that well above lasing threshold the output pulse energy E is related to absorbed pump pulse energy $E_{\text{pump}}^{\text{abs}}$ via the slope efficiency η_s, hence

$$E = P_{\text{peak}} t_0 \approx \eta_s E_{\text{pump}}^{\text{abs}} = \eta_s t_{\text{on}} P_{\text{abs}}. \tag{4.4}$$

The validity of this relation has been confirmed because the measured pulse energies are in excellent agreement with the values obtained using Eq. (4.4). By combining this relation with Eq. (4.3) it then follows that

$$t_{\text{on}} = \frac{\beta}{\eta_s} t_0. \tag{4.5}$$

In Fig. 4.9 the on-time is shown as function of the total cavity length. The results are obtained simultaneously with the results shown in Fig. 4.6. The lines in the plot are calculated using Eq. (4.5) with either the

measured pulse duration (dashed lines) or the pulse duration obtained by Eq. (3.22) (full lines). The agreement is fairly good with an error falling below 10%. The difference between the evaluations of Eq. (4.5) using the measured or calculated pulse duration is less than 5%.

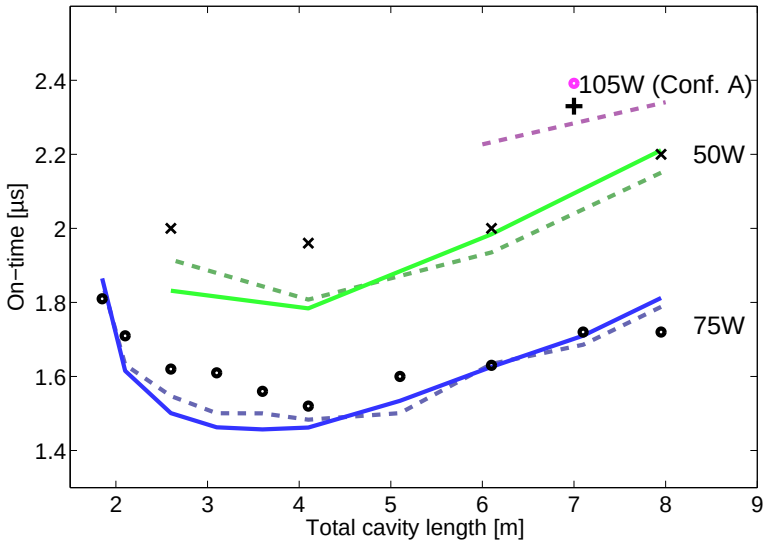

Figure 4.9: On-time at optimum duty cycle. The dots are measured values, the dashed lines are found by evaluating Eq. (4.5) using the measured pulse duration, and the full lines are found by evaluating Eq. (4.5) using the pulse duration calculated from Eq. (3.22). Configuration C is used and the pump power at 915 nm is varied from 50 W–75 W. A single data point measured using configuration A is also shown, and as only one cavity length is measured, Eq. (4.5) is only evaluated using the measured pulse duration at 7 m.

The shortest off-time for which the peak power remains at the high level as function of cavity length for three pump power levels is shown in Fig. 4.10. It therefore represents the optimum repetition rate, and it corresponds to the situation where the cavity is just emptied sufficiently. In Fig. 4.10 it can be seen that the off-time is decreased from more than 3 μs at 8 m cavity length to about 1.1 μs at 2 m cavity length at pump power levels of 50 W and 75 W. This means that a higher repetition rate is possible with the shortest cavities, which have the least pump absorption efficiency. Improvement of the maximum repetition rate for a short cavity compared to a long cavity is higher than 80% in the presented measurements. The minimal off-times are slightly smaller at a pump power level of 25 W so it is also dependent of the pump power level. The reason for this is not clear.

The off-time is an expression of how long it takes for the photon level

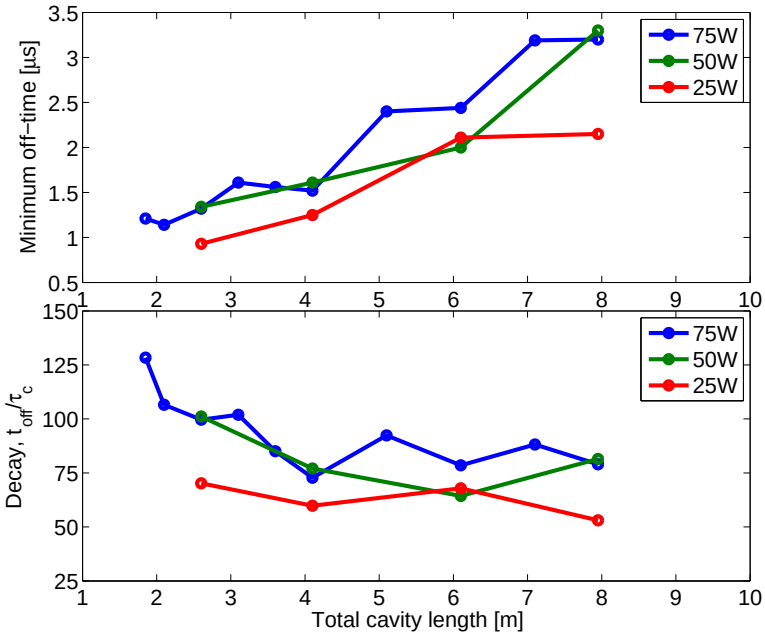

Figure 4.10: The minimum off-time, for which the peak power is maximized, is shown in the upper section. In the lower section the off-time is normalized to the cavity decay time. Configuration C with 915 nm pumps are used to obtain these results.

to reach the spontaneous emission level, and it is therefore relevant to normalize the off-time to the cavity decay time, which is given by Eq. (D.4). In Fig. 4.10 t_{off}/τ_c is shown as function of cavity length and pump power level. The variations that can be seen are probably due to varying loss in the splices. For a pump level of 75 W the off-time is between 75 to 125 times the cavity decay time and it decreases slightly with the pump power level.

The cavity decay time can be reduced by decreasing the reflectivity of the low reflector. This has been experimentally confirmed by using a flat end-facet with 4% reflection as the low reflector. The resulting maximum repetition rate is about 30% higher than for the grating with 15% reflection, which is in good agreement with the reduction in the cavity decay time.

4.4.3 Low repetition rate dynamics

In this section GS at low repetition rates of a few kilohertz is described, which corresponds to duty cycles less than 0.5%. In the discussion of

the low duty cycle limit of the results in Fig. 4.7, it is argued that the delay between the pump pulses are approaching the lifetime of the excited Yb ions ($t_{\text{off}} \sim \tau_2$). This causes a substantial amount of the residual inversion to decay between the pump pulses as the population decays as $\exp\{-t/\tau_2\}$. To put this into numbers, this means that at a repetition rate of 1.8 kHz, roughly 50% of the residual ions have decayed to a lower energy state between the pump pulses. This is contrary to a high repetition rate of 50 kHz, where only less than 5% of the stored residual energy is lost by this process. Therefore, the level of excited ions is highly dependent on the repetition rate.

This has the effect that if the repetition rate is low then a low population inversion is present at the time of spike emission, which leads to output pulses with low pulse energy, low peak power, and a long pulse duration. This effect can be seen in Figs. 4.11(a) and (d), where the repetition rate is decreased from 5 kHz to 1 kHz and from 8 kHz to 3 kHz, respectively. In Fig. 4.11(a) the temporal traces of the pump and the emitted spikes are shown for a fixed absorbed pump energy of 150 μJ. At the repetition rate of 5 kHz the output pulses have a duration of 66 ns, a peak power of 700 W, a pulse energy of 55.4 μJ, and the optical-to-optical efficiency is 36%. In Fig. 4.11(d) the absorbed pump energy is reduced to 77 μJ, which results in an output pulse with a duration of 130 ns, a peak power of 150 W, a pulse energy of 22.4 μJ, and the optical-to-optical efficiency is 30% at 8 kHz. At a repetition rate of 4 kHz the efficiency is half of this value due to the relaxation of excited Yb ions.

In Fig. 4.11(a) the emitted pulse at the repetition rate of 1 kHz has a low peak power, which means that the lasing threshold is just exceeded. The threshold absorbed pump pulse energy $E^{\text{abs}}_{\text{pump,th}}$ is a function of the repetition rate and it can be estimated by

$$E^{\text{abs}}_{\text{pump,th}} = \frac{P_{th}}{f(1-\exp\{-(f\tau_2)^{-1}\})}, \tag{4.6}$$

where P_{th} is the threshold pump power in CW operation. In Fig. 4.11(d) the absorbed pump pulse energy is 77 μJ and it can be estimated that at 2 kHz the threshold is barely reached, which result in a threshold pump power of ~70 mW. For example, if a repetition rate of 0.5 kHz is desired the threshold pump pulse energy exceeds 150 μJ.

In Fig. 4.11(a) and (d) it can be seen that the pump power level is fixed but the peak power level is increasing (with repetition rate). This is contrary to the results in section 4.2, where it is shown that the peak power scales linear with pump power. The reason that this relationship

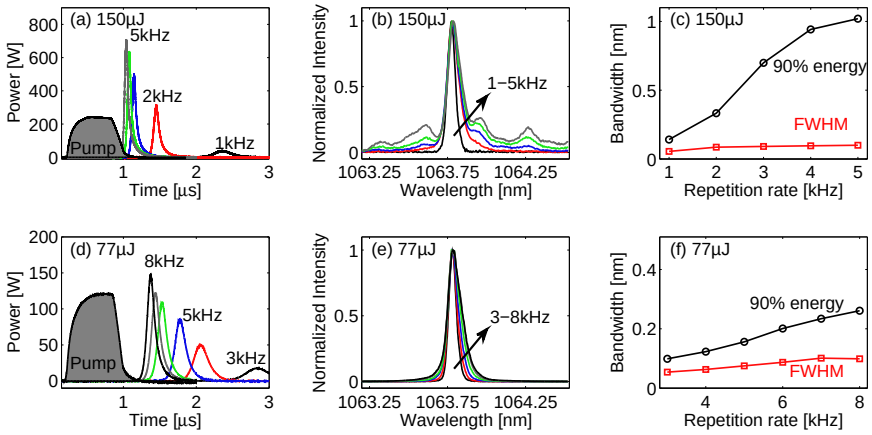

Figure 4.11: Characterization of the output of the MO at increasing repetition rate and absorbed pump energies. Temporal pulse shapes are shown in (a) and (d) for 150 μJ and 77 μJ absorbed pump energies, respectively. The spectra are given in (b) and (e). Calculated FWHM and 90%-confined-energy bandwidths are shown at increasing repetition rate in (c) and (f). The laser configuration B is used.

fails is that at low repetition rates the laser is not operating well above the threshold, which is a requirement for the linearity.

An experiment has been carried out to examine the power scalability in the low repetition rate regime. The laser configuration D has been used as shown in Fig. 4.12, where the number of pump powers are increased to seven. In Fig. 4.13 the pump power level is increased to 1500 W, which is realized by applying both forward and backward pumping and increasing the pump diode current well above the specified value. It can be seen that the peak power of the pulse exceeds 8.9 kW and the pulse duration is as low as 41 ns at a repetition rate of 6 kHz. Both these numbers are the current records for GS of Yb-doped fiber lasers. In the right of Fig. 4.13 the repetition rate is varied and it can be seen that approximately the same peak power can also be achieved at 3.8 kHz. This experiment demonstrates that GS of Yb-doped fiber lasers can be scaled efficiently. Here, the scaling was limited by the pulsed diode drivers.

4.5 The spectral bandwidth

The spectral bandwidth of the output pulses are mainly of concern in nonlinear applications due to e.g. narrow bandwidth phase-matching conditions [174]. The spectral bandwidth of the output pulses is in

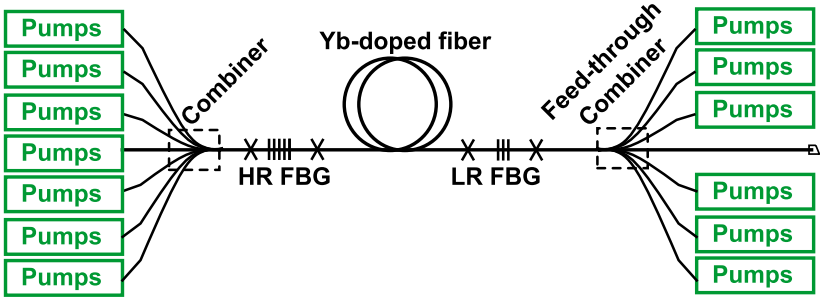

Figure 4.12: Experimental setup used in configuration D for power scaling.

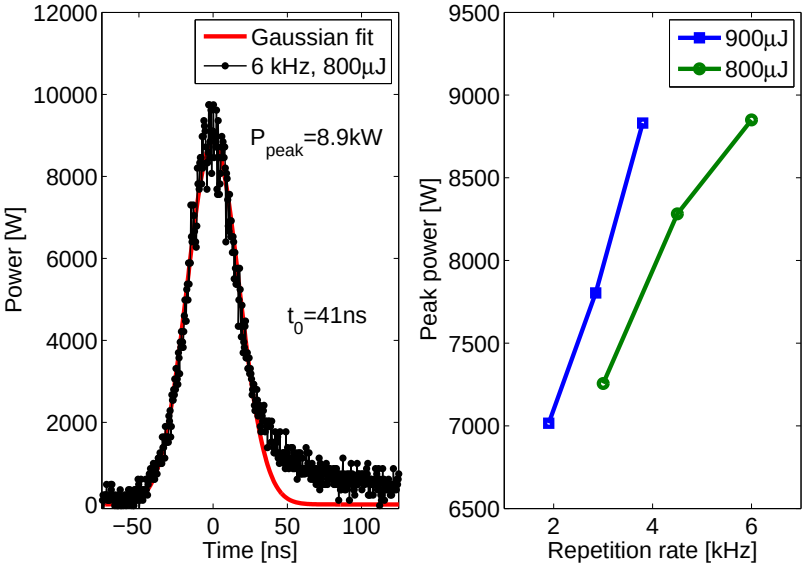

Figure 4.13: Gaussian fit and temporal pulse profile recorded at 6 kHz and a pump energy of 800μJ. To the right the peak power versus repetition rate is shown for two pump pulse energies. The laser configuration D is used.

general determined by the bandwidth of the low reflecting grating, which in most cases is narrower than the high reflection grating.

It is known that the spectral bandwidth of fiber lasers are broadened by self-phase modulation (SPM) even at a relative low power level of a few Watts and that it in many cases achieves a Lorentzian-like spectral shape [175, 176]. In Fig. 4.14 the spectra of the outputs are shown at increasing peak power using configuration C, i.e. it is in the high repetition rate regime. It is clear that the pulses broaden with peak power and the triangular shape on a logarithmic scale resembles the typical Lorentzian spectrum, which indicates that SPM is responsible for the broadening. The FWHM bandwidth increases from 0.26 nm at a CW output power of 42 W to 0.6 nm at a peak power of 600 W.

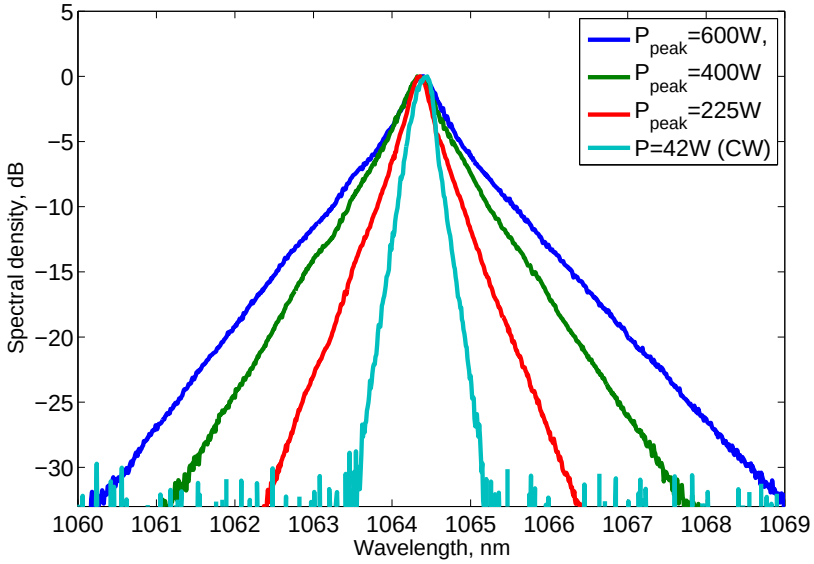

Figure 4.14: Normalized spectra at increasing peak power in the high repetition rate regime. Laser configuration C is used with pumps at 915 nm.

The spectral bandwidth has also been examined in the low repetition rate regime. The normalized spectra of the output pulses are shown in Fig. 4.11(b) for increasing repetition rate. At the lowest repetition rate of 1 kHz the spectrum has a narrow Gaussian-like shape. The spectra at higher repetition rates have, besides a narrow central peak, irregular and broad structures that contain a significant amount of the pulse energy.

The commonly used full-width half-maximum is not a good measure of the actual bandwidth of these spectra. Therefore the bandwidth that contains 90% of the pulse energy (B90) is evaluated in addition to the

FWHM. For a Gaussian spectral shape the B90 is 1.4 times the FWHM and for a Lorentzian shape the B90 is a factor of five of the FWHM. The ratio of the B90 and the FWHM can be seen as a measure of the quality of the spectrum.

In Fig. 4.11(c) on page 65 the FWHM and B90 bandwidths are shown for increasing repetition rate. At the lowest repetition rate of 1 kHz the spectrum has a narrow FWHM of 0.055 nm and a B90 of 0.14 nm. At the highest repetition rate of 5 kHz the FWHM increases slightly to 0.1 nm while the B90 reaches 1 nm. The highly irregular shape indicates that SPM cannot solely be responsible for this broadening. The reason for the irregular shape is that the gain becomes so high that lasing occurs at wavelengths, which are only slightly supported by the cavity. These wavelengths are most likely governed by the spectral side-lopes of the low reflector FBG. The reflection spectra of the low reflecfor FBG is shown in Fig. 4.15. The side-lopes specified by the manufacture to be 12 dB below the peak of the reflection of 13.7%.

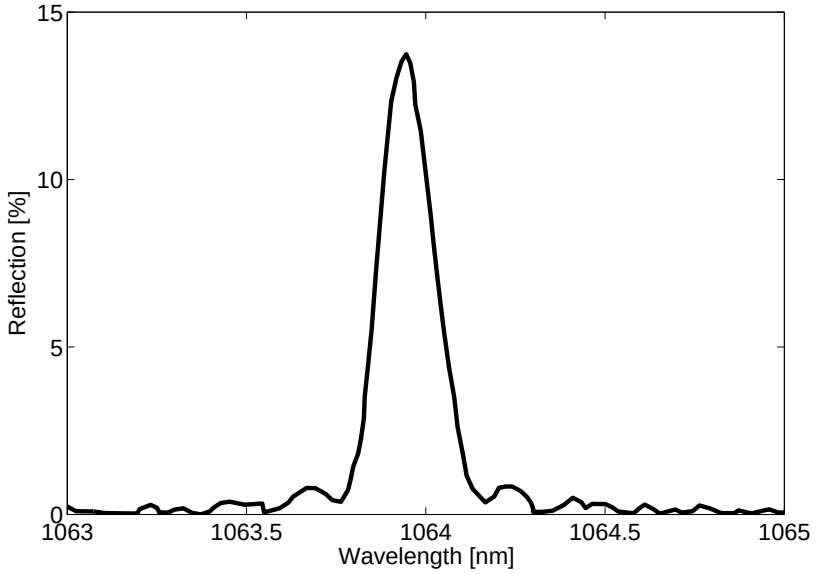

Figure 4.15: Reflection spectra of the FBG used in configuration C.

In Fig. 4.11(e) and (f) the normalized spectra and the bandwidth are shown for a reduced absorbed pump energy of 77 μJ. In contrast to pumping with a pulse energy of 150 μJ, the spectra obtained with 77 μJ of pulse energy remain well-behaved while increasing repetition rate, which also results in a smaller B90 of maximum 0.25 nm at 8 kHz.

It has been observed the polarization extinction ratio tends to de-

grade with reduction of the spectral quality. The polarization extinction ratio is typically 14 dB using laser configuration C.

4.6 Discussion

In the previous sections important aspects of GS have been investigated experimentally, and explicit expressions have been put forward regarding the design parameters in GS. These will now be applied to discuss the possibilities and limitations of GS of cladding-pumped Yb-doped fiber lasers.

The peak power is shown to depend linearly on absorbed pump power. The maximum achievable peak power for a given pump power can thus be achieved by absorbing the pump sufficiently (>16 dB). It further means that the cavity length has no influence as long as the pump absorption is maintained.

It is interesting to note that a typical length of passive fiber in the cavity thereby has a negligible influence on the peak power. This finding has furthermore been checked by reducing the passive length from 1.1 m to 0.5 m, and the peak power emitted had been found to be unchanged, which confirms this result. This conclusion only applies as long as nonlinear effects and losses can be neglected.

Given these results, a typical diode pump module with a power of 25 W can produce a pulse with a peak power of more than 200 W and an average output power of more than 10 W, when driven with a realistic duty cycle of 50%. Some applications require a higher peak power, e.g., in the tens of kilowatts regime, and in this case the pump power needs to be in the kilowatt range. This increases the complexity and the cost of the laser significantly. A more cost-effective solution would be to generate gain-switched pulses with a moderate pump power and then amplify them in a large mode area fiber amplifier.

Cladding pumping is advantageous in regards to power scaling because the generated heat is distributed over a long fiber length. A long cavity length, however, leads to a long duration of the pulses, and minimizing the pulse duration turns out to be rather challenging. The pulse duration scales as $P_{\mathrm{pump}}^{-1/2}$ and the scaling possibilities are typically limited by the available pump power. Controlling the pulse duration via the fiber laser design involves tuning the core area A, dopant density N_0, and cladding area A_{clad}. In this regard the pulse duration scales as

$$t_0^2 \propto \frac{A(L_{Yb} + L_{\mathrm{pas}})}{1 - \exp\{-N_0 \sigma_a \Gamma A L_{Yb}/A_{\mathrm{clad}}\}}. \tag{4.7}$$

Increasing N_0, σ_a and decreasing A_{clad} will increase the pump absorption and hence reduce the pulse duration. The influence of the core area and the active fiber length is not trivial, and therefore in Fig. 4.16 the pulse duration is calculated for fibers with core diameters between 5 μm and 20 μm. It is seen that the smallest fiber core results in the shortest pulse duration. However, if one wants a fixed high peak power obtained at the same pump absorption efficiency, then the required active fiber length increases rapidly when the core diameter decreases. This is illustrated in Fig. 4.16 with the dashed line, which corresponds to a pump absorption efficiency of 10 dB and a peak power of 615 W. Unfortunately, the combination of small core diameter and long fiber length can be problematic due to nonlinear effects.

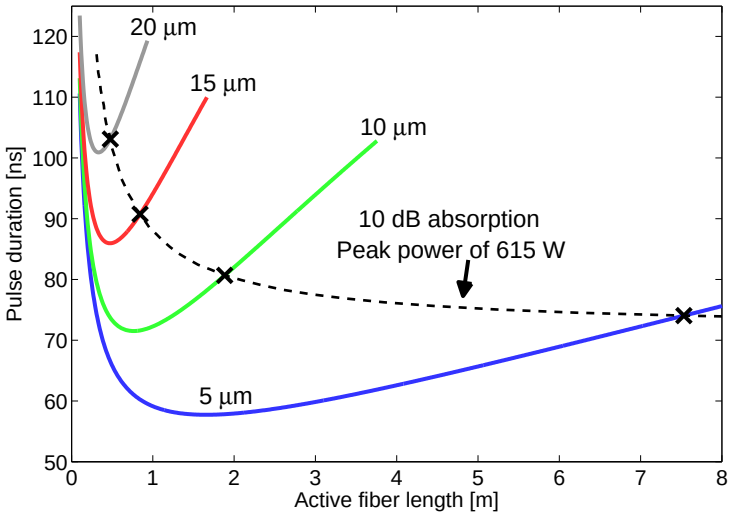

Figure 4.16: Calculated pulse duration versus length of the active fiber for fiber core diameters between 5 μm and 20 μm. The 'x's corresponds to 10 dB absorption efficiency and the peak power will at these points be 615 W for all core diameters. It is calculated by Eq. (3.22) using a pump power of 75 W, $N_0 = 9 \times 10^{25}\text{m}^{-3}$, $\sigma_a(976\ nm) = 2.5 \times 10^{-24}\text{m}^2$, $\Gamma = 0.85$, $A_{\text{clad}} = 0.25\pi 125^2 \mu\text{m}^2$, and $L_{\text{pas}} = 0.5\text{m}$.

Gain-switched all-fiber lasers are commonly constructed with FBGs that add a certain length of passive fiber to the cavity as is the case in configuration B, C, and D. Thus, it is important to take into account that the length of passive fiber in the cavity induces a minimum in the pulse duration as function of active fiber length [52].

As an example of the advantage of having obtained the factors that determine the pulse duration explicitly, a result in [109] will now be re-

visited. In the paper a Tm-doped fiber laser with varying cavity length was gain-switched, and it was found that the pulse duration was sub-linear with the cavity length. It was suggested that a nonlinear pulse narrowing could be responsible. However, by realizing that $t_0 \propto \sqrt{L}$ according to Eq. (3.20) the observed behavior is well explained.

The product of the peak power and pulse duration gives the output pulse energy E as argued in Eq. (4.4). As both constituents are given explicit in Eqs. (4.3) and (3.22), the pulse energy can easily be estimated. It can be seen that it scales as $E \propto \sqrt{ALP_{\mathrm{abs}}}$. This is in contrast to Q-switching, where it has been shown that the maximum energy that can be extracted from a fiber is about 10 times the saturation energy, $E_{sat} = A\hbar\omega/\Gamma(\sigma_{e\omega} + \sigma_{a\omega})$ [10]. The significant difference is that the pulse energy in GS has a dependence on the cavity length. The upper limit of the pulse energy will be given by the nonlinearities and the damage threshold of the fiber.

Given this results it can be estimated that a pulse energy of 2 mJ can be extracted using a state of the art pump (∼600 W) and 30 m large mode area fiber (30 μm core diameter). For such pulses the estimated peak power exceeds 5 kW, the pulse duration is less than 350 ns, and the average power is more than 250 W when the pump is driven with a realistic duty cycle of 50%.

It is interesting that in Eq. (4.4) the value of $\underline{\beta}$ and η_s show little deviation for other Yb-doped fiber lasers, hence one can estimate that $t_{\mathrm{on}} \approx 11t_0$. So when a small pulse duration is desired (for example 30 ns), the pump pulse duration should also be short (about 330 ns) and the rise and fall times of the pump pulse should be even smaller (<100 ns), which can be challenging.

In the analysis of the required off-time to empty the cavity sufficiently, it is found that the off-time should be around 100 times the cavity decay time under typical conditions. The obtainable repetition rate can therefore be estimated from knowledge of this number and the fact that the on-time is about 11 times the pulse duration.

4.7 Summary

Gain-switching is a cost-effective method for constructing pulsed fiber lasers and is interesting for many applications. This study on cladding-pumped gain-switched fiber lasers is motivated by the power scalability and simplicity of such lasers.

During this project several configurations of gain-switched Yb-doped cladding-pumped all-fiber lasers have been constructed. A range of dif-

ferent active fibers, lengths of active fibers, fiber Bragg gratings, pump powers, and pump wavelengths have been investigated. Based on these experimental results and the results of the modeling work described in the previous chapter, several conclusions have been drawn.

The peak power is shown to depend linearly on the absorbed pump power and the slope of 9.1 W/W is independent of the active fiber length in the cavity.

The pulse duration can be described by a derived theoretical expression based on a linear stability analysis of the homogeneous rate equations of fiber lasers. The pulse duration has a square root dependence on the cavity length and the core area, and an inverse square root dependence on the absorbed pump power.

The bandwidth is found to broaden due to self-phase modulation, and at high pump power levels the spectral quality can be degraded due to lasing in side-lope wavelengths of the fiber Bragg grating.

The influence of the repetition rate has been examined in the complete kilohertz range. From this discussion the requirements for efficient GS of a fiber laser have been put forward;

- The pump pulse duration should be close to the build-up delay time, which is approximately given by a constant factor times the output pulse duration.

- The off-time should be much shorter than the lifetime of the excited ions ($t_{\text{off}} \ll \tau_2$), hence the repetition rate should be in the tens of kilohertz range.

- The off-time should be much longer than the cavity decay time ($t_{\text{off}} \gg \tau_c$) and a factor of 100 is found to be the minimum under typical conditions.

The presented results are at this moment the state-of-the-art within gain-switched Yb-doped fiber lasers, and following records have been claimed (independently): the highest peak power of 8.9 kW, the highest average power of 29 W, the shortest pulse duration of 41 ns, the narrowest bandwidth below 0.1 nm, and highest pulse energy of 150 μJ.

Chapter 5

Quasi-continuous wave supercontinuum generation

In this chapter the physical processes involved in supercontinuum (SC) generation are briefly reviewed and a numerical simulation is used to illustrate the typical broadening mechanisms. The dynamics, which dominate quasi-CW pumped SC, are described and confirmed experimentally. Three series of PCFs are pumped by pulses from a GS fiber laser and the spectral properties are discussed. Optimized PCFs are suggested based on the obtained results. Most of the presented results are published in [78, 173, 177].

5.1 Supercontinuum generation

The remarkable process of SC generation in optical fibers is fairly well-understood [12–14, 178]. As the mechanisms have been described in much detail elsewhere e.g. in [14], only a very brief summary will be given here. Instead SC generation will be visualized by a series of spectrograms in Figs. 5.1, 5.2, 5.3, and 5.4.

The SC generation is, for picosecond or longer pulses, initiated by the modulation instability (MI), which require that the pump wavelength is close to the zero dispersion wavelength (ZDW) and within the anomalous dispersion region. The MI creates a number of solitons in the anomalous dispersion region. A large number of dispersive waves are formed in the normal dispersion region below the pump wavelength. The solitons redshift due to stimulated Raman scattering and can through four-wave mixing trap the dispersive waves causing them to blueshift resulting in group velocity matching (GVM) of the spectral edges [13, 178–183].

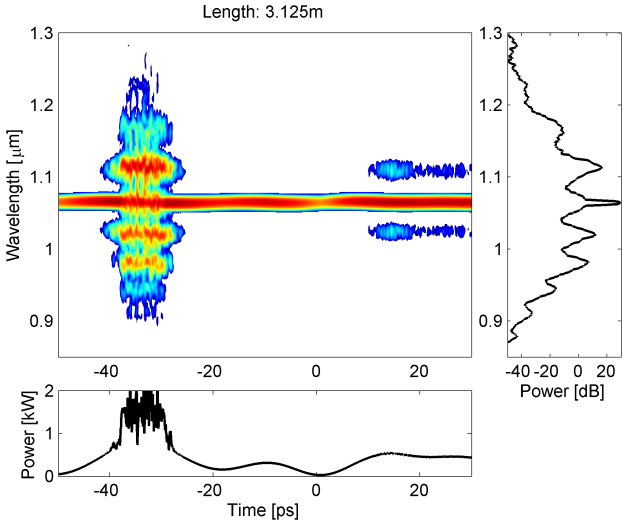

Figure 5.1: Initial stages of SC generation at 3.1 m. The incoherence of the pump results in varying pump power on the ~ 40 ps time scale. At 15 ps the characteristic symmetric spectral side-bands of the MI process can be seen. The instantaneous power was initially high around -35 ps and the broadening has advanced to a stage where cascaded side-bands appear.

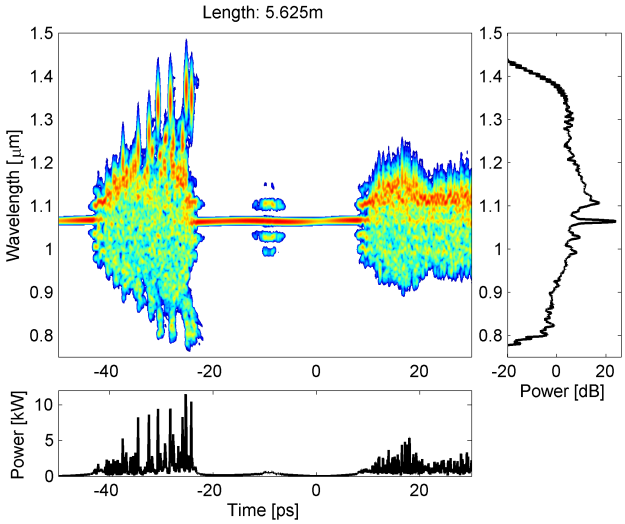

Figure 5.2: Early soliton formation stage of SC generation at 5.6 m. At -25 ps the MI Stokes band has evolved into discrete solitonic pulses between 1.25 μm and 1.45 μm.

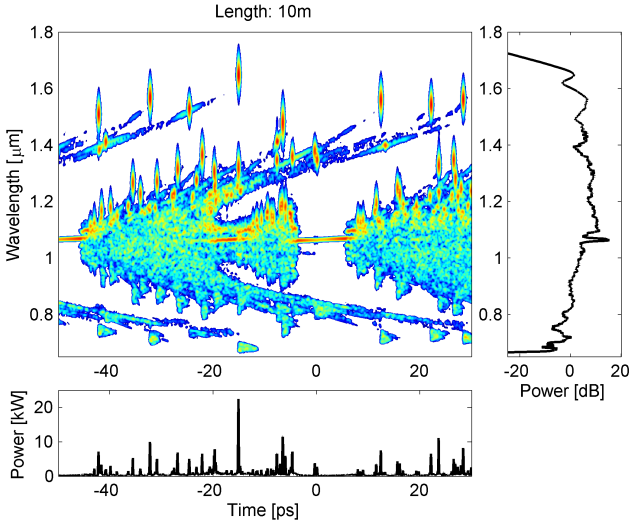

Figure 5.3: Formation of a soliton Raman continuum and trapping of dispersive waves. The large number of solitons redshift by intra-pulse stimulated Raman scattering and are delayed because of the reduced group velocity at longer wavelengths. Each soliton has trapped a package of dispersive waves at the short wavelengths. At -15 ps two solitons overlap temporally and the instantaneous power exceeds 20 kW.

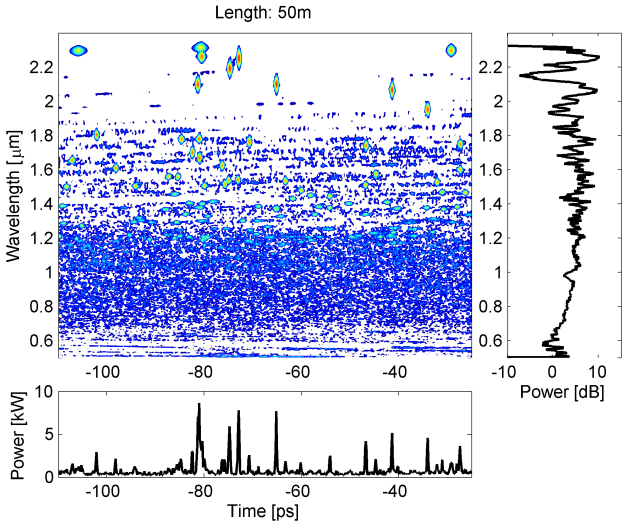

Figure 5.4: Terminal stage of SC generation at 50 m. The largest solitons have redshifted to the loss edge at 2.25-2.3 μm. The soliton energy drops whereby the redshift is ceased, and the spectral edge is formed. Less energetic solitons at shorter wavelengths continue to redshift.

The spectrograms in Figs. 5.1, 5.2, 5.3, and 5.4 give insight into the dynamics of SC generation. The principle behind these spectrograms is to analyze the frequency components in a narrow time (gate) window. The spectrogram can be defined $S(t', \omega) = |\mathcal{F}[\tilde{A}(t) \exp\{-(t - t')^2/2\sigma_t^2\}]\omega|^2$, where σ_t is the width of the gate window. The interpretation of the processes are described in the figure text.

The numerical simulation shown here is obtained by the GNLSE presented in section 2.5.2. The parameters used are as follows: the average pump power is 500 W, the spectral bandwidth is 0.1 nm which corresponds to a coherence time of ∼40 ps, the number of numerical steps is 2^{17}, the maximum local error is 10^{-3}, the maximum step size is 125 μm, the time resolution is 2 fs, the time window is 270 ps, and losses are included as shown in Fig. 5.6. The degree of chromatic dispersion used has been calculated for a PCF with $d/\Lambda = 0.48$ and $\Lambda = 3.4$ μm, hence the PCF corresponds closely to the tested fiber F10 (see Table 5.1). Simulation time was about 38 hours. The spectrogram gate width is $\sigma_t = 200$ fs, and the color scale and the wavelength range have been changed in each figure to enhance the details. The spectra shown to the right have been averaged over a span of 4 nm.

5.1.1 Quasi-CW SC generation

It can be seen in the spectrograms that the SC generation dynamics occur on a time scale of femtoseconds to picoseconds. This is much shorter than that of pulses generated by GS, which are hundreds of nanoseconds in duration. The mechanisms involved in SC generation therefore experience the envelope of nanosecond pulses as a quasi-continuous wave (quasi-CW). A more rigid argument is that if any components of the SC are delayed due to chromatic dispersion by a significant amount compared to the pump pulse duration, the SC cannot be considered quasi-CW.

For a PCF with one ZDW, the generated spectral edges are the most delayed relative to the pump (which is close to the ZDW). In a typical PCF the temporal walk-off per unit fiber length between the pump and the loss edge at 2300 nm is around 80 ps/m. In our case of fibers with a length of 100 m, this smearing corresponds to at maximum 8 ns, which is much shorter than the duration of the pump pulses at more than 200 ns. Therefore, the SC process can be considered quasi-CW.

5.1.2 Modeling of quasi-CW SC generation

SC generation has been modeled extensively in the literature using the GNLSE in Eq. (2.27) [13,14]. However, modeling of CW SC generation has not be carried out routinely for two reasons [184–187]; the large computational demand required and the difficulty in accurately representing the incoherent CW field.

An accurate description of the input field is important because longitudinal mode beatings in CW pump lasers result in enhancement of the instantaneous power (peak power) in a short time duration characterized by the temporal coherence of the pump laser. The temporal coherence is connected to the spectral bandwidth [185,186]. In [188] a variety of input models were compared and a phase diffusion model with one photon per mode noise showed in general the best agreement with experimental results. This approach is therefore used in the simulation shown in the spectrograms.

In a simulation the temporal window should be around 600 ns to cover the entire pulse. With a temporal step size around 2 fs, this gives $2^{28} = 3 \cdot 10^8$ numerical points, which corresponds to 4 GB of data. With the computers of today this is in principle possible; however, the combination of long lengths of hundreds of meters of fiber and the high number of time steps makes it extremely computationally heavy.

Alternatively, the input field can be split into $2^{16} - 2^{18}$-point segments, which correspond to a width of 100-500 ps. This approach is used in the simulation of the SC in the spectrograms, however the validity can be questioned because the most redshifted solitons will pass more than 20 times through the temporal domain due to periodic boundary conditions. For this reason the numerical simulations are only used in this project for visualization of the SC dynamics.

5.2 Review of CW and quasi-CW supercontinuum generation

In typical continuous wave (CW) SC experiments, a PCF is pumped by a high-power fiber laser, which has an average output power of 10 W to 100 W. The drawback of such pump lasers are the reduced peak power compared to pulsed pumping, which leads to less broadening and the need for longer fiber lengths. Especially the generation of light at shorter wavelengths than the pump wavelength is troublesome [48, 50, 50, 87, 143, 189–191]. The advantages of using a CW pump are that the complexity of the system is reduced, a higher average power, and a

higher power spectral density can be obtained.

In the following a brief review of high-power CW SC in PCFs will be given. More thorough reviews covering the discovery of the nonlinear effects, SC standard fibers, and pulsed SC in PCFs can be found elsewhere [74, 192, 193].

In state-of-the-art CW SC generation pump powers of 100 W is routinely used and even a 400 W fiber laser has been tested [48, 50, 190, 191, 194]. Lengths of 20 m to 400 m of PCF with reduced OH-loss are used. Designs based on Ge-doped cores and tapered fibers have recently been investigated [50, 190, 194, 195]. The improved performance of these designs is due to an increased nonlinearity by Ge-doping and a shift of the short and long wavelength edges depending on the design of the tapering [178, 180, 196–198].

In [48] a 400 W laser was used for pumping pure silica PCFs and a spectrum spanning from 1060 nm to the loss edge of silica (>2200 nm) was obtained. In another fiber with a ZDW only 20 nm shorter than the pump wavelength, a spectrum spanning from 600 nm to 1900 nm was obtained. In [50] a PCF with a Ge-doped core is pumped at a pump power of 100 W and a resulting spectrum spanning from 550 nm to ∼2100 nm was demonstrated. By tapering the spectrum was extended down to 450 nm [50].

The influence of the spectral bandwidth of the pump laser was investigated in [185, 186, 199], and it was shown that an optimum degree of coherence of the pump exists for which is the MI process is most efficient.

The benefits of CW pumping compared to pulsed pumping are, as mentioned, the higher average power, simplicity of the setup, and a higher degree of flatness of the SC. The challenges are the long fiber lengths, where the fiber loss can become significant, and the need for high average pump powers to obtain sufficient broadening [48, 50].

At very high CW power levels (hundreds of Watts) destructive heating problems occur and pulsing of the pump laser is necessary to avoid these [48, 200]. In doing so the pump is not strictly CW. The pulse peak power of the slowly modulated pump has been referred to as the switched-on or equivalent power [48,200] but the term 'quasi-CW power' is found more descriptive and it will be used in the following.

Slow on/off-modulation of the pump laser is often applied to reduce the thermal stress in the splices and at the end-facet of the nonlinear PCF, due to the high average power [48, 191]. This modulation is typically done in the 100 Hz range and SC results are considered purely CW-pumped.

In [191] the modulation of a CW fiber laser at a repetition rate of 7.8 kHz was reported to 'enhances the continuum beyond that expected from the peak-power increase alone', which could indicate that the authors might have generated spikes.

Another approach was reported that did not rely on relaxation oscillations, but instead used a master oscillator power amplifier configuration with an acousto-optical modulator after the seed CW laser. Here short nanosecond pulses were generated with hundred Watt peak power level [143], which are quite similar to the pulses produced by GS, however such a system is more complex and is not monolithic.

5.3 Fibers and the experimental method

A schematic of the setup used in the SC experiments is shown in Fig. 5.5. The laser configuration A is exclusively used in the SC generation experiments. A maximum coupled quasi-CW power (peak power) of between 500 W to 600 W is used depending on the splicing loss and pulse setting, and the average power coupled to the PCFs in GS operation is fixed to 21 W by varying the repetition rate – unless stated otherwise. For comparison the fibers are also CW pumped by a coupled average power of 21 W. The minimum pulse duration is 210 ns.

In the experiments a PCF with a length of 100 m is spliced to the output fiber of the gain-switched fiber laser by use of an intermediate fiber, which reduces the mode field diameter from 15 μm to 4 μm to match the nonlinear PCF. The total splice loss is between 0.7-1 dB. The output of the fiber is launched into an integrating sphere or a power meter. The visible and infrared spectra are measured with a 350-1750 nm or a 1200-2400 nm optical spectrum analyzer, respectively. The spectral resolution is 2 nm. The spectra are normalized to the output power and the visible and infrared spectra are stitched at 1500 nm. The spectral response function of the fiber between the integrating sphere and the optical spectrum analyzer is taken into account.

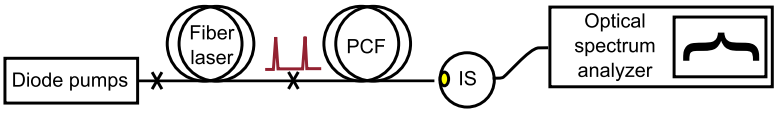

Figure 5.5: Experimental setup consisting of the GS fiber laser that is spliced to a PCF. The SC light is launched into an integrating sphere (IS) that is fiber-coupled to an optical spectrum analyzer. The laser configuration A is exclusively used in the SC generation experiments.

The properties of the used PCFs are summarized in Table 5.1. The relative hole size d/Λ and pitch Λ are measured by an optical microscope with 100x magnification. The fiber group velocity dispersion (GVD) is measured by a white light low-coherence interferometric method [29, 201]. The fully vectorial finite-element method described in section 2.4 is used to calculate the GVD and nonlinear parameter γ. There is in general good agreement between the measured and calculated GVD when taking the uncertainties of the optical measurement of the hole size into account. The dispersion parameters β_2 and β_3 are defined by Eq. (E.8).

The PCFs are fabricated at NKT Photonics using the stack and draw method. They are all single-mode at 1064 nm and have a low OH loss at 1380 nm of <25 dB/km and a background loss of <5 dB/km between 800 nm and 1750 nm. The G-fiber series has a OH-loss of > 500dB/km due to that the Ge-doped silica in the core was not purified sufficiently. The typical attenuation of the fibers is shown in Fig. 5.6, which increases exponentially towards 2300 nm [77].

The fibers E34 and E89 are commercially available (at NKT Photonics A/S) under the product names SC-5.0-1040 and SC-3.7-975, respectively. Both PCFs have been optimized to short-pulse pumping with a coupled peak power of around 10 kW.

The fibers in the F-series have been fabricated to have the ZDW on either side of the pump wavelength of 1064 nm. Their calculated dispersion profiles are shown in Fig. 5.6, where it is seen that the major difference is the ZDW and that only at the very long wavelengths the slopes deviate.

The G-fiber-series is fabricated to enhance the nonlinearity by doping of the core by a high density of Ge. This increases the confinement and the intrinsic nonlinearity $\underline{n_2}$, which both contribute to an increased nonlinear parameter γ of about a factor of 4-5. The GVD is designed to position the ZDW close to but below the pump wavelength of 1064 nm.

5.4 Quasi-CW supercontinuum experiments

In this section quasi-CW SC generation is investigated experimentally by pumping a series of PCFs by a GS fiber laser. Special attention is paid on the dynamics that are specific for quasi-CW SC generation. The tested fibers are from the F-series and represent both anomalous and normal GVD at the pump wavelength. By sweeping the dispersion, valuable insight into the SC dynamics can be revealed. The influence of

Fiber	d/Λ	Λ μm	ZDW nm	γ $(\mathrm{Wkm})^{-1}$	β_2 $\mathrm{ps}^2\mathrm{km}^{-1}$	$\beta_3 \cdot 10^2$ $\mathrm{ps}^3\mathrm{km}^{-1}$
E34	0.52	3.25	1030	12.0	-4.22	7.40
E89	0.52	2.6	975	18.0	-12.1	8.26
F24	0.47	3.2	1040	11.3	-2.82	7.21
F10	0.47	3.4	1054	10.1	-1.12	7.02
F-6	0.47	3.6	1070	8.9	0.67	6.78
F-27	0.47	4.0	1091	7.5	2.87	6.51
G34	0.55	2.0	1030	51	-6.18	10.3
G24	0.55	2.1	1040	48	-3.54	9.79
G9	0.55	2.2	1055	46	-1.70	9.80

Table 5.1: Characteristic PCF data. The fiber name refers to the detuning of the ZDW from the pump wavelength of 1064 nm. The measured relative hole size d/Λ, pitch Λ, calculated nonlinear parameter γ at the pump wavelength, ZDW, and calculated dispersion parameters β_2, and β_3 at the pump are given. The core of the G-fibers are highly doped with Ge ($\Delta n = 2.01\%$ or approximately 19%mol) and the diameter of the Ge-rod is 0.74Λ. It has been assumed that $\underline{n}_2 = 2.6 \cdot 10^{-20}$ m^2/W in the pure silica fibers and $\underline{n}_2 = 3.38 \cdot 10^{-20}$ m^2/W in the Ge-doped fibers.

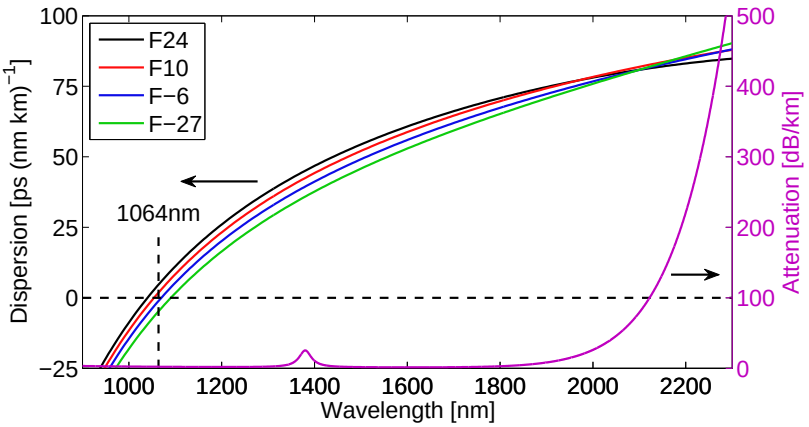

Figure 5.6: The calculated dispersion of the four fibers in the F-series with the pump at 1064 nm indicated by a dotted vertical line. On the right axis the typical fiber attenuation is shown.

increasing the pump power and fiber length on the SC spectrum is also discussed.

5.4.1 Spectral broadening in the quasi-CW regime

In Fig. 5.7 the output spectra of fiber F24 pumped by coupled quasi-CW powers of 21 W (CW), 200 W, and 500 W are shown. Here, the pump wavelength is in the anomalous GVD regime, which allows MI to split the pump into soliton-like pulses that Raman redshift [13,14]. The MI characteristic peaks are not visible due to the subsequent broadening processes. It is observed that by increasing the pump power the infrared edge is shifted to longer wavelengths. Thus, a higher pump power causes a stronger redshift of the generated solitons.

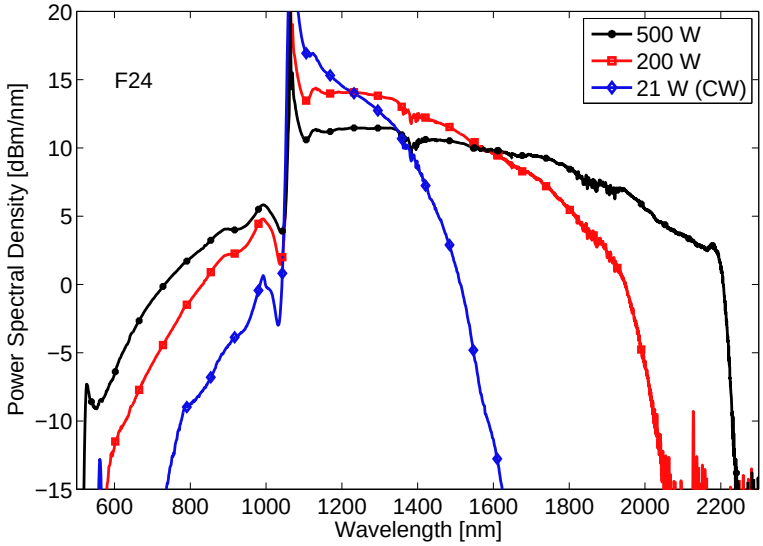

Figure 5.7: Output spectra of the fiber F24 pumped by pulses with quasi-CW (peak) powers of 500 W, 200 W, and CW pumped with 21 W. The coupled average power is 21 W for all spectra.

This is well-known and can be explained through the relations for the soliton energy and the soliton self-frequency shift [12]. On average the MI process generates a fundamental soliton for each MI period t_{MI} and given the quasi-CW pump power P_{QCW}, the average soliton energy can be approximated by [12, 185]

$$E_{sol} = P_{QCW} t_{MI} = 2P_0 T_0 = \sqrt{\frac{2\pi^2 |\beta_2| P_{QCW}}{\gamma}}, \tag{5.1}$$

where P_0 is the soliton peak power and T_0 is the soliton duration. Using this, the analytical expression for the rate of soliton self-frequency shift in the long soliton duration limit becomes [12, 87, 197, 202]

$$\frac{d\omega(z)}{dz} = -\frac{4|\beta_2(\omega)|T_R}{15\pi T_0(\omega)^4} = -\frac{T_R\gamma(\omega)^4\{E_{sol}\frac{\omega}{\omega_0}\}^4}{60\pi|\beta_2(\omega)|^3}, \tag{5.2}$$

where the shift of the soliton frequency $\omega(z)$ is proportional to the Raman gain slope $T_R = 3$ fs and is strongly dependent on the soliton duration. It has been used that for a fundamental soliton the duration is given by $T_0 = \sqrt{|\beta_2|/\gamma P_0}$. The factor $(\omega/\omega_0)^4$ is included to take the inelasticity of Raman scattering into account [203] and ω_0 is the pump angular frequency. Using Eqs. (5.1) and (5.2) it is clear that by increasing the quasi-CW pump power, the soliton energy is increased and it will consequently redshift to a longer wavelength. The process is self-limiting because all frequency-dependent terms reduce the redshifting rate with lower frequency.

The experimental result, i.e. the infrared edge of the SC spectrum, is now compared to the redshift of a single soliton generated by the MI process. The redshift of a single soliton is estimated by numerical integration of the ordinary differential equation in Eq. (5.2) over the fiber length of 100 m and by simulation of the generalized nonlinear Schrödinger equation. Good agreement between the two results is found. The experimental redshift is evaluated at the -10 dBm/nm level of the steep infrared edge of the SC.

At the quasi-CW power of 21 W the single soliton redshift amounts to 4.3 THz, whereas the experimentally found redshift is 93 THz (525 nm). At the increased quasi-CW power of 200 W the single soliton redshift is 21 THz whereas the experimentally found redshift is 134 THz (965 nm). The MI period and soliton energy are shown for the fiber F24 in Table 5.2. The single soliton redshift is therefore close to an order of magnitude less than the experimentally found result. The large discrepancy is an indication of the fact that the picture of the red edge of the SC consisting of independent, redshifting, fundamental solitons generated by MI is not correct.

The spectral bandwidth of the laser is on the order of a nanometer, which leads to stochastic temporal intensity fluctuations on the few picosecond time scale [185]. These temporal fluctuations can result in a local increase in the instantaneous pump power by up to an order of magnitude [185]. Additional fluctuations are expected due to the fact that the MI process is seeded by intrinsic noise, which leads to a minor variation in the MI period and hence the soliton energy. To get an

Fiber	P_{QCW} W	t_{MI} fs	E_{sol} pJ	$\Delta\nu_{th}$ THz	$\Delta\nu_{exp}$ THz
F24	21	484	10	-4.3	-93
F10	21	323	7	-3.7	-88
F24	200	157	31	-21	-134
F10	200	105	21	-15	-125
F24	500	99	50	-32	-148*
F10	500	66	33	-23	-146*

Table 5.2: MI period t_{MI}, soliton energy E_{sol}, the analytical $\Delta\nu_{th}$ and experimental redshift $\Delta\nu_{exp}$ at increasing pump power P_{CW} for fibers F24 and F10. *The redshift is limited by the high infrared attenuation at 2300 nm shown in Fig. 5.6.

idea of the influence of these noise fluctuations the worst-case scenario is considered, in which they lead to an increase in the soliton energy by a factor of two. Thus, by combining these two effects the soliton energy can be increased by a factor of $\sim 2\sqrt{10}$ through Eq. (5.1). The redshift is now expected to be much larger as the soliton energy appears in the fourth power in Eq. (5.2). By carrying out the numerical integration the redshift in this case amounts to 40 THz (at 21 W pump), which is still much weaker that the experimentally found result of 93 THz. In fact, it turns out that in order for a single MI generated soliton to redshift 93 THz, an increase of the soliton energy of a factor of 30 is required (300 pJ). Such a large value is needed due to the term $\gamma^4|\beta_2|^{-3}$, which decreases rapidly with decreasing frequency. It can therefore be concluded that the experimentally obtained redshift cannot be explained by independent MI generated, redshifting solitons, even if the partial coherence of the pump and noise-seeded MI is taken into account.

Instead of treating the solitons as being independent, one has to consider the inevitable interaction between the solitons. Temporally overlapping solitons can interact and exchange energy through four-wave mixing and Raman scattering in so-called inelastic soliton collisions [39, 87, 204, 205]. In noise-seeded MI-based SC generation these collision events are stochastic and can generate high peak power solitons that have been compared to freak or rogue waves [206–209]. Even without the Raman term such large solitons can be generated by collisions [210]. In high-power CW and quasi-CW pumped SC generation the number of solitons is very large and a substantial number of soliton collisions can occur. This is further facilitated by long interaction lengths and large temporal walk-off due to chromatic dispersion. When a large number of collisions have taken place some solitons have gained

sufficient energy to redshift to significantly longer wavelengths than a single MI generated soliton is able to. These collisions can therefore explain the large experimentally observed redshift.

At the highest quasi-CW power of 500 W the infrared edge at 2230 nm is steep due to the strongly increasing material loss. This behavior is observed with a coupled quasi-CW power above 350 W (not shown). No significant improvements in the bandwidth can be expected for a given PCF design by increasing the power above this value due the cancellation of the soliton redshift and therefore also the blueshift of the group-velocity matched visible edge. The current record pump power is 230 W of coupled CW power [48] and due to extensive heating, it is considered cumbersome to reach 350 W. Therefore, to obtain a loss-limited SC the CW pump must be modulated.

The light generated below the pump wavelength consists of MI anti-Stokes components (at 1028 nm) and soliton generated dispersive waves [48]. Using the approach in [211] and by assuming a soliton peak power P_0 of 0.5–1 kW, the pump can form dispersive waves at ∼980-990 nm, which fits well with the feature in the spectra of F24 in Fig. 5.7. The subsequent trapping interaction between dispersive waves and the redshifting solitons extends and flattens the visible part [182]. As a result of this interaction the visible and infrared edges are group-velocity matched [183]. These processes are more efficient at the highest quasi-CW power, which can be seen by the amount of visible light generated.

5.4.2 Cutback

The SC dynamics can also be revealed by examining the progress of the broadening at various fiber lengths. In fig. 5.8 a cutback of the F10 fiber pumped by a launched quasi-CW power of 500 W is shown. It can be seen that within the first few meters MI peaks are generated and soon after redshifting solitons form the long wavelength edge of the spectrum. The short wavelength edge is formed from dispersive waves trapped by, and hence obtain GVM to, the redshifting solitons.

The MI peaks shift closer to the pump wavelength within the first 10 m. This can be explained by the characteristics of the injected Gaussian-like pulses. These pulses have a broad power distribution and the quasi-CW power in the SC processes is therefore given by this broad distribution. The highest power components broaden first and have the most separated MI peaks. The low power components develop MI peaks later in the fiber that are closer to the pump. Another contributing effect is depletion of the pump of the MI process.

The visible wavelengths are predominantly generated during the first about 20 m. After more than 70 m the spectrum is almost fully developed and attenuation is the dominant process that define the spectral edges.

These experimental observations are in good agreement with the interpretation of the spectrograms in sections 5.1.

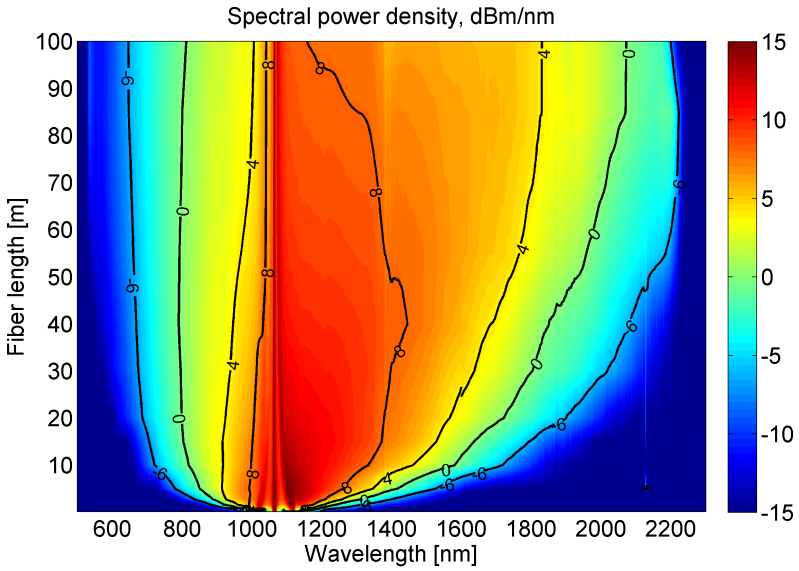

Figure 5.8: Experimental SC spectrum in F10 as function of fiber length where the contour lines and the color represents the spectral power density. The fiber is pumped by 500 W coupled quasi-CW power and 9 W average power. The spectra are measured a different lengths. A smoothing algorithm has been applied.

5.4.3 Varying the Anomalous Dispersion

The GVD and ZDW is crucial for the MI process [13] that initiates the broadening. The position of the ZDW relative to the pump wavelength has been studied using various pulsed pumps with peak powers above 2.5 kW [212–214] and CW pumps with several tens of Watts of CW power [195, 200, 215–217]. From these studies it is found that, the most efficient use of the MI process is achieved when the GVD at the pump wavelength is weak and anomalous.

The fibers F24 and F10 both have anomalous GVD at the pump wavelength, and as seen in Table 5.1 they have different values of β_2 but all other parameters are almost constant. This enables us to examine the influence of β_2 on the broadening at the high quasi-CW power levels.

In Table 5.2 the MI period, the soliton energy, the estimated redshift $\Delta\nu_{th} = (\omega(0) - \omega(z))/2\pi$ (found by integration of Eq. (5.2)), and the experimental redshift $\Delta\nu_{exp}$ (-10 dBm/nm edge) are shown for the fibers at the quasi-CW power levels 21 W, 200 W, and 500 W. The fibers F-6 and F-27 are omitted due to a different initial SC process, as will be discussed later.

It can easily be shown that the redshift rate scales with β_2^{-1}, by inserting Eq. (5.1) into Eq. (5.2) and ignoring the wavelength dependencies. In CW SC generation results in the literature at a pump power of 10 W this approach is used to explain that the lowest anomalous dispersion maximizes the soliton redshift [14, 218]. Under this assumption the fiber F10 would result in the most redshifted solitons, which is in contrast to our results shown in Table 5.2. The wavelength dependencies can therefore not be neglected. The soliton redshift rate in the F10 fiber is initially faster than in fiber F24, but due to similar $\beta_2(\omega)$ of the two fibers after the initial redshifting, the soliton energy term in Eq. (5.2) dominates.

It can be seen in Table 5.2 that in fiber F24 the soliton energy is about 50% larger than in F10 due to a longer MI period. The spectrum is therefore expected to have an infrared edge at longer wavelengths. The difference in the estimate of the single soliton redshift between the two fibers can be seen to be about 30%. However, at the pump power of 200 W, e.g. the difference in the experimental redshifts is only 7% (9 THz). It is noteworthy that even though the soliton energy is 50% higher in fiber F24 than fiber F10 the bandwidth is only slightly larger. This can be explained by the fact that in F10 the MI period is shorter, which increases the number of generated solitons. This in turn increases the likelihood of soliton collisions and enables the large redshift.

It has therefore been shown that in high power CW SC in a fully-developed spectrum the largest redshift is not obtained with the lowest value of the anomalous dispersion, but a slightly higher value can be advantageous. However, these differences almost vanish due to the fact that the soliton collisions dominate the SC broadening.

5.4.4 Normal Dispersion Pumping

The PCFs examined have ZDWs that are positioned on either side of the pump wavelength, which means that the pump experiences either normal or anomalous GVD. The influence of the ZDW is shown in Fig. 5.9 for the PCFs pumped with the quasi-CW power of 500 W. The broad bandwidth and spectral shape are similar for all the fibers. However, important differences can be extracted.

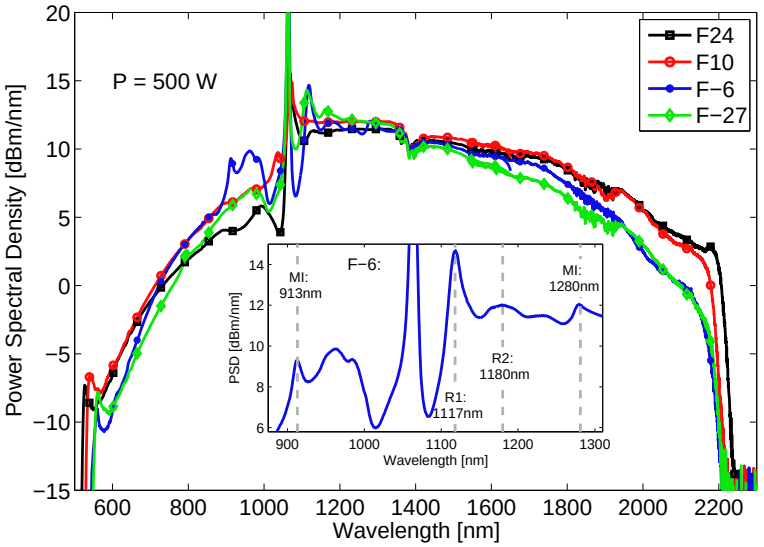

Figure 5.9: Output power spectral density for a coupled quasi-CW peak power of 500 W. The coupled average power is 21 W and the average output power is around 13.5 W for all fibers. The inset shows the spectrum of F-6 with marked MI and Raman (R) features.

The process of splitting the pump into solitons cannot (initially) take place in fibers F-6 and F-27 in which the pump wavelength is in the normal GVD regime. From the close-up of F-6 in the inset of Fig. 5.9 the dynamics can be deduced. An intense peak (R1) is present at 1117 nm, which corresponds to the Raman shift of the pump at 1064 nm [215,216]. The Raman threshold length is $L_{\text{eff}} = 16A_{\text{eff}}/g_R P_{th}$ [12], which at 500 W results in a length of ∼5 m and this is much shorter than the fiber length of 100 m. The pump light that is rapidly transferred to the Raman wavelength now experiences anomalous GVD in both fibers. After this additional conversion process the SC generation is equivalent to the one in F24 and F10, which explains the striking similarity of the spectra.

The close-up in Fig. 5.9 also shows some additional spectral features that are not found in the other spectra. Besides the first Raman Stokes peak at 1117 nm, a peak (R2) can be seen at 1180 nm, which corresponds to the second Raman Stokes order. The MI process in the normal GVD regime is in general characterized by widely separated Stokes and anti-Stokes components [219]. An MI anti-Stokes peak at 913 nm and an MI Stokes peak at 1280 nm have been identified by use of the calculated GVD profile. The formation of the MI anti-Stokes peak with high spectral power is responsible for generation of the features at 955 nm

and 985 nm, which can be attributed to Raman scattering of the MI anti-Stokes peak at 913 nm.

5.4.5 The Bandwidth Variation

The SC bandwidth at the -10 dBm/nm level for the four fibers in the F-series pumped with a quasi-CW power of 500 W is between 1645 nm and 1710 nm as can be seen in Fig. 5.9. This variation of the bandwidth with the ZDW is small and can be quantified to a relative value of only 4%. There are two reasons for the similar bandwidth. Firstly, in the fibers with normal dispersion at 1064 nm, the pump is effectively transferred into the anomalous dispersion region through Raman scattering. Secondly, the infrared edge is limited by the silica loss and this limits the visible edge through GVM. This means that the fiber core can be increased to reduce damage effects caused by the high optical intensities without sacrificing the SC bandwidth due to a longer ZDW and normal GVD.

The fiber that gives the highest amount of visible light is F10, which is due to the fact that the efficiency of the dispersive wave generation decreases with increased spacing between the pump wavelength and the ZDW [195, 220, 221]. One could consider increasing the bandwidth by designing the group velocity profile to shift the short wavelength edge. This possibility will be discussed section 5.6. However, it turns out that this will inherently reduce the ZDW and in turn lower the efficiency of the dispersive wave generation so only a negligible amount of light is generated at the short wavelengths. Extensive research has been conducted to solve this issue through cascading of two PCFs and tapering [38–40, 180, 194, 222, 223].

The influence of the ZDW on the bandwidth for the examined quasi-CW power range is shown in Fig. 5.10. At the power levels traditionally used in CW-pumping of 20 W–200 W, a bandwidth reduction is seen for the fibers with normal GVD at the pump wavelength. The relative bandwidth variations are found to be 20% and 30%, respectively. The reason for this is that the additional Raman scattering process occurring before formation of solitons in the fibers is only efficient at the highest power. Note that this variation is small compared to previous CW SC results at a pump power of 3 W, where a variation above 500% was found [217]. For the fibers with anomalous dispersion at the pump wavelength (F24 and F10) the tendency is that fiber F24 has the broadest bandwidth, which can be explained by the differences in GVM condition between the two fibers.

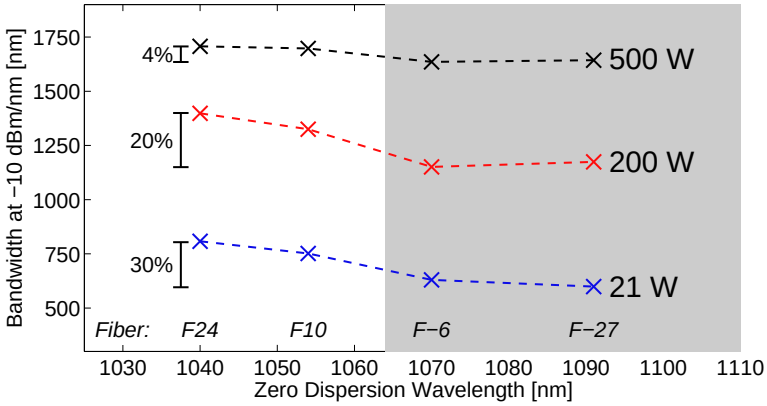

Figure 5.10: The dependence of the ZDW on the spectral bandwidth at the pump power of 21 W, 200 W, and 500 W. The bandwidth at -10 dBm/nm is shown with crosses for the four different ZDWs. The relative bandwidth variation is displayed to the left and the gray area marks that the pump wavelength has normal GVD.

5.5 Scaling the average power

It is of technological interest in some situations to achieve as high as possible average power of the SC. The analysis of the high repetition rate regime of GS in section 4.4.1 revealed that a wide range of peak powers and average powers are available. It is possible to increase the average power by increasing the repetition rate and whereby operate to the right of the optimum region in Fig. 4.7. The cost is obviously a lower peak power but it can not be taken for granted that this is the best point of operation for all applications.

In Fig. 5.11 the F24 fiber is pumped by increasing average power, whereby the peak power is determined by the linearly decreasing line to the right of the optimum region in Fig. 4.7. The actual coupled peak and average powers are stated in Fig. 5.11. It is seen that by decreasing the peak power the width of the spectrum is reduced, however the spectral power density nearest to the pump is considerably increased due to the higher repetition rate. For example, going from a peak power of 500 W and an average power of 21 W to a peak power of 250 W and an average power of 34 W (black and red lines, respectively) narrows the spectral edges by only 50-100 nm but in the range from 750 nm to 1800 nm the spectral power density increases by up to 3 dB.

This experiment demonstrates the flexibility of the GS fiber laser as a pump for quasi-CW SC generation. It is also argued that the application of the SC light determines whether the highest possible peak power is required or not.

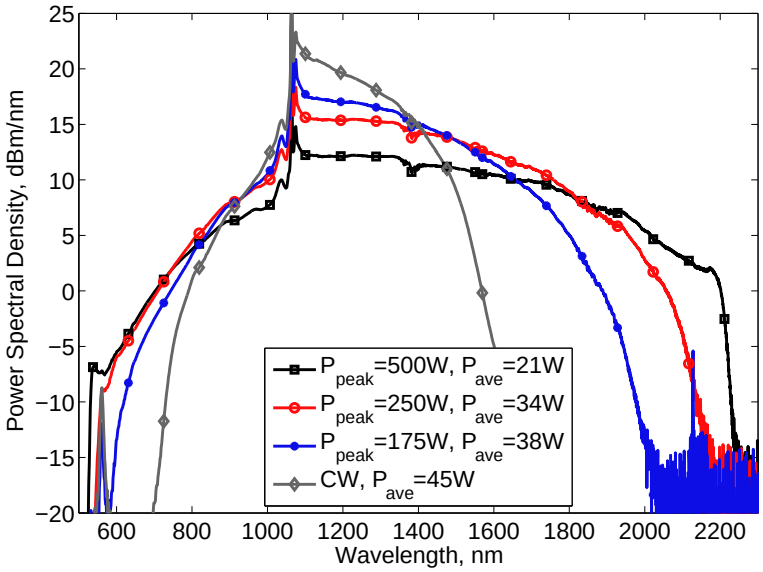

Figure 5.11: SC spectra with 85 m of the F24 fiber pumped by the fiber laser in configuration A. The SC spectra are shown for different sets of quasi-CW powers (P_{peak}) and average powers (P_{ave}). The CW pumped spectrum is also shown. The output powers are 15 W, 26 W, 31 W, and 39 W, respectively, which corresponds to optical-to-optical efficiencies above 70%.

5.5.1 Improvements of gain-switching

It is clear that a high quasi-CW power produced by GS of the pump laser is advantageous in SC generation. In principle *all* fiber lasers designed for CW operation can be gain-switched, and hence the SC generation can be improved without any modifications of (the optical components of) the fiber laser. It is therefore relevant to evaluate the improvement of taking advantage of GS operation.

In Fig. 5.12 the SC results obtained by pumping the E34 and E89 fibers in CW and GS operation are shown. The coupled peak power is about 600 W and the coupled average power is 25 W. For comparison a coupled average power of 25 W is also used for CW pumping.

In GS operation the spectrum of E34 spans from 500 nm to 2250 nm at the -10 dBm/nm level, and the total output power is 12 W. The infrared part is particular flat and has a flatness of 6 dB over a bandwidth of more than 1000 nm with a power density above 5 dBm/nm (3 mW/nm). The maximum power spectral density (when ignoring the pump) is 11 dBm/nm (12 mW/nm) at 1250 nm and the bandwidth at a power spectral density above 0 dBm/nm (1 mW/nm) is 1500 nm. The

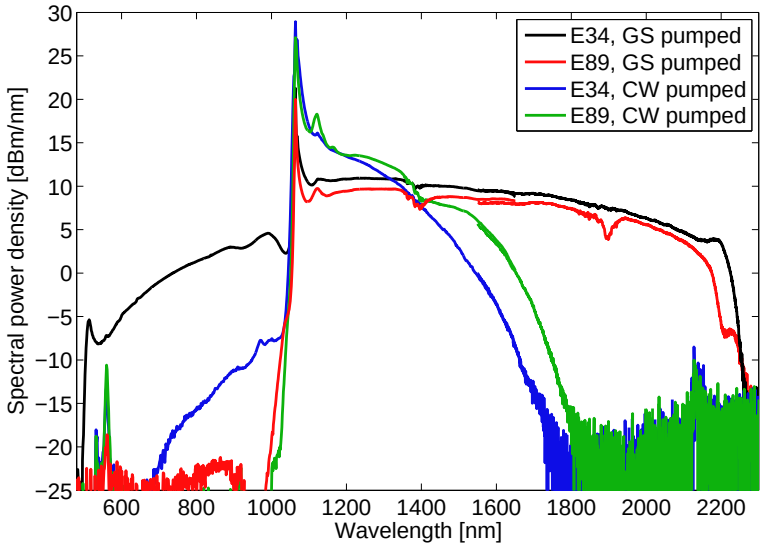

Figure 5.12: SC generation in the E34 and E89 fibers pumped in CW operation and in GS operation with 600 W of coupled peak power. The coupled average power in both modes is 25 W. The output powers of E34 are 17 W and 12 W for CW and gain-switched pumping, respectively. For E89 the output powers are around 15 W and 8.5 W for CW and gain-switched pumping, respectively.

infrared edge of the spectrum is determined by the loss edge of silica. The short wavelength side of the pump has a flatness of 6 dB over a bandwidth of 365 nm.

In CW operation the spectrum of E34 is spanning from 950 nm to 1650 nm (-10 dBm/nm level) with an output power of 17 W. The components of the spectrum above 5 dBm/nm spans only 400 nm. When operating in CW the average output power is higher because no light is generated at the infrared-loss edge.

The E89 fiber has a ZDW of 975 nm, which means that the efficiency of the dispersive wave generation is low. This can be seen in Fig. 5.12, where the short wavelength light barely exceeds the noise floor of the measurement. On the other hand the long wavelength side of the spectrum is developed to a comparable extent as the SC generated in E34. Under CW operation conversion is more efficient in E89 due to the higher nonlinear parameter of the fiber. The average output power is however lower in E89 than in E34 because less residual pump light is present at the output. It can be concluded that using the E89 fiber only the long wavelength side of the spectrum can be generated. Therefore, at the used quasi-CW power level this type of fiber is only useful if long wavelengths are desired.

5.6 Optimizing the photonic crystal fiber

In the preceding sections the SC dynamics, the influence of the quasi-CW power, and the dependencies of the GVD have been investigated. For optimum conversion efficiency and spectral broadening the GVD should be weak and anomalous, and the quasi-CW power should be as high as possible. At the highest examined power level the long wavelength limit is determined by the infrared loss edge of silica. The visible edge on the other hand is determined by the group velocity profile of the PCF used. It is therefore interesting to try to optimize the short wavelength spectral extent by studying a range of PCF designs.

The nonlinear parameter of the PCF is linked to the effective core area. However, optimizing the nonlinear parameter is ambiguous. On one hand, high confinement and thereby nonlinear parameter is desired to obtain the highest amount of broadening and enable the use of short fiber lengths. Conversely, damages occur in the fiber core in long term operation [46], which motivates the use of a large core area to reduce the optical intensity and therefore the nonlinear parameter.

Additionally, it is desired to use a PCF that is single-mode (at least at the pump wavelength) to have the highest possible beam quality. This is strictly obtained with a relative hole size of $d/\Lambda < 0.45$ [55, 59, 224].

In order to carry out optimization, the complete parameter space of pure-silica hexagonal-cladding PCFs has been calculated using a full-vectorial solver, which has been described in section 2.4. The results are compiled in Fig. 5.13. The short wavelength edge is defined through the GVM to either the infrared loss edge, which is assumed to be at 2250 nm, or if present to a second ZDW located at a long wavelength. The GVM results are shown as a color plot with contour lines for each 50 nm. The nonlinear parameter γ is shown with solid red lines. Finally, for each relative hole size (d/Λ) it is possible to vary the pitch (Λ) to obtain a ZDW at the pump wavelength of 1064 nm. This relationship is displayed as the black dashed line. Below this line the GVD is in the anomalous regime.

The desired weak and anomalous dispersion is slightly below the dashed line, and therefore the optimum pitch is located at this line as the relative hole size is increased. It is then seen that γ only changes slightly with d/Λ, and for $d/\Lambda > 0.45$ it is almost constant at a value of 9 $(\text{kW m})^{-1}$. The short wavelength edge, defined by the GVM, shifts towards shorter wavelengths with increased relative hole size; though, for relative hole sizes larger than 0.52 the short wavelength edge stays fixed at 520 nm.

Hence, under the constraint that the ZDW must be close to 1064 nm

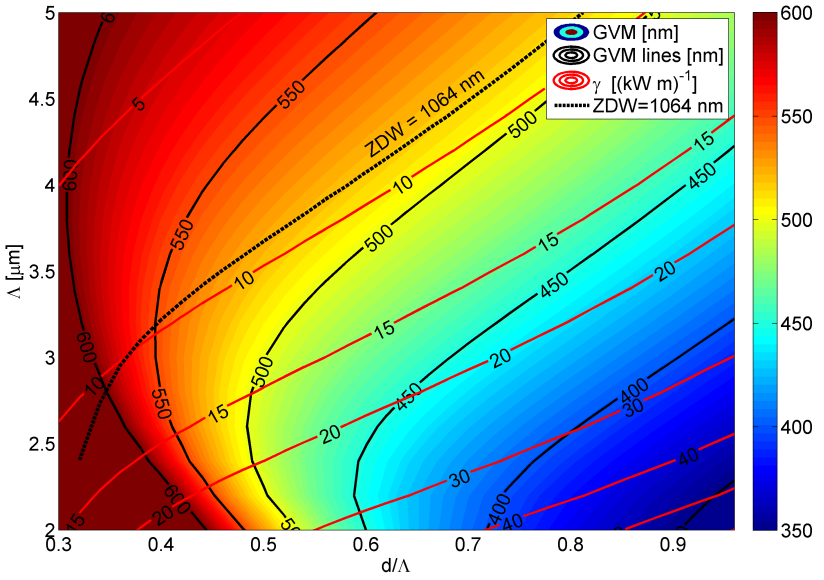

Figure 5.13: Optimization of pure silica PCFs. See the text for explanation.

the optimal relative hole size is about 0.5. Higher value of the relative hole size will not improve the magnitude of the nonlinear parameter nor the position of the short wavelength edge, but the fiber will tend to be multimode. A lower relative hole size means a slightly lower nonlinear parameter and a shift of the short wavelength edge towards the pump and in turns reduced SC bandwidth. Therefore, the investigated F10 fiber is close to being optimal and only minor improvements can be expected.

Besides optimizing the dispersion and nonlinear properties of pure silica PCFs another option is to dope the core material to improve the performance. This is the topic of the next section.

5.6.1 Increasing the nonlinearity

Silica fibers are commonly doped with materials such as Ge, F, B, Al, or rare earth elements. The advantages of doping the core of the PCF with Ge is to increase the confinement, the intrinsic nonlinearity, and the Raman fraction of the nonlinearity. The maximum doping density is limited by stresses in the glass and the difference in glass-transition temperature with respect to undoped silica, which can make fabrication challenging.

A series of PCFs with Ge-doped cores have been fabricated with the highest doping level available of 19%mol. The nonlinear parameter is thereby enhanced by a factor of 4-5 compared to undoped PCFs with similar GVD. The ZDW has been designed to be close to but shorter than the pump wavelength. The PCFs constitute the G-series and their properties are listed in Table 5.1.

In Fig. 5.14 SC spectra of the three Ge-doped PCFs in the G-series pumped by a gain-switched fiber laser are shown. In general the same spectral form and features are present as for pure silica PCFs. The buildup of solitons at the long wavelength edge is more apparent, which can be explained by the higher nonlinearity and an increased Raman cross section. A kink is present at 1380 nm due to the high OH-loss in the fibers, which causes the solitons to stop redshifting.

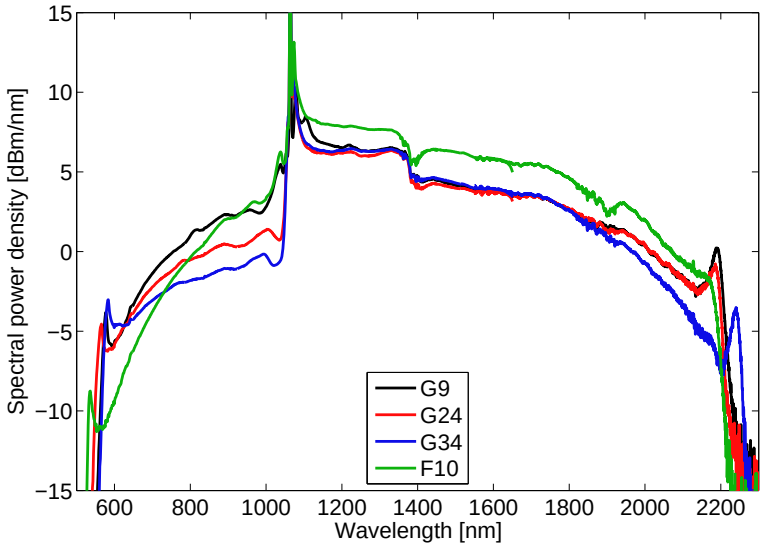

Figure 5.14: SC spectrum generated with 25 m of Ge-doped PCFs with decreasing ZDW pumped by a gain-switched fiber laser with 500 W coupled quasi-CW power. The coupled average power is 9 W. The fiber F10 is included for comparison.

It is worth noting that only 25 m of fiber length is necessary to fully develop the SC spectrum compared to 70-100 m in the pure silica PCF. Furthermore, a higher fraction of the total generated light is below the pump wavelength. This observation is quantified in Fig. 5.15 where the integrated spectral power density below 800 nm (P<800 nm) and the integrated spectral power density above 1250 nm (P>1250 nm) are shown as function of ZDW. The fibers used to obtain this data are pumped with 500 W peak power and 21 W average power.

The fractional power η is defined as the power in the integrated intervals divided by the total average output power. It can be seen that in Ge-doped fibers twice as much visible light is generated compared to that obtained from silica PCFs. The visible fraction is almost 4% for the G9 fiber (with ZDW of 1055 nm). In fact, the visible fraction of G9 is 240% higher than the visible fraction of F10 fiber, which basically has the same ZDW. The fraction of light beyond 1250 nm is slightly lower for the Ge-doped fibers due to higher fiber loss.

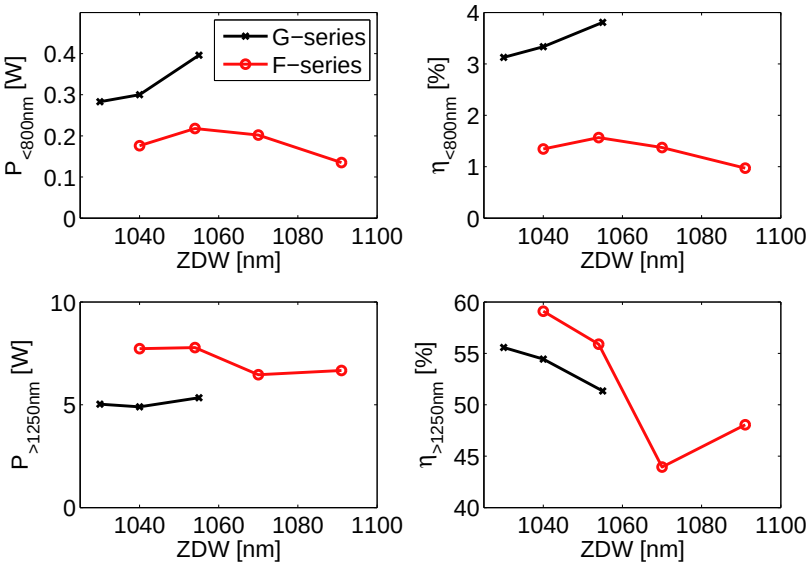

Figure 5.15: Integrated power of visible (P<800 nm) and infrared (P>1250 nm) light, and the fraction η of the integrated power of the total output power for the Ge-doped and pure PCFs with increasing ZDW. The fibers are pumped with 500 W peak power and 21 W average power with laser configuration A.

5.7 Summary

The physical processes involved in supercontinuum (SC) generation have been briefly reviewed. A numerical simulation is used to illustrate the typical broadening mechanisms in SC generation. It is concluded that numerical simulations of quasi-continuous wave (quasi-CW) SC is computationally heavy but is an excellent tool for visualization of the SC dynamics occurring in photonic crystal fiber (PCF).

Three series of PCFs are pumped with pulses from a GS fiber laser and the spectral properties of the resulting optical output are discussed.

An unprecedented coupled quasi-CW pump (peak) power of 500 W–600 W is used.

The dynamics that dominate quasi-CW pumped SC are found experimentally. The processes of modulation instability, soliton redshift, and trapping of dispersive waves by solitons are identified. The soliton collisions are found to be of utmost importance to explain the large observed bandwidths. It is shown that a weak and anomalous dispersion at the pump wavelength results in the flattest spectra.

At the highest quasi-CW pump power level the SC bandwidth variation is found to be less than 4%, hence the spectral bandwidth becomes quasi-independent of the zero dispersion wavelength in the examined range of 1030-1090 nm. This quasi-independence is due to the fact that the spectral bandwidth is limited by the high attenuation in silica at long wavelengths.

SC generation in commercial PCFs pumped by a fiber laser operating in the gain-switching regime and in CW mode is compared. The spectrum generated by the gain-switched pulse train spanned from 500 nm to 2250 nm, with a total output power of 12 W, and high infrared power spectral density above 5 dBm/nm (3.1 mW/nm) over a bandwidth of more than 1000 nm with 6 dB flatness. This spectrum is considerably broader than that obtained when CW-pumping the same fiber. When the separation of the pump wavelength from the zero dispersion wavelength is increased, only a negligible amount of visible light is generated.

Optimized PCFs for gain-switched fiber laser pumping are investigated. Using modeling of the transverse mode properties it is shown that the short wavelength edge and the nonlinear parameter cannot be optimized further for pure silica PCFs with a hexagonal cladding structure. A series of Ge-doped fibers are fabricated with a nonlinear parameter 4-5 times higher than pure silica PCFs. These doped fibers had a 240% higher efficiency of visible light generation than pure silica fibers with similar zero dispersion wavelength.

Chapter 6

Conclusion and outlook

In this thesis the feasibility of applying gain-switched all-fiber lasers to supercontinuum (SC) generation was investigated. The work was motivated by the simplicity of the architecture and the ability to scale the optical output power of such fiber lasers. By reducing the complexity and the cost of SC laser sources, applications within new areas can be enabled.

The physics of fiber lasers were reviewed to understand the mechanisms involved in gain-switching. A detailed numerical model was provided to visualize the different stages of pulse generation. The important coupling of spontaneous emission into the laser mode in the initial stage was described. The influence of the radial dependence, of the amplified spontaneous emission, and of varying input parameters on the output pulse peak power was examined. The agreement between the results of the model and the experiment was not adequate and a fitting parameter was needed. A simplified point model was also developed to derive an analytic expression for the relaxation oscillation period.

Extensive experiments with gain-switching of fiber lasers with a variety of different configurations such as active fiber type, fiber length, pump power, and pump wavelength were carried out. The dependencies of output peak power, pulse duration, spectral bandwidth, and scaling with repetition rate were thoroughly described. General guidelines were derived to enable designing of gain-switched fiber lasers with tailored properties. This implied that the peak power was found to vary linearly with absorbed pump power, and the pulse duration was found to be accurately described via the relaxation oscillation period derived by the simplified point model of fiber lasers.

The linear and nonlinear processes of SC generation were reviewed with focus on the quasi-continuous wave pumping regime. The dynam-

ics of SC generation were confirmed experimentally and the importance of the soliton collisions for the observed broadening was highlighted. Requirements for efficient and flat SC generation at the high quasi-continuous wave power levels were analyzed. A gain-switched fiber laser was shown to be a versatile pump for SC generation. Finally, an optimization of photonic crystal fibers for gain-switched fiber laser-pumped SC generation was presented.

6.1 Outlook

SC laser sources have numerous applications in areas, such as spectroscopy and microscopy due to the unique combination of extremely broad spectral bandwidths, high spectral power densities, and high spatial coherence. Interest is on reducing the complexity of the SC source to reduce the cost, improve reliability, and to improve the spectral power density in selected wavelength bands and thereby enable applications within new areas.

Using a gain-switched fiber laser, supercontinua were generated, which had higher average output powers and spectral power densities than commercially available short-pulsed SC laser sources. This can be seen in Fig. 6.1. Here, the spectral power density of the output of two optimized fibers are compared to the output of a high-power picosecond SC laser source. However, the spectral power density at visible wavelengths below 800 nm was lower for fibers pumped by a gain-switched fiber laser. An optimized Ge-doped fiber had higher spectral power density at shorter wavelengths than a pure silica fiber. Unfortunately, the relatively low peak power of pulses generated by gain-switching was not sufficient to excite much visible light.

The optical construction of a SC laser source based on a gain-switched fiber laser is considerably simpler than typical high-power picosecond pumped SC laser sources. This suggests that a SC laser source based on a gain-switched fiber laser can have a reduced price point and thereby open applications within new areas.

The work done in this PhD project has therefore shown that gain-switched all-fiber lasers are viable and cost-effective pump lasers for high-power invisible SC generation in photonic crystal fibers.

Gain-switched fiber laser can also be applied to applications other than SC sources, for instance in material processing where high pulse energies and average power levels are desirable. The design guidelines that are derived in this project are a valuable tool in the design process of gain-switched fiber lasers for such applications [120].

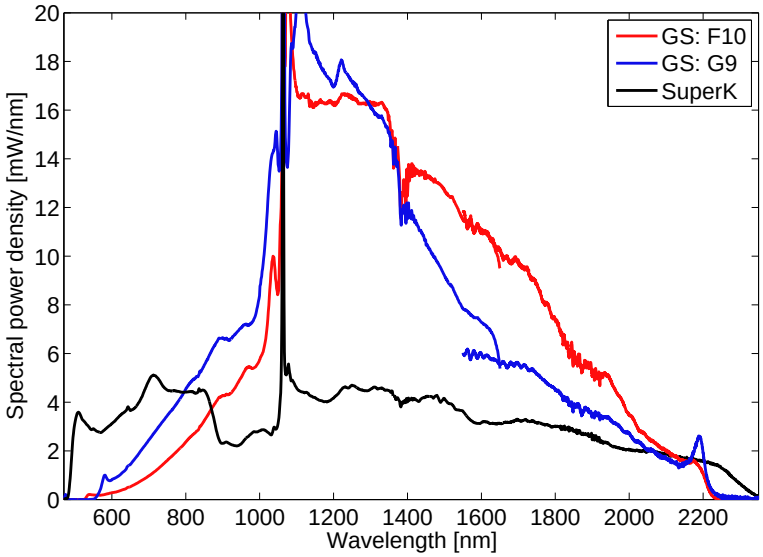

Figure 6.1: Output SC spectra of two optimized photonic crystal fibers (F10 and G9) pumped by the gain-switched fiber laser developed in the project. They are compared to the output spectra of a commercially available high-power picosecond SC laser source (SuperK EXR-15, NKT Photonics).

6.2 Future perspectives

The goals of this thesis have been accomplished but greater understanding can be obtained by putting more work in the same directions.

Three aspects of the modeling of gain-switching are highly relevant to examine further; What causes the discrepancies between the simulations and the experiments, how to thoroughly derive the relation $t_0 = \tau_R/\pi^2$, and what contributes to the experimentally determined constant $\underline{\beta}$.

It would be interesting to thoroughly investigate the influence of the reflectivity, center wavelength, and bandwidth of the low reflector fiber Bragg grating of the laser cavity on the peak power of the generated pulses. Based on the detailed numerical model, modest improvements were found in section 3.5.1, but an experimental verification of these tendencies is needed.

Alternatively, it would be interesting to combine passive Q-switching and gain-switching by including a section of a saturable absorber fiber in the cavity. This reduces the spontaneous emission level, which causes the pulse generation to be delayed, whereby the peak power is potentially increased.

Cascading of gain-switched fiber lasers has been used in Tm-doped

and Ho-doped fiber lasers [131]. However, it would be interesting to use a cladding-pumped gain-switched Yb-doped fiber laser at e.g. a wavelength of 1040 nm to core-pump a gain-switched Yb-doped fiber laser at a wavelength of 1064 nm. Theoretically, this would results in an increased peak power by almost an order of a magnitude. Alternatively, a gain-switched Yb-doped fiber laser can be used as a powerful pump for a core-pumped gain-switched Tm-doped fiber laser.

Regarding SC generation, it would be interesting to scale the qausi-CW power level to well above 1 kW by using a fiber amplifier to generate more visible light. The influence of the bandwidth of the pump laser on the SC spectrum has been examined at a low CW pump power [185], but it is not known if the same relations apply in the high-power regime and for a fully developed SC. In this project only an unpolarized pump laser was used, but the SC generation can possibly be improved by using a linearly polarized gain-switched fiber laser and a polarization maintaining nonlinear fiber.

Appendix A

Abbreviations

ASE – Amplified spontaneous emission

BPP – Beam parameter product

B90 – Bandwidth that contains 90% of the pulse energy

CW – Continuous wave

FBG – Fiber Bragg grating

FWHM – Full-width half-maximum

GNLSE – Generalized nonlinear Schrödinger equation

GVD – Group velocity dispersion

GVM – Group velocity matching

GS – Gain-switching

HR – High reflector

LR – Low reflector

MI – Modulation instability

NA – Numerical aperture

PCF – Photonic crystal fiber

SC – Supercontinuum

SPM – Self-phase modulation

Yb – Ytterbium (Rare-earth element)

V – V-parameter or normalized frequency

ZDW – Zero dispersion wavelength

Appendix B

Current fiber laser technology

In this appendix the concepts and technologies behind fiber lasers will be described with the aim of introducing a non-expert reader to the terminology and various practical aspects. It is therefore intended as a compact reference work. The reader is directed to Refs. [10, 11, 63] to obtain a more formal introduction to fiber lasers and amplifiers with focus on the history and future power scaling.

The components of a fiber laser are illustrated in Fig. B.1. Many different types of fiber lasers exist, but they all contain similar elements as found in the illustration. The purpose, the properties, and available

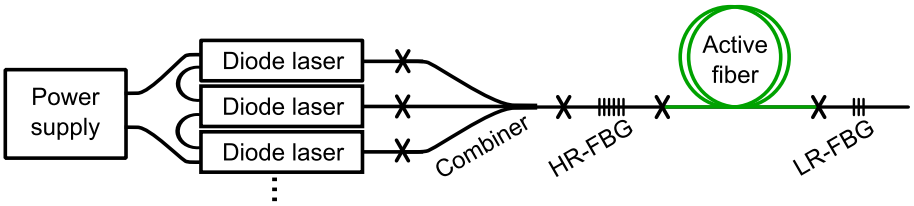

Figure B.1: The components of fiber lasers considered in this thesis. The '**X**'s mark fusion splices. HR-FBG and LR-FBG are the high and low reflector fiber Bragg grating, respectively.

technologies for each element will now be listed:

The power supply delivers a controlled current to the diode pump lasers, and is often also called a diode driver. Their properties, such as capacity, efficiency, and noise are selected depending on the application of the laser. When a fiber laser is set for GS operation, a power supply with a high modulation frequency and relatively high current capacity is required. Commercially available power supplies can deliver 60 A with a rise time of 90 ns. To obtain this

fast value a good impedance matching of the electronics in the power supply, the wires, and the diodes is required to minimize ringing effects.

Diode lasers act as the optical pump of the laser gain medium and has replaced older pumping technologies such as flash lamps; due to reliability, efficiency, and high brightness (or radiance defined as the power per area per solid angle). The diodes are fabricated by InGaAs semiconductor technology and are basically electrically pumped quantum wells formed in a cavity [225]. The maximum constant driving current can be up to 15 A (for a single emitter) and the electrical-to-optical efficiency for fiber-coupled pump diodes is typically higher than 60%. The spectral bandwidth is typically a few nanometers (FWHM) and the central wavelength can be varied from ∼800 nm–980 nm, where the most common wavelengths used for pumping fiber lasers and amplifiers are 915 nm and 976 nm determined by maxima of the absorption cross section of Yb-doped silica. The central wavelength shifts ∼0.33 nm/°C with heat sink temperature and ∼1.3 nm/A with the drawn current. This means that if the tolerances of the absorption band are tight, as in the case of 976 nm in Yb-doped silica, then the diode must be temperature controlled. Two types exist: single-mode diodes and highly multi-mode diodes. The output from the single mode diodes can be coupled directly into single-mode fiber, and their fiber coupled output power is limited to < 1 W by the intensity damage threshold of the diode facet. Multi-mode diodes can, on the other hand, deliver more than 10 W [226] into a highly multi-mode double clad fiber with core of 105 μm and a NA of between 0.12 or 0.22 (see section 2.1). In a single module/package the output from several diode lasers can also be combined (spatially and by polarization multiplexing) into the same fiber and thereby increasing the output power and brightness. Today's state-of-art modules are capable of delivering 140 W in a single multi-mode fiber [227]. The diode laser technology is very mature and expected lifetime at maximum operation conditions is more than 20 years. A single diode can for a time of <700 ns be driven by up to 50 A [226] resulting in 35 W of output power, but the lifetime is reduced considerably.

A combiner is a component that enables combining the output of several fiber coupled diode lasers into a single fiber. A combiner can be avoided if a single diode pump module is sufficient for the ap-

plication. Different concepts can be applied to their construction but the common aspect is that they are fabricated by processing of silica fibers, such as fusing of fiber bundles and tapering to reduce the fiber diameter [228]. A typical realization is constructed using 7 fibers with an outer diameter of 125 μm and NA of 0.15, fused together and tapered to an outer diameter 125 μm. The principle of brightness conservation [228] dictates that beam divergence increases as the area is reduced (analogue to the transform limit in time and frequency). The taper ratio typically introduces a shift in brightness of a factor of three, hence the NA at the output will be three times higher; $\sim$0.45. One of the input fibers can contain a single core in the double-clad configuration to enable feed through of e.g. a seed signal. The pump and signal loss in a combiner is usually $<$0.5dB equivalent to $<$10%.

Reflectors are required to form the laser cavity. Their free-space analogues are a high reflectivity mirror (HR) and a lower reflectivity mirror (LR) or output coupler at the output end. They are characterized by the reflectivity, the center wavelength, the bandwidth, and the imperfections such as side-lobe suppression. In fiber lasers so-called fiber Bragg gratings (FBGs) are mostly used due the stability and the all-fiber format. They are made by exposing a fiber with UV light with a regular longitudinal pattern e.g. made by a phase mask. This results in periodic formations of defects, which causes longitudinal modulation of the refractive index in the core that functions as a mirror for certain wavelength ranges. For fiber lasers the HR reflectivity is usually close to 100% and the LR reflectivity can be between 5–50%. Alternatively, the LR can be replaced with a cleaved fiber facet with as small angle as possible, whereby the silica-air interface will cause a $\sim$4% reflection.

The active fiber is the key component and is described in much more detail in section 2.1, which covers the fiber geometry, and in section 2.2, where the properties rare earth doped silica are described. The common pumping schemes are described in Appendix B.2.

Splices are made by heating two flat cleaved fiber facets until they soften at $\sim$ 2000°C and pressing them together in a controlled manner. In this way a mechanically strong and stable coupling is made, which can handle high temperature fluctuations and high optical powers. The loss can be made low by careful alignment of the fiber cores visually or by optimizing the transmitted power during splicing. A mismatch in the core diameter, misalignment of

the cores, or facet cleave angles larger than a few degrees generally result in an increased loss at the splice. In the fusing process the silica reaches such high temperature that diffusion of the core or cladding dopant becomes important. This can be used as an advantage e.g. when splicing a highly doped fiber with a small core to a less doped fiber with a larger core, because the core size mismatch is minimized by differential diffusion. When splicing PCFs, the temperature needs to be reduced to avoid collapse of the air holes due to surface tension. Low loss splicing is still possible, but a higher degree of control of the splicing temperature is needed. This can be done using a resistive filament made from Wolfram or graphite. More traditional heating methods are achieved via an RF-arc discharge or a CO_2 laser. Splices can be protected in a variety of methods, the most typical being casting the bare fiber in a polymer.

In addition to the component described above, common fiber coupled components are: isolators (light rectifier), power monitors, intensity or phase modulators, filters, and splitters. These components are mostly used in the low power <1 W regime, whereas the thoroughly described components are commercially available with power handling capacity of >1 kW.

B.1 Fiber laser output properties

The properties of output from fiber lasers are in some cases different from that of other lasers. Therefore, the properties, methods by which to measure them, and aspects relevant for gain-switching are listed in the following:

Output power is measured in Watts with a calibrated thermal or semiconductor-type power sensor. For fiber lasers the power typically scales linearly with diode pump current. Calibration of power meters is required but a variation in the measured power in the range of ±5% is usually found. The measured power can depend on the wavelength of the light depending on the type of sensor used, but most meters are programmed to take this effect into account. Power scaling of fiber lasers has been quite aggressive in the last decade, and fiber lasers with >2 kW single-mode output and 50 kW multi-mode output are currently commercially available [229].

Temporal dynamics generally refer to either pulsed or CW modes of operation of a fiber laser. Short pulses (<10 ps) can be measured by an autocorrelator or a similar technique, whereas longer pulses can be measured directly via a fast photodiode (up to 1 GHz) and oscilloscope. If a CW laser has more than two longitudinal modes without a phase relation between them, the output will vary in time as mode beating occur and overall output power on very short time scales will behave chaotic. The term 'continuous wave' should therefore be understood to describe a laser that is not intentionally pulsed and has an output power that is rather stable on a time scale of milliseconds. The fiber lasers in the project all have lengths of a few meters and bandwidths of ∼1 nm, hence 10^4 longitudinal modes[1] are excited. The characteristic time of the beatings is called the coherence time, which is inversely proportional to the bandwidth [185,186]. For a bandwidth of 1 nm the coherence time is about 5 ps [186]. The beatings result in enhancement of the instantaneous power (peak power) in a short time duration, and for a bandwidth of 1 nm the instantaneous power is up to 7 times the average power [186]. This effect is important in interpretation of the results from qausi-CW SC generation experiments.

Mode quality is of crucial importance for many applications, such as telecommunications and SC generation, where the light needs to be coupled to single mode fibers or focused to the smallest spot size possible. It is defined within the so-called beam parameter product (BPP), which is the product of the beam radius at the waist (w_0) and the beam divergence in the far field (θ). A beam with a Gaussian spatial profile is diffraction limited, and therefore is the ideal distribution and has a BPP of $\lambda/\pi = 0.34$ mm mrad at 1064 nm [63]. A non-ideal mode quality is quantified as $M^2 = \theta w_0/\mathrm{BPP} > 1$. The M^2 factor is measured by focusing the beam with a lens such that a suitable size beam waist is formed and measuring the beam profile through the focus point to obtain sufficient data to precisely determine both the waist size and location as well as the far-field divergence.

Spectral properties are measured with a spectrometer (linear photodiode array) or an optical spectrum analyzer (typically a rotating grating, a slit, and a detector). The spectral properties are closely

[1]The mode spacing is $c_0/(2nL)$, where n is the refractive index and L the cavity length. The number of modes is the bandwidth (in frequency) divided by the mode spacing.

related to the temporal dynamics for short pulses due to the transform relationship. The central wavelength, bandwidth and the spectral shape are typically analyzed, which are good indicators of the quality of the gratings used to build the cavity and the output. Spectral broadening due to nonlinear effects such as stimulated Raman scattering and self-phase modulation (see section 5.1) can be identified and are commonly found.

Quantum efficiency is defined as the $\eta_Q = \lambda_{pump}/\lambda_{signal}$, where λ_{pump} is the mean wavelength of the pump and λ_{signal} is the signal wavelength. This factor is important in that, in order for a quasi-four level laser transition to occur (see section 2.2), the pump photon energy must be higher than the signal photon energy. For Yb-doped fiber the value is typically between 86% and 95%, which is very low compared to most other laser media. The upper limit in the efficiency of the laser is set by this value. The energy that is not converted is dissipated as heat (phonons).

Slope efficiency is defined as the linear slope of the output power versus the available *or* incident *or* absorbed pump power. The laser threshold of Yb-lasers is <1 W of pump power, which means that in many cases the threshold can be neglected. For high performance lasers the slope efficiency is 1-5% lower than the quantum efficiency, where the additional losses can be explained by splicing losses, scattering loss in the fibers, and an imperfect HR grating. When considering the absorbed slope efficiency the output power is divided by absorbed pump power (the coupled pump power minus the unabsorbed pump at the output).

Optical-to-optical efficiency is defined as the optical output power of the laser divided by the optical output power of the pump diodes at a given diode current. It is a few to tens of percent less than the slope efficiency depending on the pump power because it incorporates the lasing threshold.

Polarization or the polarization state of the optical output of a fiber is either linearly, elliptically, or randomly polarized. The degree of polarization of an emitted beam can be measured at the output by analyzing the output with a polarizer (birefringent element), either by rotating the beam polarization or the polarizer about the axis of propagation. The ratio of the highest transmitted power divided by the lowest transmitted power is a good approximation to the polarization extinction ratio, which is often converted to

decibels. For fibers, good linearly polarized output has a polarization extinction ratio between 16-20 dB. Higher values can in general be produced in solid state lasers.

Figure B.2: High power fiber lasers are hazardous to the skin and especially the eyes. Remember to wear appropriate protection at all times and minimize the risk of accidents. Source: www.electricstuff.co.uk

B.2 Core and cladding pumping

Active fibers can, depending on the application, be designed to be core pumped or cladding pumped. In Fig. B.3 the two pumping schemes of fiber lasers are illustrated.

The pump source is generally either diode lasers or other fiber lasers. Fiber lasers are used as pumps e.g. when the desired pump wavelength is not accessible with diode lasers, or a low pump beam NA, a short pump pulse duration, or a high peak pump power are needed. The complexity and cost of the complete fiber laser increases in this case. Diode lasers have a moderate beam quality, relatively narrow bandwidth, high electrical-to-optical efficiency, and the price per Watt is lower than for a fiber laser. Diode laser technology has matured to the point that they are easily packed and fiber coupled, which makes them robust and reliable. The pump diode laser technology is described in detail in Appendix B.

In the lower part of Fig. B.3 the pump intensity is illustrated as function of the length of the active fiber for the two pumping schemes.

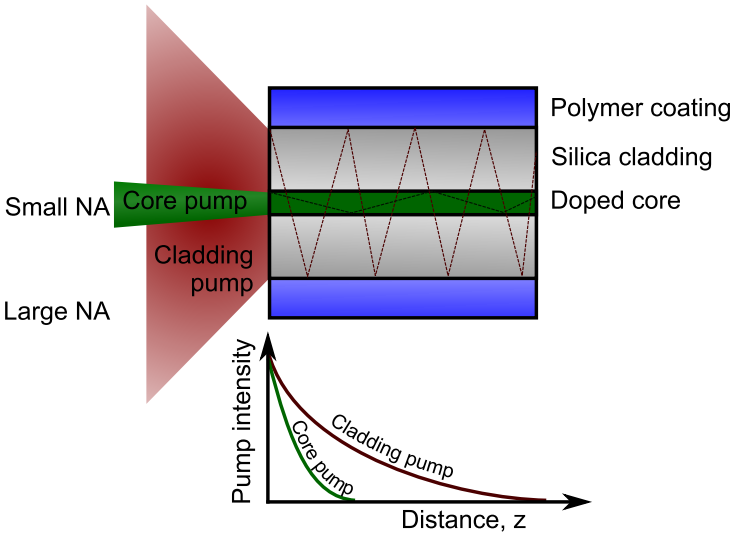

Figure B.3: Difference in the core and the cladding pumping schemes. The lower part shows the pump intensity as function of distance in the active fiber.

The pump absorption efficiency $\eta_{\text{abs}}(L_{Yb})$ is defined by

$$\begin{aligned} \eta_{\text{abs}}(L_{\text{Yb}}) &= \frac{I(0) - I(L_{Yb})}{I(0)} \\ &= 1 - \exp\left\{-L_{\text{Yb}}\sigma_a(\lambda_p)N_1\frac{\Gamma A}{A_{\text{pump}}}\right\} \qquad \text{(B.1)} \\ &= 1 - \exp\left\{-0.23 L_{Yb}\alpha_{dB}(\lambda_p)\right\}, \qquad \text{(B.2)} \end{aligned}$$

where $I(z)$ is the pump intensity, L_{Yb} the active fiber length, λ_p the wavelength of the pump, Γ the effective overlap of the transverse mode area of the core and the Yb-doped area A, and A_{pump} is the area of the mode(s) of the pump. When the laser medium is excited, the upper state density N_2 is populated and density of ground state N_1 is reduced, hence $N_1 = N_0 - N_2$, where N_0 is the ion concentration. The pump is said to be unsaturated, where it applies that $N_2/N_0 \to 0$ and $N_1 \approx N_0$. A given active fiber is therefore characterized by a the pump absorption coefficient $\alpha_{dB}(\lambda_p)$ in unit of dB/m ($N_1 = N_0$ is assumed).

A typical pump absorption efficiency η_{abs} of a fiber laser is designed to be 13 dB–20 dB (95%–99%). Absorbing the last fraction is inconvenient because, for large values of the $L_{Yb}\alpha_{dB}$, the absorption efficiency increases slowly and a large length is needed. Note that if the absorption cross section is doubled, the fiber length can be reduced by half while maintain the same pump absorption efficiency. Increasing A increases

the number ions per length (at fixed doping concentration) and reducing A_{pump} increases the overlap between the pump and the doped area, and hence the absorption coefficient is increased.

In core pumping the beam quality of the pump laser must be high to match the low NA of the core and the spot diameter must match the area of the core. For these reasons single-mode pump lasers must be used. In core pumping the overlap of the pump light and the core is high due to $A_{\text{pump}} \approx \Gamma A$. The pump absorption efficiency coefficient is typically more than 100 dB/m [66], hence the pump light is typically absorbed over a short active fiber length of centimeters. This causes a high upper state density and pump saturation is often present in core-pumping. When the pump power exceeds tens of Watts, the generated heat per centimeter is high and problems with heat dissipation occurs [112]. To overcome the power limitations the cladding pumping geometry can be applied.

In the double clad fibers the pump waveguide has much higher NA and core area, and can therefore collect more light and the beam quality of the pump can be reduced. This opens the possibility of using cost-effective and high power multi-mode diode lasers [10]. The pump light still has overlap with the doped area but the absorption coefficient is much smaller than in core pumping. Typical cladding pump absorption is less than 10 dB/m [66], which means that the cavity length should be a few meters to maintain a sufficient absorption of the pump. This has the advantage that the heat load is distributed over a large length (surface area). Up to a kilowatt per meter of extracted power has been demonstrated corresponding to hundreds of Watt of generated heat per meter [10].

Appendix C

Implementation of the detailed model

The numerical scheme applied is chosen such that the level of approximations is low in order to keep the results as general as possible. The fibers used in the project have a nearly symmetric core hence the angular dependence in the radial coordinate is small and can be neglected. The fiber is therefore split into a number of concentric tubes and the length is discretized. The optical power spectrum is divided into a number of bins with a specific bandwidth. Both forward and backward propagating powers are simulated. The transverse mode is found by a radial mode solver. The transverse field of the pump is assumed to be uniformly distributed over the cladding area. The pump and signal are simulated to travel in both forward and backward directions. It is a boundary value problem, and the following boundary conditions are used:

$$p_\omega^+(L_{\text{pump}}) = p_\omega^{+\text{pump}}(t) \tag{C.1}$$
$$p_\omega^-(L_{\text{pump}}) = p_\omega^{-\text{pump}}(t) \tag{C.2}$$
$$p_\omega^+(L_{HR}) = R_{H,\omega} p_\omega^-(L_{HR}) \tag{C.3}$$
$$p_\omega^+(L_{LR}^+) = (1 - R_{L,\omega}) p_\omega^+(L_{LR}^-) \tag{C.4}$$
$$p_\omega^-(L_{LR}) = R_{L,\omega} p_\omega^+(L_{LR}), \tag{C.5}$$

where $p_\omega^{\pm\text{pump}}(t)$ is the forward and backward propagating pump power at the position L_{pump}, $R_{H,\omega}$ is the reflectance of the high reflector, and $R_{L,\omega}$ is the reflectance of the low reflector. The temporal and spatial derivatives are discretized using simple forward and backward difference approximations. The forward difference scheme is defined as

$$\left.\frac{\partial u}{\partial x}\right|_i = \frac{u_{i+1} - u_i}{\Delta x}, \tag{C.6}$$

where $u_i = u(x_i, t)$. Furthermore, the so-called Courant number Q, which relates the temporal and spatial time step, is defined as

$$Q = \frac{\delta t}{\delta z \sqrt{\epsilon \mu_0}} = \frac{c_0 \delta t}{n \delta z}. \tag{C.7}$$

It can be seen that $Q \leq 1$ to avoid numerical artifacts.

The implementation is quite lengthy (300 lines) in order to have a high level of flexibility, so only the core lines of the implementation will be shown. To read the presented code only fundamental knowledge of the Matlab programming language is required. The symbols follow the convention in the derivation closely and are therefore not separately listed here. Each element of the code has been validated by means of known steady state and dynamic solutions. This code and some examples are made publicly available on www.muder.dk/GS.

```
%% Finite difference simulation of fiber laser, 2013 C. Larsen
h = length/nz;  % length step size, total length/number of z's
dt = Q*h*n0/c0; % temporal step size
% p(nz,nlam) is forward propagating power at wavelength (lam)
% q(nz,nlam) is backward propagating power
for j = 1:nt    % loop nt times to propagate equations
    K = zeros(nz,nr); G = zeros(nz,nlams); S = zeros(nz,nlams);
    % add pump (P) to forward prop. power at pump.zi
    p(pump.zi,pump.nlam) = p(pump.zi,pump.nlam) + Q * pump.P;
    % implement grating at fbg.zi
    p(fbg.zi+1,fbg.nlam) = fbg.tm/Q * p(fbg.zi,fbg.nlam) ...
                         + (1-fbg.tm)/Q * q(fbg.zi+1,fbg.nlam);
    p(fbg.zi,fbg.nlam) = 0;
    % update population
    for l = 1:nlams % integrate over all wavelengths
      K = K + lam(l)*(siga(l)-(siga(l)+sige(l))*n2)...
          .* ((p(:,l)+q(:,l))*psi(l,:));
    end
    n2 = (n2.*(1 - dt/tau2) + dt/(h0*c0)*K);
    % update gain
    for k = 1:nr % integrate over the radial direction
      G = G + (n2(:,k)*(siga+sige) - ones(nz,1)*siga)...
          .* (ones(nz,1)*psi(:,k)') *k;
    end
    % update spontaneous emission
    Sl = 2*pi*N0*2*h0*c0^2*sige./(pi*Dc^2/4*lam.^3).*dlam;
    for k = 1:nr % integrate over the radial direction
      S = S + n2(:,k)*Sl*k;
    end
    % update forward propagation for all wavelengths
    p(2:nz,:)=p(2:nz,:).*(1-Q+Q*h*(-alpha+2*pi*N0.*dr^2*G(2:nz,:)))...
            + Q*p(1:nz-1,:) + Q*h*dr^2*S(2:nz,:);
end
```

Appendix D

The laser cavity

In this appendix the characteristic times of a laser cavity are derived. A cavity is made of two mirrors with a certain separation called the cavity length. The time it takes of a photon to propagate from one mirror to the other and back again is called the round trip time τ_{rt} and is given by [230]

$$\tau_{rt} = \frac{2nL}{c_0}, \tag{D.1}$$

where L is the cavity length, c_0 is the speed of light, and n is the refractive index. For a passive linear cavity with mirror reflectivities R_1 and R_2, and a loss per fiber length α, the intensity $I(t)$ at a fixed position after a single round trip is given by

$$I(\tau_{rt}) = I(0)R_1R_2(1-\alpha L)^2. \tag{D.2}$$

The intensity at a fixed position at the time of the m'th round trip ($t = mt_{rt}$) defines the photon lifetime in the cavity, τ_c, as

$$I(m\tau_{rt}) = I(0)e^{-m\tau_{rt}/\tau_c} = I(0)\{R_1R_2(1-\alpha L)^2\}^m, \tag{D.3}$$

and thus τ_c is

$$\tau_c = -\frac{\tau_{rt}}{\ln\{R_1R_2(1-\alpha L)^2\}} \tag{D.4}$$

Typical values for a fiber laser with fiber Bragg gratings are $R_1 = 1$, $R_2 = 0.15$, and $\alpha L \approx 0$ and the photon lifetime is then $\sim nL/c_0$. The pulse duration of pulses produced by gain-switching is affected by the round trip time and by reducing the fiber length L the pulse duration can be minimized.

Appendix **E**

Chromatic material dispersion

In this appendix the chromatic material dispersion is discussed by using the classical model of a driven and damped harmonic oscillator. The material dispersion of silica is represented by Sellmeier polynomials.

The classical, driven, damped, harmonic oscillator is found to describe absorption and dispersion well. By the Newton second law the equation of motion of a (quasi-particle) charge carrier is described by

$$\frac{\partial^2 x(t)}{\partial t^2} + \gamma' \frac{\partial x(t)}{\partial t} + \omega_r^2 x(t) + \frac{e}{m^*} E(t) = 0, \tag{E.1}$$

where $x(t)$ is displacement of charge carrier density from equilibrium, m^* the effective mass, γ' damping rate, $\omega_r^2 = k/m^*$ the resonance frequency, e electron elementary charge, $E(t)$ the applied electric field. The solution to this is called the Lorentz model, and the Drude model is derived by setting the resonance frequency to zero. Due to the linearity the response terms are additive.

The harmonic solution to equation E.1 can be found by an electric field of $E(t) = \Re\{E_\omega \exp(-i\omega t)\}$ and assuming that the solution to the displacement has the same time dependence, $x(t) = \Re\{x_\omega \exp(-i\omega t)\}$;

$$x_\omega \exp(-i\omega t) \left\{-\omega^2 - i\omega\gamma' + \omega_r^2\right\} + \frac{e}{m^*} E_\omega \exp(-i\omega t) = 0 \tag{E.2}$$

$$x_\omega \left\{-\omega^2 - i\omega\gamma' + \omega_r^2\right\} + \frac{e}{m^*} E_\omega = 0 \tag{E.3}$$

Note, that the chosen sign of the exponential defines the complex refractive index, hence $n = n_{re} + ik$. The linear susceptibility $\chi_p^{(1)}$ of term p can now be found as

$$\chi_p^{(1)} = \frac{P_p(\omega)}{\epsilon_0 E(\omega)} \tag{E.4}$$

where $P_p(\omega) = -eN_p x_p(\omega)$ is the induced polarization given by the electronic charge, the density of oscillators N, and the displacement. Combining equation E.3 and E.4 gives

$$\chi_p^{(1)} = \frac{-eN_p x_{\omega p}}{E_\omega} = \frac{\omega_{pp}^2}{\omega_{0p}^2 - \omega^2 - i\omega\gamma_p'}, \tag{E.5}$$

introducing the plasma frequency $\omega_{pp}^2 = \frac{N_p e^2}{\epsilon_0 m_p^*}$ for pole p. The complex refractive index of a material consisting of several Lorentz terms is then given by,

$$\epsilon_r = n^2 = 1 + \sum_p^N \chi_p^{(1)} = 1 + \sum_p^N \frac{\omega_{pp}^2}{\omega_{0p}^2 - \omega^2 - i\omega\gamma_p'} \tag{E.6}$$

The dispersion is defined [12]

$$D = \frac{dv_g^{-1}}{d\lambda} = -\frac{\lambda^2}{c_0}\frac{d^2 n}{d\lambda^2}, \tag{E.7}$$

where v_g is the group velocity. Alternatively, the propagation constant $\beta = n\omega/c = nk$ can be expanded in a power series, which coefficients are defined

$$\beta_j = \frac{d^j \beta(\omega)}{d\omega^j}|_{\omega=\omega_0}, \tag{E.8}$$

where ω_0 is the reference angular frequency.

In Fig. E.1 the real and imaginary components of the relative permittivity is shown for three resonances. In the lower section the refractive index and the dispersion is calculated. At resonance the radiation can be dissipated and transformed into heat. The resonances imply variation with frequency of the real part of the permittivity and hence the refractive index, which can be described through Kramer-Koning relation. Normal dispersion means increase of permittivity/refractive index with frequency, anomalous dispersion is the reverse. It can be seen that in between two resonances the dispersion crosses zero.

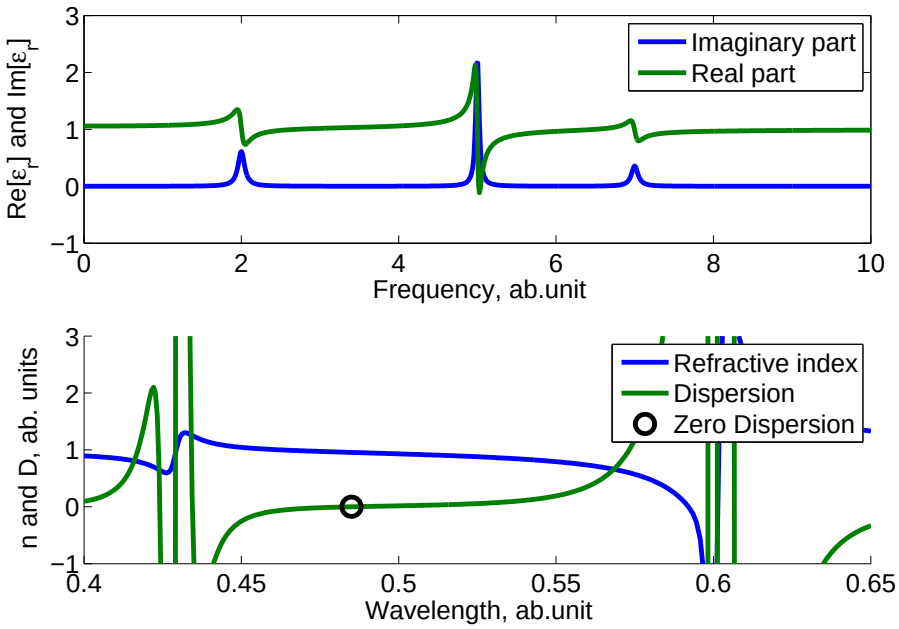

Figure E.1: Dispersion of an artificial material with resonances at frequencies of 2, 5, and 7 with varying strength and linewidth. In the bottom part the refractive index and the dispersion is seen as function of wavelength. A zero dispersion wavelength is found at 0.485 in between the two resonances.

E.1 The Sellmeier polynomial for silica

The common way of expressing the dispersion of a material is by the so-called Sellmeier polynomial given on the form

$$n(\lambda) = \sqrt{1 + \sum_{i=1}^{N} \frac{\lambda^2 a_i}{\lambda^2 - b_i}}, \tag{E.9}$$

where the parameters a_i and b_i are given by fits to experimental data. The values used for pure silica in the project are: [231]

```
a1 = 0.6965325; a2 = 0.4083099; a3 = 0.8968766;
b1 = 4.368309e-3; b2 = 1.394999e-2; b3 = 9.793399e1,
```

where λ is in μm. A high Germanium concentration in the core changes the refractive index and the Sellmeier polynomial must be modified as

$$n(\lambda) = \sqrt{1 + \sum_{i=1}^{N} \frac{\lambda^2 (a_i + x(c_i - a_i))}{\lambda^2 - (b_i - x(d_i - b_i))^2}}, \tag{E.10}$$

where the mole fraction of Germanium is x, and the parameters are [232];

```
a1 = 0.69616630; a2 = 0.40794260; a3 = 0.89747940;
b1 = 0.06840430; b2 = 0.11624140; b3 = 9.8961610;
c1 = 0.80686642; c2 = 0.71815848; c3 = 0.85416831;
d1 = 0.068972606; d2 = 0.15396605; d3 = 11.841931;
```

The Sellmeier parameters for 1% and 2% fluorine doped silica are [233]

```
a1 = 0.69325; a2 = 0.39720; a3 = 0.86008;
b1 = 0.06724; b2 = 0.11714; b3 = 9.7761;

a1 = 0.67744; a2 = 0.40101; a3 = 0.87193;
b1 = 0.06135; b2 = 0.12030; b3 = 9.8563;
```

Bibliography

[1] A. Schawlow and C. Townes, "Infrared and optical masers," Physical Review **112** (1958).

[2] T. Maiman, "Stimulated optical radiation in ruby," Nature **4736**, 493–494 (1960).

[3] P. Franken and A. Hill, "Generation of optical harmonics," Physical Review Letters **7**, 118–119 (1961).

[4] R. Boyd, *Nonlinear optics* (Academic Press, 2002).

[5] K. Kao and G. Hockham, "Dielectric-fibre surface waveguides for optical frequencies," IEEE pp. 1151–1158 (1966).

[6] S. E. Miller, E. A. J. Marcatili, and T. Li, "Part I: The Transmission Medium," IEEE (1973).

[7] E. Snitzer, "Optical Maser Action of Nd+3 in a Barium Crown Glass," Physical Review Letters **7**, 444–446 (1961).

[8] C. J. Koester and E. Snitzer, "Amplification in a Fiber Laser," Applied Optics **3**, 1182 (1964).

[9] Nobel, "http://www.nobelprize.org/ nobelprizes/ physics/ laureates/ 2009/ popular-physicsprize2009.pdf," Webpage **October 29** (2013).

[10] D. J. Richardson, J. Nilsson, and W. A. Clarkson, "High power fiber lasers: current status and future perspectives [Invited]," Journal of the Optical Society of America B **27**, B63 (2010).

[11] A. Tünnermann, T. Schreiber, and J. Limpert, "Fiber lasers and amplifiers: an ultrafast performance evolution." Applied Optics **49**, F71–8 (2010).

[12] G. Agrawal, *Nonlinear fiber optics* (Elsevier Inc., 2007).

[13] J. M. Dudley and S. Coen, "Supercontinuum generation in photonic crystal fiber," Reviews of Modern Physics **78**, 1135–1184 (2006).

[14] J. M. Dudley and J. R. Taylor, *Supercontinuum Generation in Optical Fibers* (Cambridge, 2010).

[15] J. Knight, T. Birks, P. Russell, and D. Atkin, "All-silica single-mode optical fiber with photonic crystal cladding," Optics letters **22**, 484–5 (1996).

[16] J. K. Ranka, R. S. Windeler, and A. J. Stentz, "Optical properties of high-delta air silica microstructure optical fibers." Optics Letters **25**, 796–8 (2000).

[17] H. Imam, "Broad as a lamp, bright as a laser," Nature Photonics **2**, 26–28 (2008).

[18] N. Savage, "Supercontinuum sources," Nature Photonics **3**, 114–115 (2009).

[19] Y. Sun, C. F. Booker, S. Kumari, R. N. Day, M. Davidson, and A. Periasamy, "Characterization of an orange acceptor fluorescent protein for sensitized spectral fluorescence resonance energy transfer microscopy using a white-light laser." Journal of biomedical optics **14**, 054009 (2009).

[20] E. Auksorius, "Multidimensional Fluorescence Imaging and Super-resolution Exploiting Ultrafast Laser and Supercontinuum Technology," Ph.D. thesis, Imperial College London (2008).

[21] A. Tycho, "Optical Coherence Tomography: Monte Carlo Simulation and Improvement by Optical Amplificatio," Ph.D. thesis, DTU (2002).

[22] D. T. Miller, O. P. Kocaoglu, Q. Wang, and S. Lee, "Adaptive optics and the eye (super resolution OCT)." Eye **25**, 321–30 (2011).

[23] S. Ishida, N. Nishizawa, T. Ohta, and K. Itoh, "Ultrahigh-Resolution Optical Coherence Tomography in 1.7 um Region with Fiber Laser Supercontinuum in Low-Water-Absorption Samples," Applied Physics Express **4**, 052501 (2011).

[24] J. Yi, Q. Wei, W. Liu, V. Backman, and H. F. Zhang, "Visible-light optical coherence tomography for retinal oximetry." Optics Letters **38**, 1796–8 (2013).

[25] C. Lee, S. Han, S. Kim, M. Jeon, M. Jeon, C. Kim, and J. Kim, "Dual-modal photoacoustic and optical coherence tomography using a single near-infrared supercontinuum laser source," SPIE **8581** (2013).

[26] L. V. Wang and S. Hu, "Photoacoustic tomography: in vivo imaging from organelles to organs." Science **335**, 1458–62 (2012).

[27] A. McCarthy, X. Ren, and A. D. Frera, "Kilometer-range depth imaging at 1550 nm wavelength using an InGaAs/InP single-photon avalanche diode detector," Optics Express **21**, 6241–6251 (2013).

[28] Y. Chen, E. Räikkönen, S. Kaasalainen, J. Suomalainen, T. Hakala, J. Hyyppä, and R. Chen, "Two-channel hyperspectral LiDAR with a supercontinuum laser source." Sensors **10**, 7057–66 (2010).

[29] J. Y. Lee and D. Y. Kim, "Versatile chromatic dispersion measurement of a single mode fiber using spectral white light interferometry." Optics Express **14**, 11608–15 (2006).

[30] P. Hlubina, M. Kadulová, and P. Mergo, "Chromatic dispersion measurement of holey fibres using a supercontinuum source and a dispersion balanced interferometer," Optics and Lasers in Engineering **51**, 421–425 (2013).

[31] A. De Angelis, A. Labruyère, V. Couderc, P. Leproux, A. Tonello, H. Segawa, M. Okuno, H. Kano, D. Arnaud-Cormos, P. Lévèque, and H.-o. Hamaguchi, "Time-frequency resolved analysis of a nanosecond supercontinuum source dedicated to multiplex CARS application." Optics Express **20**, 29705–16 (2012).

[32] P. Klarskov, A. Isomäki, K. P. Hansen, and P. E. Andersen, "Supercontinuum generation for coherent anti-Stokes Raman scattering microscopy with photonic crystal fibers." Optics Express **19**, 26672–83 (2011).

[33] NKTPhotonics, "http://www.nktphotonics.com," Webpage **October** (2013).

[34] Fianium, "http://fianium.com/," Webpage **October** (2013).

[35] Leukos, "http://www.leukos-systems.com/," Webpage **October** (2013).

[36] PolarOnyx, "http://www.polaronyxlaser.com/," Webpage **October** (2013).

[37] YSLPhotonics, "http://www.yslphotonics.com/en/," Webpage **October** (2013).

[38] S. T. Sørensen, "Deep-blue supercontinuum light sources based on tapered photonic crystal fibres," Ph.D. thesis, DTU (2013).

[39] J. C. Travers, "Blue extension of optical fibre supercontinuum generation," Journal of Optics **12**, 113001 (2010).

[40] J. Stone and J. Knight, "From zero dispersion to group index matching: How tapering fibers offers the best of both worlds for visible supercontinuum generation," Optical Fiber Technology **18**, 315–321 (2012).

[41] C. Xia, Z. Xu, M. N. Islam, F. L. Terry, S. Member, M. J. Freeman, A. Zakel, and J. Mauricio, "10.5W Time-Averaged Power Mid-IR Supercontinuum Generation Extending Beyond 4 um With Direct Pulse Pattern Modulation," IEEE Journal of Selected Topics in Quantum Electronics **15**, 422–434 (2009).

[42] C. Agger, "Infrared Supercontinuum Generation in Soft-glass Fibers," Ph.D. thesis, DTU (2012).

[43] C. Agger, I. Kubat, U. Møller, P. M. Moselund, C. Petersen, B. Napier, A. Seddon, S. Sujecki, T. Benson, M. Farries, J. Ward, S. Lamrini, K. Scholle, P. Fuhrberg, and O. Bang, "Numerical demonstration of 3-12um supercontinuum generation in large-core step-index chalcogenide fibers pumped at 4.5um," Nonlinear Optics p. NW4A.09 (2013).

[44] J. Swiderski, M. Michalska, and G. Maze, "Mid-IR supercontinuum generation in a ZBLAN fiber pumped by a gain-switched mode-locked Tm-doped fiber laser and amplifier system." Optics Express **21**, 7851–7 (2013).

[45] K. K. Chen, S.-U. Alam, J. H. V. Price, J. R. Hayes, D. Lin, A. Malinowski, C. Codemard, D. Ghosh, M. Pal, S. K. Bhadra, and D. J. Richardson, "Picosecond fiber MOPA pumped supercontinuum source with 39 W output power." Optics Express **18**, 5426–32 (2010).

[46] J. M. Stone, W. J. Wadsworth, and J. C. Knight, "1064 nm laser-induced defects in pure SiO2 fibers." Optics letters **38**, 2717–9 (2013).

[47] R. Song, J. Hou, Y.-B. Wang, T. Liu, and Q.-S. Lu, "Analysis of the scalability of single-mode near-infrared supercontinuum to high average power," Journal of Optics **15**, 035203 (2013).

[48] J. C. Travers, A. B. Rulkov, B. A. Cumberland, S. V. Popov, and J. R. Taylor, "Visible supercontinuum generation in photonic crystal fibers with a 400 W continuous wave fiber laser." Optics Express **16**, 14435–47 (2008).

[49] B. A. Cumberland, J. C. Travers, S. V. Popov, and J. R. Taylor, "29 W High power CW supercontinuum source." Optics Express **16**, 5954–62 (2008).

[50] A. Kudlinski, G. Bouwmans, O. Vanvincq, Y. Quiquempois, A. Le Rouge, L. Bigot, G. Mélin, and A. Mussot, "White-light cw-pumped supercontinuum generation in highly GeO(2)-doped-core photonic crystal fibers." Optics Letters **34**, 3631–3 (2009).

[51] L. Zenteno, E. Snitzer, and H. Po, "Gain switching of a Nd+3-doped fiber laser," Optics Letters **14**, 671–673 (1989).

[52] C. Larsen, K. P. Hansen, K. E. Mattsson, and O. Bang, "The all-fiber cladding-pumped Yb-doped gain-switched laser," Optics Express **22**, 1490–1499 (2014).

[53] K. P. Hansen, C. B. Olausson, J. Broeng, D. Noordegraaf, M. D. Maack, T. T. Alkeskjold, M. Laurila, T. Nikolajsen, P. M. W. Skovgaard, M. H. Sørensen, M. Denninger, C. Jakobsen, and H. R. Simonsen, "Airclad fiber laser technology," Optical Engineering **50**, 111609 (2011).

[54] A. Bjarklev, J. Broeng, and A. S. Bjarklev, *Photonic crystal fibres* (Springer, 2003).

[55] P. Russell, "Photonic crystal fibers." Science **299**, 358–62 (2003).

[56] P. Kaiser, "A new optical fiber," Bell System Technical Journal **52**, 265–269 (1973).

[57] P. Kaiser, "Drawing-induced coloration in vitreous silica fibers," Journal of the Optical Society of America **64**, 475 (1974).

[58] P. S. Russell, "Photonic crystal fibers," Journal of Lightwave Technology **24**, 4729–4749 (2003).

[59] T. A. Birks, J. C. Knight, and P. S. Russell, "Endlessly single-mode photonic crystal fiber." Optics Letters **22**, 961–3 (1997).

[60] J. Zhou, K. Tajima, K. Nakajima, K. Kurokawa, C. Fukai, T. Matsui, and I. Sankawa, "Progress on low loss photonic crystal fibers," Optical Fiber Technology **11**, 101–110 (2005).

[61] W. J. Miniscalco, "Optical and Electronic Properties of Rare Earth Ions in Glasses," in "Rare-Earth-Doped Fiber Lasers and Amplifiers," (Taylor and Francis, 2001).

[62] S. Jackson, "Towards high-power mid-infrared emission from a fibre laser," Nature Photonics **6**, 423–431 (2012).

[63] R. Paschotta, "http://www.rp-photonics.com/," Webpage **October 11** (2013).

[64] J. Kirchhof, S. Unger, A. Schwuchow, S. Grimm, and V. Reichel, "Materials for high-power fiber lasers," Journal of Non-Crystalline Solids **352**, 2399–2403 (2006).

[65] R. Paschotta, J. Nilsson, A. Tropper, and D. Hanna, "Ytterbium-doped fiber amplifiers," IEEE Journal of Quantum Electronics **33**, 1049–1056 (1997).

[66] NLight-Liekki, "http://www.nlight.net/products/active-fiber/," Webpage **October 23** (2013).

[67] Nufern, "http://www.nufern.com/pam/opticalfibers/," Webpage **October 23** (2013).

[68] R. Paschotta, "Ultrafast Laser Systems: Fiber or Bulk Solutions? A comparison from a developer's perspective," laser-journal.de pp. 51–55 (2013).

[69] K. Mattsson, "The three-electron bond SiO2Yb absorption center of pre-darkened ytterbium-doped silica," Optics express **21**, 12849–12864 (2013).

[70] J. D. Jackson, *Classical electrodynamics* (Wiley, 1999).

[71] K. R. Hansen, T. T. Alkeskjold, J. Broeng, and J. Lægsgaard, "Theoretical analysis of mode instability in high-power fiber amplifiers." Optics Express **21**, 1944–71 (2013).

[72] D. Gloge, "Weakly guiding fibers," Applied Optics **10**, 2252–8 (1971).

[73] S. Jackson and T. King, "Theoretical modeling of Tm-doped silica fiber lasers," Journal of Lightwave Technology **17**, 948–956 (1999).

[74] J. Dudley, G. Genty, F. Dias, B. Kibler, and N. Akhmediev, "The dynamics of a developing CW supercontinuum: analytical predictions and experiments," OSA OFC pp. 1–3 (2010).

[75] M. Pedersen, K. Rottwitt, and K. Jespersen, "Non-Linear Fibres for Widely Tunable Femtosecond Fibre Lasers," Ph.D. thesis, DTU (2013).

[76] M. Pedersen, P. Kristensen, L. Gruner-Nielsen, and K. Rottwitt, "Impact of the Scalar Approximation on the Prediction of the Group Velocity Dispersion," Journal of Lightwave Technology **29**, 3129–3134 (2011).

[77] P. Moselund, "Long-pulse supercontinuum light sources," Ph.D. thesis, DTU (2009).

[78] C. Larsen, S. T. Sørensen, D. Noordegraaf, K. Hansen, K. Mattsson, and O. Bang, "Zero-dispersion wavelength independent quasi-CW pumped supercontinuum generation," Optics Communications **290**, 170–174 (2013).

[79] Y. Shen, "Optical second harmonic generation at interfaces," Annual Review of Physical Chemistry **40**, 327–50 (1989).

[80] N. Bloembergen and P. Pershan, "Light waves at the boundary of nonlinear media," Physical Review **128** (1962).

[81] N. Bloembergen, "Surface nonlinear optics: a historical overview," Applied Physics B: Lasers and Optics **293**, 289–293 (1999).

[82] R. Khakimov, I. Shavrin, S. Novotny, M. Kaivola, and H. Ludvigsen, "Numerical solver for supercontinuum generation in multimode optical fibers," Optics Express **21**, 834–839 (2013).

[83] K. J. Blow and D. L. Wood, "Theopetical Description of Transient Stimulated Raman Scattering in Optical Fibers," IEEE Journal of Quantum Electronics **25**, 2665 (1989).

[84] J. Laegsgaard, "Mode profile dispersion in the generalised nonlinear Schrödinger equation," Optics Express **15**, 337–342 (2007).

[85] J. Hult, "A Fourth-Order Runge-Kutta in the Interaction Picture Method for Simulating Supercontinuum Generation in Optical Fibers," Journal of Lightwave Technology **25**, 3770–3775 (2007).

[86] C. Agger, C. Petersen, S. Dupont, H. Steffensen, J. K. Lyngsø, C. L. Thomsen, J. Thøgersen, S. R. Keiding, and O. Bang, "Supercontinuum generation in ZBLAN fibers-detailed comparison between measurement and simulation," Journal of the Optical Society of America B **29**, 635 (2012).

[87] M. H. Frosz, T. Sørensen, and O. Bang, "Nanoengineering of photonic crystal fibers for supercontinuum spectral shaping," Journal of the Optical Society of America B **23**, 1692 (2006).

[88] J. Lægsgaard, P. J. Roberts, and M. Bache, "Tailoring the dispersion properties of photonic crystal fibers," Optical and Quantum Electronics **39**, 995–1008 (2007).

[89] T. Kato, Y. Suetsugu, and M. Nishimura, "Estimation of nonlinear refractive index in various silica-based glasses for optical fibers." Optics Letters **20**, 2279 (1995).

[90] C. Fukai, K. Nakajima, J. Zhou, K. Tajima, K. Kurokawa, and I. Sankawa, "Effective Raman gain characteristics in germanium- and fluorine-doped optical fibers." Optics Letters **29**, 545–7 (2004).

[91] O. Sinkin and R. Holzlöhner, "Optimization of the split-step Fourier method in modeling optical-fiber communications systems," Journal of Lightwave Technology **21**, 61–68 (2003).

[92] A. Heidt, "Efficient adaptive step size method for the simulation of supercontinuum generation in optical fibers," Journal of Lightwave Technology **27**, 3984–3991 (2009).

[93] R. Collins, D. Nelson, and A. Schawlow, "Coherence, narrowing, directionality, and relaxation oscillations in the light emission from ruby," Physical Review Letters **5** (1960).

[94] Gurs, "Relaxationschwingungen in der emission optischer rubinmaser unter versciedenen arbeitsbedingungen," Zeitschrift fur Naturforschung (1963).

[95] R. Dunsmuir, "Theory of Relaxation Oscillations in Optical Masers," INTERNATIONAL JOURNAL OF ELECTRONICS (1961).

[96] L. Casperson and A. Yariv, "The time behavior and spectra of relaxation oscillations in a high-gain laser," Quantum Electronics, IEEE Journal of pp. 69–73 (1972).

[97] W. G. Wagner and B. a. Lengyel, "Evolution of the Giant Pulse in a Laser," Journal of Applied Physics **34**, 2040 (1963).

[98] D. A. Kleinman, "The maser rate equations and spiking," Bell System Technical Journal (1964).

[99] W. Koechner, *Solid-state laser engineering* (Springer-Verlag, 2006).

[100] D. Carlson, "Dynamics of a Repetitively Pump-Pulsed Nd:YAG Laser," Journal of Applied Physics **39**, 4369–4374 (1968).

[101] W. Lauterborn and R. Steinhoff, "Bifurcation structure of a laser with pump modulation," JOSA B **5**, 1097–1104 (1988).

[102] K. S. Wu, D. Ottaway, J. Munch, D. G. Lancaster, S. Bennetts, and S. D. Jackson, "Gain-switched holmium-doped fibre laser." Optics Express **17**, 20872–7 (2009).

[103] M. L. Flohic, P.-l. Francois, M. J.-y. Allain, F. Sanchez, and G. M. Stcphan, "Dynamics of the Transient Buildup of Emission in Nd3+-Doped Fiber Lasers," IEEE Journal of Quantum Electronics **27** (1991).

[104] S. Jackson and T. King, "Efficient gain-switched operation of a Tm-doped silica fiber laser," IEEE Journal of Quantum Electronics **34**, 779–789 (1998).

[105] B. Dickinson, S. Jackson, and T. King, "10 mJ total output from a gain-switched Tm-doped fibre laser," Optics communications pp. 199–203 (2000).

[106] B. C. Dickinson, P. S. Golding, M. Pollnau, T. A. King, and S. D. Jackson, "Investigation of a 791-nm pulsed-pumped 2.7-um Er-doped ZBLAN fibre laser," Optics Communications **191**, 315–321 (2001).

[107] S. Jackson, "Direct evidence for laser reabsorption as initial cause for self-pulsing in three-level fibre lasers," Electronics Letters **38**, 1640–1642 (2002).

[108] J. Yang, Y. Tang, and J. Xu, "Development and applications of gain-switched fiber lasers [Invited]," Photonics Research **1**, 52 (2013).

[109] M. Jiang and P. Tayebati, "Stable 10 ns, kilowatt peak-power pulse generation from a gain-switched Tm-doped fiber laser." Optics Letters **32**, 1797–9 (2007).

[110] M. Jiang and D. Mahgerefteh, "Gain-switched fiber laser system," (2010).

[111] J. Ding, B. Sampson, A. Carter, C. Wang, and K. Tankala, "A monolithic thulium doped single mode fiber laser with 1.5ns pulsewidth and 8kw peak power," SPIE **7914** (2011).

[112] N. Simakov, A. Hemming, S. Bennetts, and J. Haub, "Efficient, polarised, gain-switched operation of a Tm-doped fibre laser." Optics Express **19**, 14949–54 (2011).

[113] H. Nakagami, S. Araki, and H. Sakata, "Gain-switching pulse generation of Tm-doped fiber ring laser pumped with 1.6-um laser diodes," Laser Physics Letters **8**, 301–304 (2011).

[114] X. B. Zhang, X. Zhu, L. Chen, F. G. Jiang, X. B. Yang, J. G. Peng, and J. Y. Li, "Enhanced violet Cherenkov radiation generation in GeO2-doped photonic crystal fiber," Applied Physics B **111**, 273–277 (2013).

[115] M. Tao, J. Zhao, Y. Yan, Z. Wang, P. Yang, G. Feng, and X. Ye, "Experimental investigation of gain-switched Tm-Ho Co-doped single clad fiber lasers," Laser Physics **23**, 105101 (2013).

[116] C. Gu, L. Xu, W. H. Chung, L. Shao, H. Y. Tam, and H. Ming, "Gain switching of an Yb-doped DFB fiber laser," SPIE **6838**, 683808–683808–3 (2007).

[117] Y. Sintov, M. Katz, P. Blau, Y. Glick, E. Lebiush, and Y. Nafcha, "A frequency doubled gain switched Yb3+ doped fiber laser," SPIE **7195**, 719529 (2009).

[118] M. Giesberts, J. Geiger, M. Traub, and H.-D. Hoffmann, "Novel design of a gain-switched diode-pumped fiber laser," SPIE **7195**, 71952P (2009).

[119] R. Petkovšek, V. Agrež, and F. Bammer, "Gain-switching of a fiber laser: experiment and a simple theoretical model," SPIE **7721**, 77210L–1 (2010).

[120] V. Agrež and R. Petkovšek, "Gain-switched Yb-doped fiber laser for micro-processing," Applied Optics **52**, 3066–3072 (2013).

[121] R. Petkovšek, V. Agrež, F. Bammer, P. Jakopič, and B. Lenardič, "Experimental and theoretical study of gain switched Yb-doped fiber laser," SPIE **8601**, 860128–6 (2013).

[122] R. Petkovšek and V. Agrež, "Gain Switch Laser based on Microstructured Yb-Doped Active Fiber," Advanced Solid State Lasers pp. 50–52 (2013).

[123] J. Yang, H. Li, Y. Tang, and J. Xu, "Temporal Characteristics of In-Band-Pumped Gain-Switched Tm-doped Fiber Lasers," JOSA B (2013).

[124] J. L. Yang, Y. L. Tang, and J. Q. Xu, "Hybrid-pumped, gain-switching operation of a Tm-doped fiber laser with linear-polarized output," Laser Physics Letters **10**, 055104 (2013).

[125] Y. Tang, L. Xu, Y. Yang, and J. Xu, "High-power gain-switched Tm 3+-doped fiber laser," Optics Express **18**, 22964–22972 (2010).

[126] Y. Tang and J. Xu, "Hybrid-Pumped Gain-Switched Narrow-Band Thulium Fiber Laser," Applied Physics Express **5**, 072702 (2012).

[127] Y. Tang, F. Li, and J. Xu, "Narrow-pulse-width gain-switched thulium fiber laser," Laser Physics Letters **10**, 035101 (2013).

[128] H. Zhang, H. Xiao, P. Zhou, X. Wang, and X. Xu, "Hybrid-pumped, gain-switched 1120 nm Yb-doped fiber laser," Applied Optics (2013).

[129] V. V. Dvoyrin, "Pulsed Fiber Laser with Cross-Modulation of Laser Cavities," Conference on Lasers and Electro-Optics 2012 p. CTu3M.5 (2012).

[130] A. Jin, J. Hou, B. Zhang, H. Chen, and Z. Jiang, "Theoretical models for beam quality evaluation of fiber supercontinuum sources," Optics Express **21** (2013).

[131] A. Hemming, S. Bennetts, N. Simakov, J. Haub, and A. Carter, "Development of resonantly cladding-pumped holmium-doped fibre lasers," SPIE **8237** (2012).

[132] G. Qin, T. Suzuki, and Y. Ohishi, "Stable gain-switched 845 nm pulse generation by a weak 1550 nm seed laser." Optics Letters **33**, 249–51 (2008).

[133] J. Li, T. Hu, and S. D. Jackson, "Q-switched induced gain switching of a two-transition cascade laser." Optics Express **20**, 13123–8 (2012).

[134] J. Swiderski, M. Maciejewska, J. Kwiatkowski, and M. Mamajek, "An all-fiber, resonantly pumped, gain-switched, 2 μm Tm-doped silica fiber laser," Laser Physics Letters **10**, 015107 (2013).

[135] J. Swiderski and M. Michalska, "Generation of self-mode-locked, fast gain-switched thulium-doped fiber laser," Optics Letters **38**, 1624–1626 (2013).

[136] P. Boers, "Dynamic behaviour of semiconductor lasers," Electronics Letters pp. 206–208 (1975).

[137] K. Y. Lau, "Gain switching of semiconductor injection lasers," Applied Physics Letters **52**, 257 (1988).

[138] P. Dupriez, a. Piper, A. Malinowski, J. Sahu, M. Ibsen, B. Thomsen, Y. Jeong, L. Hickey, M. Zervas, J. Nilsson, and D. Richardson, "High average power, high repetition rate, picosecond pulsed fiber master oscillator power amplifier source seeded by a gain-switched laser diode at 1060 nm," IEEE Photonics Technology Letters **18**, 1013–1015 (2006).

[139] B. Barnes and P. Morkel, "Q-switching in fibre lasers," SPIE **1171** (1990).

[140] O. Schmidt, J. Rothhardt, F. Röser, S. Linke, T. Schreiber, K. Rademaker, J. Limpert, S. Ermeneux, P. Yvernault, F. Salin, and A. Tünnermann, "Millijoule pulse energy Q-switched short-length fiber laser." Optics Letters **32**, 1551–3 (2007).

[141] M. Laurila, J. Saby, T. T. Alkeskjold, L. Scolari, B. Cocquelin, F. Salin, J. Broeng, and J. Lægsgaard, "Q-switching and efficient harmonic generation from a single-mode LMA photonic bandgap rod fiber laser." Optics Express **19**, 10824–33 (2011).

[142] C. Jauregui, J. Limpert, and A. Tünnermann, "High-power fibre lasers," Nature Photonics **7**, 861–867 (2013).

[143] A. Avdokhin, S. Popov, and J. Taylor, "Continuous-wave, high-power, Raman continuum generation in holey fibers," Optics Letters **28**, 1353–1355 (2003).

[144] C. C. Renaud, H. L. Offerhaus, J. Nilsson, W. A. Clarkson, P. W. Turner, D. J. Richardson, and A. B. Grudinin, "Characteristics of Q-Switched Cladding-Pumped Ytterbium-Doped Fiber Lasers with Different High-Energy Fiber Designs," IEEE Journal of Quantum Electronics **37**, 199–206 (2001).

[145] J. Kerttula, V. Filippov, Y. Chamorovskii, K. Golant, and O. G. Okhotnikov, "250uJ Broadband Supercontinuum Generated Using a Q-Switched Tapered Fiber Laser," IEEE Photonics Technology Letters **23**, 380–382 (2011).

[146] M. J. F. Digonnet, *Rare-Earth-Doped Fiber Lasers and Amplifiers* (CRC press, 2001).

[147] M. E. Fermann, M. Andrejco, Y. Silberberg, and M. Stock, "Passive mode locking by using nonlinear polarization evolution in a polarization-maintaining erbium-doped fiber." Optics Letters **18**, 894 (1993).

[148] T. Andersen, P. Pérez-Millán, S. Keiding, S. Agger, R. Duchowicz, and M. Andrés, "All-fiber actively Q-switched Yb-doped laser," Optics Communications **260**, 251–256 (2006).

[149] M. Andrés, J. Cruz, a. Díez, P. Pérez-Millán, and M. Delgado-Pinar, "Actively Q-switched all-fiber lasers," Laser Physics Letters **5**, 93–99 (2008).

[150] A. Kurkov, "Q-switched all-fiber lasers with saturable absorbers," Laser Physics Letters **8**, 335–342 (2011).

[151] D. B. S. Soh, S. E. Bisson, B. D. Patterson, and S. W. Moore, "High-power all-fiber passively Q-switched laser using a doped fiber as a saturable absorber: numerical simulations." Optics Letters **36**, 2536–8 (2011).

[152] S. V. Chernikov, Y. Zhu, J. R. Taylor, and V. P. Gapontsev, "Supercontinuum self-Q-switched ytterbium fiber laser." Optics Letters **22**, 298–300 (1997).

[153] Y. Wang and C.-Q. Xu, "Actively Q-switched fiber lasers: Switching dynamics and nonlinear processes," Progress in Quantum Electronics **31**, 131–216 (2007).

[154] P. Milonni and J. Eberly, *Lasers* (John Wiley and Sons, 1988).

[155] C. L. Tang, "On Maser Rate Equations and Transient Oscillations," Journal of Applied Physics **34**, 2935 (1963).

[156] M. Dinand and C. Schutte, "Theoretical modeling of relaxation oscillations in Er-doped waveguide lasers," Journal of Lightwave Technology **13**, 14–23 (1995).

[157] J. Marcerou, H. Fevrier, and J. Ramos, "General theoretical approach describing the complete behavior of the erbium-doped fiber amplifier," SPIE (1990).

[158] C. Giles and E. Desurvire, "Modeling erbium-doped fiber amplifiers," Journal of Lightwave Technology **9** (1991).

[159] N. A. Brilliant, R. J. Beach, A. D. Drobshoff, and S. A. Payne, "Narrow-line ytterbium fiber master-oscillator power amplifier," Journal of the Optical Society of America B **19**, 981 (2002).

[160] J. Yang, Y. Tang, R. Zhang, and J. Xu, "Modeling and Characteristics of Gain-Switched Diode-Pumped Er-Yb Codoped Fiber Lasers," IEEE Journal of Quantum Electronics **48**, 1560–1567 (2012).

[161] J. Swiderski, A. Zajac, P. Konieczny, and M. Skorczakowski, "Numerical model of a Q-switched double-clad fiber laser." Optics Express **12**, 3554–9 (2004).

[162] Y. Wang and C.-Q. Xu, "Modeling and optimization of Q-switched double-clad fiber lasers." Applied Optics **45**, 2058–71 (2006).

[163] P. Wysocki, "Accurate modeling of next-generation rare-earth-doped fiber devices," OSA **16**, 46–71 (1997).

[164] G. C. Valley, "Modeling Cladding-Pumped Er/Yb Fiber Amplifiers," Optical Fiber Technology **7**, 21–44 (2001).

[165] Y. Wang, C. Xiong, J. Hou, J. Cao, Y. Li, R. Song, and Q. Lu, "Continuous wave, dual-wavelength-pumped supercontinuum generation in an all-fiber device." Applied Optics **50**, 2752–8 (2011).

[166] R.-L. Zhou, Y.-L. Ju, J. Zhao, C. Yang, and Y.-Z. Wang, "A theoretical and experimental investigation of an in-band pumped gain-switched thulium-doped fiber laser," Chinese Physics B **22**, 064208 (2013).

[167] A. Siegmann, *Lasers* (University Science Books, 1986).

[168] G. Sorbello, S. Taccheo, and P. Laporta, "Numerical modelling and experimental investigation of double-cladding erbium-ytterbium-doped fibre amplirers," Optical and Quantum Electronics **33**, 599–619 (2001).

[169] E. Desurvire and J. Simpson, "Amplification of spontaneous emission in erbium-doped single-mode fibers," Journal of Lightwave Technology **7**, 835–845 (1989).

[170] R. Oron and A. a. Hardy, "Rayleigh backscattering and amplified spontaneous emission in high-power ytterbium-doped fiber amplifiers," Journal of the Optical Society of America B **16**, 695 (1999).

[171] C. Henry, "Theory of spontaneous emission noise in open resonators and its application to lasers and optical amplifiers," Journal of Lightwave Technology **4**, 288–297 (1986).

[172] A. Hartog and M. Gold, "On the theory of backscattering in single-mode optical fibers," Journal of Lightwave Technology **2**, 76–82 (1984).

[173] C. Larsen, D. Noordegraaf, P. M. W. Skovgaard, K. P. Hansen, K. E. Mattsson, and O. Bang, "Gain-switched CW fiber laser for

improved supercontinuum generation in a PCF." Optics Express **19**, 14883–91 (2011).

[174] C. Larsen, M. Giesberts, S. Nyga, O. Fitzau, B. Jungbluth, H. D. Hoffmann, and O. Bang, "Gain-switched all-fiber laser with narrow bandwidth," Optics Express **21**, 170–174 (2013).

[175] M.-A. Lapointe and M. Piche, "Linewidth of high-power fiber lasers," SPIE **7386**, 73860S (2009).

[176] S. I. Kablukov, E. a. Zlobina, E. V. Podivilov, and S. a. Babin, "Output spectrum of Yb-doped fiber lasers." Optics Letters **37**, 2508–10 (2012).

[177] C. Larsen, D. Noordegraaf, K. P. Hansen, K. E. Mattsson, and O. Bang, "Photonic crystal fibers for supercontinuum generation pumped by a gain-switched CW fiber laser," SPIE (2012).

[178] J. C. Travers, "High average power supercontinuum sources," Pramana **75**, 769–785 (2010).

[179] R. R. Alfano, *The Supercontinuum Laser Source* (Springer-Verlag, New York, 2006).

[180] S. T. Sørensen, A. Judge, C. L. Thomsen, and O. Bang, "Optimum fiber tapers for increasing the power in the blue edge of a supercontinuum-group-acceleration matching." Optics Letters **36**, 816–8 (2011).

[181] J. M. Stone and J. C. Knight, "Visibly "white" light generation in uniform photonic crystal fiber using a microchip laser." Optics Express **16**, 2670–5 (2008).

[182] A. V. Gorbach and D. V. Skryabin, "Light trapping in gravity-like potentials and expansion of supercontinuum spectra in photonic-crystal fibres," Nature Photonics **1**, 653–657 (2007).

[183] P. Beaud and W. Hodel, "Ultrashort pulse propagation, pulse breakup, and fundamental soliton formation in a single-mode optical fiber," IEEE Journal of Quantum Electronics **23**, 1938–1946 (1987).

[184] J. C. Travers, "Blue solitary waves from infrared continuous wave pumping of optical fibers." Optics Express **17**, 1502–7 (2009).

[185] E. Kelleher, "Pump wave coherence, modulation instability and their effect on continuous-wave supercontinua," Optical Fiber Technology **18**, 268–282 (2012).

[186] E. J. R. Kelleher, J. C. Travers, S. V. Popov, and J. R. Taylor, "Role of pump coherence in the evolution of continuous-wave supercontinuum generation initiated by modulation instability," Journal of the Optical Society of America B **29**, 502 (2012).

[187] B. H. Chapman, J. C. Travers, S. V. Popov, a. Mussot, and a. Kudlinski, "Long wavelength extension of CW-pumped supercontinuum through soliton-dispersive wave interactions." Optics Express **18**, 24729–34 (2010).

[188] M. H. Frosz, "Validation of input-noise model for simulations of supercontinuum generation and rogue waves." Optics Express **18**, 14778–87 (2010).

[189] P. Persephonis, S. V. Chernikov, and J. Taylor, "Cascaded CW fibre Raman laser source 1.6-1.9 um," Electronics Letters **32**, 1486–1487 (1996).

[190] J. C. Travers, S. V. Popov, J. R. Taylor, H. Sabert, and B. Mangan, "CW-Pumped, High Power, Extended Supercontinuum Generation in Low Water-Loss PCF," ASSP pp. 6–8 (2005).

[191] B. Cumberland and A. Rulkov, "High Power CW Pumped Supercontinuum Sources," OSA pp. 7–9 (2008).

[192] J. C. Travers, "Controlling nonlinear optics with dispersion in photonic crystal fibres," Ph.D. thesis, Imperial College London (2008).

[193] A. Kudlinski and A. Mussot, "Optimization of continuous-wave supercontinuum generation," Optical Fiber Technology **18**, 322–326 (2012).

[194] A. Kudlinski, G. Bouwmans, M. Douay, M. Taki, and A. Mussot, "Dispersion-Engineered Photonic Crystal Fibers for CW-Pumped Supercontinuum Sources," Journal of Lightwave Technology **27**, 1556–1564 (2009).

[195] D. Labat, G. Melin, a. Mussot, a. Fleureau, L. Galkovsky, S. Lempereur, and a. Kudlinski, "Phosphorus-Doped Photonic Crystal Fibers for High-Power (36 W) Visible CW Supercontinuum," IEEE Photonics Journal **3**, 815–820 (2011).

[196] B. Barviau, O. Vanvincq, and A. Mussot, "Enhanced soliton self-frequency shift and CW supercontinuum generation in GeO 2-doped core photonic crystal fibers," Journal of the Optical Society of America B **28**, 1152–1160 (2011).

[197] A. C. Judge, O. Bang, B. J. Eggleton, B. T. Kuhlmey, E. C. Mägi, R. Pant, and C. M. de Sterke, "Optimization of the soliton self-frequency shift in a tapered photonic crystal fiber," Journal of the Optical Society of America B **26**, 2064 (2009).

[198] A. C. Judge, O. Bang, and C. Martijn de Sterke, "Theory of dispersive wave frequency shift via trapping by a soliton in an axially nonuniform optical fiber," Journal of the Optical Society of America B **27**, 2195 (2010).

[199] E. J. R. Kelleher, M. Erkintalo, and J. C. Travers, "Fission of solitons in continuous-wave supercontinuum." Optics Letters **37**, 5217–9 (2012).

[200] B. Chapman and J. C. Travers, "Non-Solitonic Extension of Supercontinua," CLEO **1**, 15–16 (2011).

[201] A. G. Van Engen, S. a. Diddams, and T. S. Clement, "Dispersion measurements of water with white-light interferometry." Applied optics **37**, 5679–86 (1998).

[202] J. P. Gordon, "Theory of the soliton self-frequency shift." Optics Letters **11**, 662–4 (1986).

[203] A. A. Voronin and A. M. Zheltikov, "Soliton self-frequency shift decelerated by self-steepening." Optics Letters **33**, 1723–5 (2008).

[204] M. Islam, G. Sucha, and I. Bar-Joseph, "Broad bandwidths from frequency-shifting solitons in fibers," Optics Letters **14**, 370–372 (1989).

[205] F. Luan, D. V. Skryabin, a. V. Yulin, and J. C. Knight, "Energy exchange between colliding solitons in photonic crystal fibers." Optics Express **14**, 9844–53 (2006).

[206] D. R. Solli, C. Ropers, P. Koonath, and B. Jalali, "Optical rogue waves." Nature **450**, 1054–7 (2007).

[207] M. Erkintalo, G. Genty, and J. M. Dudley, "Giant dispersive wave generation through soliton collision." Optics Letters **35**, 658–60 (2010).

[208] A. Mussot, A. Kudlinski, M. Kolobov, E. Louvergneaux, M. Douay, and M. Taki, "Observation of extreme temporal events in CW-pumped supercontinuum." Optics Express **17**, 17010–5 (2009).

[209] S. T. Sørensen, C. Larsen, U. Møller, P. M. Moselund, C. L. Thomsen, and O. Bang, "Influence of pump power and modulation instability gain spectrum on seeded supercontinuum and rogue wave generation," Journal of the Optical Society of America B **29**, 2875 (2012).

[210] G. Genty, C. de Sterke, O. Bang, F. Dias, N. Akhmediev, and J. Dudley, "Collisions and turbulence in optical rogue wave formation," Physics Letters A **374**, 989–996 (2010).

[211] M. Frosz, P. Falk, and O. Bang, "The role of the second zero-dispersion wavelength in generation of supercontinua and bright-bright soliton-pairs across the zero-dispersion wavelength." Optics Express **13**, 6181–92 (2005).

[212] G. Genty, M. Lehtonen, H. Ludvigsen, J. Broeng, and M. Kaivola, "Spectral broadening of femtosecond pulses into continuum radiation in microstructured fibers." Optics Express **10**, 1083–98 (2002).

[213] T. Schreiber, J. Limpert, H. Zellmer, A. Tünnermann, and K. Hansen, "High average power supercontinuum generation in photonic crystal fibers," Optics Communications **228**, 71–78 (2003).

[214] W. Wadsworth, N. Joly, J. Knight, T. Birks, F. Biancalana, and P. Russell, "Supercontinuum and four-wave mixing with Q-switched pulses in endlessly single-mode photonic crystal fibres." Optics Express **12**, 299–309 (2004).

[215] C. Lin and W. French, "Wideband near IR continuum generated (0.7-2.1um) in low-loss optical fibres," Electronics Letters **14**, 822 (1978).

[216] A. K. Abeeluck and C. Headley, "Continuous-wave pumping in the anomalous- and normal-dispersion regimes of nonlinear fibers for supercontinuum generation." Optics Letters **30**, 61–3 (2005).

[217] L. Abrardi, "Experimental study on the role of chromatic dispersion in continuous-wave supercontinuum generation," Journal of biomedical optics **27**, 426–435 (2009).

[218] M. H. Frosz, O. Bang, and A. Bjarklev, "Soliton collision and Raman gain regimes in continuous-wave pumped supercontinuum generation." Optics Express **14**, 9391–407 (2006).

[219] J. D. Harvey, R. Leonhardt, S. Coen, G. K. L. Wong, J. C. Knight, W. J. Wadsworth, and P. S. J. Russell, "Scalar modulation instability in the normal dispersion regime by use of a photonic crystal fiber." Optics Letters **28**, 2225–7 (2003).

[220] P. K. Wai, C. R. Menyuk, Y. C. Lee, and H. H. Chen, "Nonlinear pulse propagation in the neighborhood of the zero-dispersion wavelength of monomode optical fibers." Optics Letters **11**, 464–6 (1986).

[221] M. Erkintalo, Y. Q. Xu, S. G. Murdoch, J. M. Dudley, and G. Genty, "Cascaded Phase Matching and Nonlinear Symmetry Breaking in Fiber Frequency Combs," Physical Review Letters **109**, 223904 (2012).

[222] J. C. Travers, S. V. Popov, and J. R. Taylor, "Extended blue supercontinuum generation in cascaded holey fibers." Optics Letters **30**, 3132–4 (2005).

[223] A. Kudlinski, A. George, and J. Knight, "Zero-dispersion wavelength decreasing photonic crystal fibers for ultraviolet-extended supercontinuum generation," Optics Express **14**, 5715–5722 (2006).

[224] N. A. Mortensen, "Effective area of photonic crystal fibers." Optics Express **10**, 341–8 (2002).

[225] V. Rossin, E. Zucker, M. Peters, M. Everett, and B. Acklin, "High-Power High-Efficiency 910-980nm Broad Area Laser Diodes," SPIE (2004).

[226] L. Bao, J. Wang, M. Devito, D. Xu, D. Wise, P. Leisher, M. Grimshaw, W. Dong, S. Zhang, K. Price, D. Li, C. Bai, S. Patterson, and R. Martinsen, "Reliability of High Performance 9xx-nm Single Emitter Diode Lasers," SPIE **7583** (2010).

[227] JDSU, "http://www.jdsu.com/ProductLiterature/stdiodepumplaser-ds-cl-ae.pdf," Webpage **October 10** (2013).

[228] D. Noordegraaf, "Fused combiners for photonic crystal fibers," Ph.D. thesis, DTU (2012).

[229] IPGPhotonics, "http://www.ipgphotonics.com/Collateral/Documents/English-US/HPBrochure.pdf," Webpage **October 11** (2013).

[230] O. Svelto, *Principles of lasers* (Springer, 2010).

[231] Okamoto, *Fundamentals of optics waveguides* (Academic Press, 2000).

[232] J. W. Fleming, "Dispersion in GeO2-SiO2 glasses," Applied Optics **23** (1984).

[233] J. W. Fleming and D. L. Wood, "Refractive index dispersion and related properties in fluorine doped silica." Applied Optics **22**, 3102 (1983).